DISSERTATION

A CMOS COMPATIBLE OPTICAL BIOSENSING SYSTEM BASED ON LOCAL EVANESCENT FIELD SHIFT MECHANISM

Submitted by

Rongjin Yan

Department of Electrical and Computer Engineering

In partial fulfillment of the requirements

For the Degree of Doctor of Philosophy

Colorado State University

Fort Collins, Colorado

Fall 2011

Doctoral Committee:

Advisor: Kevin L. Lear

David S. Dandy
V Chandrasekar
Branislav Notaros

ABSTRACT

A CMOS COMPATIBLE OPTICAL BIOSENSING SYSTEM BASED ON LOCAL EVANESCENT FIELD SHIFT MECHANISM

The need for label-free integrated optical biosensors has dramatically increased in recent years. Integrated optical biosensors have many advantages, including low-cost, and portability. They can be applied to many fields, including clinical diagnostics, food safety, environmental monitoring, and biosecurity applications. One of the most important applications is point-of-care diagnosis, which means the disease could be tested at or near the site of patient care rather than in a laboratory.

We are exploring the issues of design, modeling and measurement of a novel chip-scale local evanescent array coupled (LEAC) biosensor, which is an ideal platform for point-of-care diagnosis.

Until now, three generations of LEAC samples have been designed, fabricated and tested. The 1st generation of LEAC sensor without a buried detector array was characterized using a commercial near field scanning optical microscope (NSOM). The sample was polished and was end-fire light coupled using single mode fiber. The field shift mechanism in this proof-to-concept configuration without buried detector arrays has been validated with inorganic adlayers[1], photoresist[2] and different concentrations of CRP proteins[3]. Mode beating

phenomena was predicted by the beam propagation method (BPM) and was observed in the NSOM measurement.

A 2nd generation LEAC sensor with a buried detector array was fabricated using 0.35μm CMOS process at the Avogo Technologies Inc., Fort Collins, Colorado. Characterizations with both single layer patternings, including photoresist as well as BSA [4] and immunoassay complexes [5] were done with cooperative efforts from various research groups. The BPM method was used to study the LEAC sensor, and the simulation results demonstrated the sensitivity of the LEAC sensor is 16%/nm, which was proved to match well with the experimental data [6]. Different antigen/antibodies, including mouse IgG and Hspx (a tuberculosis reactive antigen), have been used to test the immunoassay ability of LEAC sensor [7].

Many useful data have been collected by using the 2nd generation LEAC chip. However, during the characterization of the Avago chips, some design problems were revealed, including incompatibility with microfluidic integration, restricted detection region, strong sidewall scattering and uncoupled light interference from the single mode fiber. To address these problems, the 3rd generation LEAC sensor chip with buried detector arrays was designed to allow real-time monitoring and compatibility with microfluidic channel integration. 3rd generation samples have been fabricated in the CSU cleanroom and the mesa detector structure has been replaced with the thin insulator detector structure to solve the problems encountered during the characterizations. PDMS microfluidic channels and a multichannel measurement system consisting of a probe card, a multiplexing/amplification circuit and a LabVIEW program have been implemented into the LEAC system.

In recent years, outbreaks of fast spreading viral diseases, such as bird flu and H1N1, have drawn a lot of concern of the point-of-care virus detection techniques. To test the virus detection ability of LEAC sensor, 40nm and 200nm polystyrene nanoparticles were immobilized onto the waveguide, and the increased scattered light was collected. Sensitivities of 1%/particle and 0.04%/particle were observed for 200nm and 40nm particles respectively.

References:

[1] G. Yuan, M. Stephens, D. Dandy, and K. Lear, "Direct imaging of transient interference in a single-mode waveguide using near-field scanning optical microscopy," *IEEE Photonics Technology Letters*, vol. 17, Nov. 2005, pp. 2382-2384.

[2] G. Yuan, M. Stephens, D.S. Dandy, and K.L. Lear, "Local Evanescent, Array Coupled (LEAC) Biosensor Response to Low Index Adlayers," *Conference on Lasers and Electro-Optics (CLEO)*, CThL, 2006.

[3] R. Yan, G. Yuan, M.D. Stephens, X. He, C.S. Henry, D.S. Dandy, and K.L. Lear, "Evanescent field response to immunoassay layer thickness on planar waveguides," *Applied Physics Letters*, vol. 93, 2008, pp. 101110-3.

[4] R. Yan, S.P. Mestas, G. Yuan, R. Safaisini, D.S. Dandy, and K.L. Lear, "Label-free silicon photonic biosensor system with integrated detector array," *Lab on a Chip*, vol. 9, 2009, pp. 2163-2168.

[5] R. Yan, L. Kingry, R. Slayden, and K. Lear, "Demonstration of the immunoassay using local evanescent array coupled biosensor," *SPIE Photonic West 2010*, 2010, 7559-14.

[6] R. Yan, S.P. Mestas, G. Yuan, R. Safaisini, and K.L. Lear, "Response of Local Evanescent Array-Coupled Biosensors to Organic Nanofilms," *Journal of Selected Topics in Quantum*

Electronics, vol. 15, 2009, pp. 1469-1477.

[7] R. Yan, N.S. Lynn, L.C. Kingry, Z. Yi, R.A. Slayden, D.S. Dandy and K.L. Lear, "Waveguide biosensor with integrated detector array for tuberculosis testing," Applied Physics Letters, vol. 98, 2010, pp. 013702.

ACKNOWLEDGEMENTS

I would like to acknowledge the help of a number of individuals who have contributed to this project by providing either valuable suggestions or technical assistance.

First, I would like to thank my advisor, Dr. Kevin Lear, for his guidance, understanding, patience, and most importantly, his friendship during my graduate studies at Colorado State University. His investigative and skeptical mind helped me through the whole research project.

I would like to thank my committee members, Dr. David Dandy, Dr. V Chandrasekar, and Dr. Branislav Notaros for their valuable comments on my dissertation, especially to Dr. David Dandy for his supports and advices on the LEAC biosensor project.

I would also like to thank my friends and colleagues at Colorado State University for their support.

Last but not the least; I would like to thank my wife, Minda Le and my parents, for their support through my five years of Ph.D study. Without their support and encouragement, this thesis would definitely not be possible.

Rongjin Yan

TABLE OF CONTENTS

Chapter 1

INTRODUCTION & MOTIVATION

1.1 Introduction

Optical biosensors have important applications in many areas [1][2][3][4]. Label-free immunoassay sensing of multiple pathogens or other proteins is very important in point-of-care clinical diagnostics, food safety, environmental monitoring, and biosecurity applications. Sensitivity, cost and miniaturization are the most important aspects in the future biosensor research.

1.2 Optical waveguide and light source

Compared with conventional optical instruments, which transport light in the form of beams or rays that are diffracted, expanded, and focused by lenses or prisms, optical waveguides have advantages in miniaturizing optical devices. Integrated optical waveguide based biosensor has been well studied in recent years to help to develop chip-scale biosensing platforms. [5][6][7][8]

The principle of an optical waveguide is that an optical material of higher refractive index is surrounded with low refractive index material which acts as cladding. Under certain condition, light coupled into the higher index material will be trapped in the high index channel and propagate through multiple internal total reflections. There are many optical waveguide

structures, such as slab, channel or ridge waveguides, as shown in Fig. 1. In recent studies, ridge waveguides are adopted in many integrated biosensor structures. In this study, waveguide core structure will be fabricated with silicon nitride with silicon dioxide as the cladding. Silicon nitride and silicon dioxide are traditional semiconductor material, which lowers the cost of our silicon-based biosensor fabricated using trailing-edge CMOS technology.

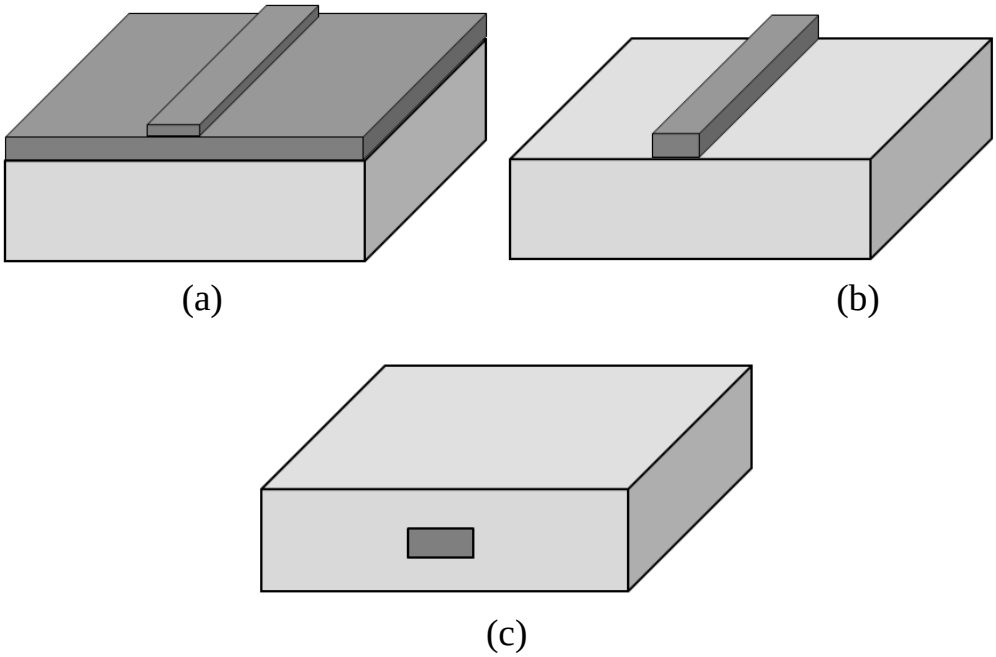

Fig. 1. (a) Ridge (b) rib and (c) channel waveguides.

The light source is one of the most important optical components for waveguides. Laser diodes and light emitting diodes (LED) are the most commonly used light sources for waveguides. A LED is basically just a specialized type of P-N junction diode, made from a thin chip of fairly heavily doped semiconductor material. LEDs have many advantages, such as low-

cost, high efficiency and small physical volume, which make it a good choice for integrated optical systems. Laser diode is a special form of LED. Just like a LED, they are P-N junction diode with a thin depletion layer where electrons and holes collide to create light photons, when the diode is forward biased. One difference is that in laser the active part is made quite narrow, to concentrate the carriers. An optical resonator cavity is needed to enable only light with selected frequency to pass the gain material multiple times, which makes the stimulated emission at selected frequency dominate. To achieve this, the ends of this narrow active region are often highly polished, or coated with distributed bragg reflectors (DBR) to act as mirrors, so it forms a resonant optical cavity. Compared with a LED, a laser diode has narrower spectrum (higher power at specified wavelength) and better light coherence. Limited by the detecting principles, most biosensing technologies, such as surface plasmon resonance (SPR), ring resonance or interferometer based biosensors, use a laser diode rather than a LED as their light source, although laser diode has higher cost and a relatively shorter lifetime. A biosensor system that could utilize the LEDs as the system light source will lower the system cost and simplify the system design.

1.3 Integrated waveguide biosensing

Integrated optical waveguide biosensing technology has become a worldwide attractive research area of high technical and fundamental importance. The major problem of most diagnostics technology is how to detect the target analytes efficiently and quickly. Limited by their detection principles and manufacturing cost, many existing detection technologies are still

suffering from long diagnostic time, high expense and lack of the portability. Many patients, especially in third-world countries, could not afford the diagnostic fees, which cause the infected persons to continue to spread the diseases, increasing their reach. In some special situations, say in battle fields, people don't have the time to travel to the hospital to take medicine treatment, and hence many infectious diseases could not be well controlled so many people will die of some easily curable diseases. Hence, point-of-care diagnosis will be very useful in these areas. The silicon-based biosensing technology described in this dissertation is compatible with the traditional CMOS fabrication technology, which makes it is possible to make disposable biosensor chips with high detection sensitivities. Millions of dollars each year in diagnostic examinations will be saved by applying such silicon-based integrated biosensors.

The integrated optical waveguide biosensor under investigation at Colorado State University would potentially detect low trace bioagents, including clinical pathogens (virus, bacteria), biowarfare agents, drugs, proteins (antibodies, enzymes) or toxicities, fermentation products and environmental agents (small molecules, proteins, ions). It is based on non-resonant biosensing technology, which lowers its requirement on light source and other off-chip equipment. It could eventually be operated with LED and integrated photodetector arrays. It is compatible with trailing-edge CMOS fabrication technology. The cost of per biosensor chip is estimated to be under $10, which makes it disposable. It will provide multi-analyte ability along each waveguide. It will help to drive the national public health and related economic properties, and hence improve people's life qualities in many aspects.

1.4 Research activities

In our research to develop a novel integrated waveguide biosensor, we exploited design, modeling and measurements research activities.

1.4.1 Design

The first task of this project is to design and optimize the structure and parameters of the biosensor, including the structure of the biosensor, geometric parameters of the waveguide, buried detector structures, and other components.

Many popular optical biosensing technologies are based on interaction between evanescent field change and the refractive index variation in the cladding. However, in these biosensors, the light power could only be detected after the light leaves the patterned region in the biosensor. We are the first research group to propose the "local field shift" detection principles, and design the local evanescent-field array coupled (LEAC) optical waveguide sensor that has the ability to detect the evanescent field shift due to specific binding of analytes to one of several localized regions of immobilized biological molecule probes. A metal-semiconductor-metal (MSM) photodetector array has been designed and implemented into the LEAC biosensor to detect the evanescent field shift due to the specific binding on the opposite side of the waveguide. Similar to the near field scanning microscope (NSOM), the detector array also senses the power change in the evanescent field tail granting the sensor the ability to simultaneously sense multiple analytes, such as virus, DNA and chemical agents. The penetration depth of the evanescent field is determined by guided mode and the refractive index of the waveguide core and cladding. A very thin waveguide core structure (~100nm) makes more coupled light power distribute to the

evanescent field, and a asymmetric waveguide structure (SiN_x waveguide core with air as the upper cladding and SiO_2 as the lower cladding) is adopted in the LEAC biosensor to force the evanescent field in the lower cladding to be much stronger than that in the upper cladding. This will benefit both the detection using the buried detector and the effective detection depth above the waveguide, whose dimension should be similar to the size of the bio-molecules interest to maximize both the sensitivity and the dynamic range.

1.4.2 Modeling

Computer simulation provides an easy way to predict the optical behavior, optimize the biosensor's performance and understand the physical principles behind the observed phenomenon in experiment. In our study, three numerical simulation methods are used, and they are 1-D mode calculation (matlab code), 2-D/3-D beam propagation method and finite domain time domain (FDTD) method (Rsoft software). Compared to the whole biosensor chip characterization flow, including fabrication, sample preparation, biomaterial patterning and measurement, computer simulation method is a more time-efficient and inexpensive way to test the optimized structure and predict the possible problem. For example, the 2-D BPM simulation showed the detected light power modulation due to the patterning will be much larger when using the buried detector array below the waveguide compared with NSOM measurement above the waveguide, and predicted the farther the detector is from the waveguide the larger the modulation is. Combined with noise calculation, optimized position of the buried detector was found, more details will be discussed in Chap. 3 [9]. What's more, numerical simulation method helps to understand the observed experiment results. The oscillation phenomena after the

patterned region on the waveguide was found for the first time when using NSOM to characterize the patterned LEAC biosensor sample, and the similar data were obtained in the following experiment measurements, including using the buried detector samples. The BPM simulation method was used to investigate this phenomenon, and the simulated result matched well with the experiment data [10]. Mode beating theory was used to explain the physical principle behind the experiment data and the calculation agreed with the measured result, and these indicate a successful LEAC biosensor design should have enough distance between each detection region.

1.4.3 Fabrication

3rd generation LEAC biosensors were fabricated using the in the CSU cleanroom. The LEAC chip was fabricated using multiple steps of photolithography, etching and thin film deposition. The first several batches of LEAC sensor were fabricated using a polysilicon wafer, and then silicon on insulator (SOI) wafers were used to replace the polysilicon wafer.

During the characterization of the Avago chip, a lot of problems were revealed, such as the waveguide width and detector length design, the non-optimized position of detector pads for microfluidic integration, and the photocurrent generated by the scattering light from the polishing edge.

Hence, a new LEAC sensor chip was designed to allow real-time monitoring and the compatibility with microfluidic channel integration. LASI was used to design the new mask. A waveguide bend was used to minimize the effect of the scattering light from the polishing edge during the fiber light coupling. Metal pads were put far from waveguides for three reasons: 1)

Enable the detection while the waveguide was covered by microfluidic channels. 2) Reduce the possibility to scratch the waveguide using micro probes. 3) Avoid the possible PDMS channel leaking problem due to the bad adhesion between PDMS and Al. Limited by the cost and equipment, chemical mechanical polishing (CMP) was not included in the new LEAC sensor fabrication flow, so different strategies were adopted to make sure the gaps between polysilicon detectors under waveguides won't cause too much light scattering. These strategies included 1) besides traditional discrete buried detectors, continuous buried detectors, which had no gaps between each detecting spot, were also included in the mask. 2) Tapered polysilicon buried detector was introduced to decrease the angle of the step in the gap. 3) Thinner detectors were tested to find the best trade-off point between light scattering loss and the sensitivity of the detector. Positions for grating coupling have been reserved on the new mask design.

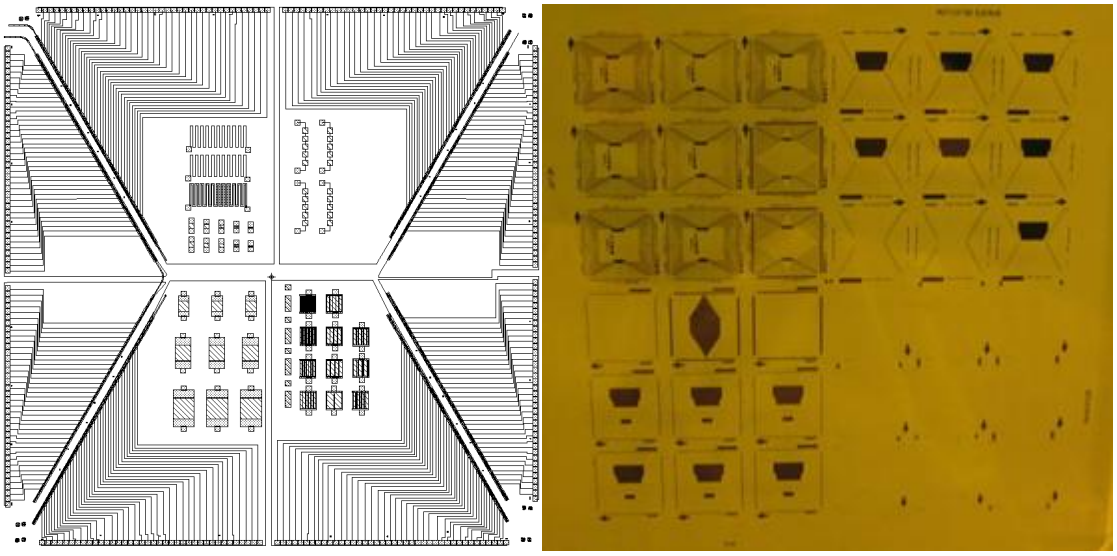

Fig. 2.3rd generation LEAC mask design (left) and mask layout (right) version 1.

The four different quadrants show the four main mask layers: Metal, Waveguide, Metal Via, and Buried Detectors. Within each quadrant are variations within each mask layer. These variations have different dimensions and features that will be tested on the LEAC chip. The fabrication of the 3rd generation of LEAC biosensor is finished in the CSU cleanroom with an optimized recipe which is compatible with traditional CMOS fabrication flow. More details could be found in chapter 4.

1.4.4 Measurements

Characterization of the biosensor is last but the most important step of the whole process. Near field scanning optical microscope technique is one of the most widely applied tools in optical waveguide researches. In our study, near field scanning optical microscope (NSOM) was used to examine the local field shift phenomenon and valid the LEAC biosensing concept before the buried photodetector array was integrated into the system. NSOM could provide both the topographic and optical information from the measured chip simultaneously, which is very useful in our measurement, since the local field shift mechanism describes the relationship between the thickness-induced effective refractive index change and the optical evanescent field distribution change. Compared with the traditional optical microscope, the high resolution of the NSOM provides a possible way to measure the evanescent field shift directly. For example, a 15nm thick, 180mm long C-reaction protein antibody antigen complex adlayer was patterned on a SiN_x waveguide surface, and the NSOM measurement accurately found the topographic change in the patterned region and ~50% optical modulation ratio was observed in the corresponding area [10].

NSOM is a very powerful tool to characterize the waveguide-based biosensor when there is no mobility or low cost requirement. However, one of the design goals of the LEAC biosensor is to fulfill the point-of-care requirement, which means bulky NSOM equipment is not the best choice. A group of buried photodetector array was integrated into the Avago LEAC biosensor chip to realize the chip-scale detecting system requirement. The photocurrent collected from the buried detector array is proportional to the evanescent light penetrating into it, and hence the current provides the information of the light distribution along the waveguide. One of the difficulties is to get the nano-ampere level current from the detector while not affecting the dark current when the light coupling fluctuations are easily caused by microprobe touch the sensor chip during measurement. Different measurement strategies were applied in the measurement to improve the signal. An AC measurement system using a lock-in amplifier was adopted in the measurement to replace the DC system to further decrease the noise level. To make the process of testing the LEAC chip much quicker we implemented a probe card to enable probing multiple photodetectors of the LEAC chip simultaneously. More details could be found in chapter 6.

1.5 Outline of the report

In chapter 2, the background information of the integrated optical waveguides will be summarized. Some necessary optical concepts related to this project are also introduced. Chapter 3 reviews the label-free optical biosensing technologies, including surface plasmon resonator biosensors, Mach-Zehnder Interferometer biosensor and ring resonator biosensor. Chapter 4 describes the biosensor design, sample fabrication/preparation and experiment setup for our study. The characterization results for different structures using NSOM will be presented in chapter 5. Chapter 6 presents the measurement results get from buried detector array. Chapter 7 reviews the work of the integration of the multichannel probe card and microfluidic channel with the LEAC sensor. Chapter 8 discusses the potential applications of the LEAC biosensor in virus detection. Chapter 9 summarizes conclusions and suggestions for future work.

References:

[1] J. Shah and E. Wilkins, "Electrochemical Biosensors for Detection of Biological Warfare Agents," *Electroanalysis,* vol. 15, 2003, pp. 157-167.

[2] C.A. Rowe-Taitt, J.W. Hazzard, K.E. Hoffman, J.J. Cras, J.P. Golden, and F.S. Ligler, "Simultaneous detection of six biohazardous agents using a planar waveguide array biosensor," *Biosensors and Bioelectronics,* vol. 15, Dec. 2000, pp. 579-589.

[3] C.A. Rowe, S.B. Scruggs, M.J. Feldstein, J.P. Golden, and F.S. Ligler, "An array immunosensor for simultaneous detection of clinical analytes," *Analytical Chemistry,* vol. 71, Jan. 1999, pp. 433-439.

[4] D.A. Chang-Yen and B.K. Gale, "Design, fabrication, and packaging of a practical multianalyte-capable optical biosensor," *Journal of Microlithography, Microfabrication, and Microsystems,* vol. 5, Apr. 2006, pp. 021105-8.

[5] M. Weisser, G. Tovar, S. Mittler-Neher, W. Knoll, F. Brosinger, H. Freimuth, M. Lacher, and W. Ehrfeld, "Specific bio-recognition reactions observed with an integrated Mach-Zehnder interferometer," *Biosensors and Bioelectronics,* vol. 14, Apr. 1999, pp. 405-411.

[6] M.R. Lee and P.M. Fauchet, "Two-dimensional silicon photonic crystal based biosensing platform for protein detection," *Optics Express,* vol. 15, Apr. 2007, pp. 4530-4535.

[7] R.D. Harris and J.S. Wilkinson, "Waveguide surface plasmon resonance sensors," *Sensors and Actuators B: Chemical,* vol. 29, Oct. 1995, pp. 261-267.

[8] R.W. Boyd and J.E. Heebner, "Sensitive Disk Resonator Photonic Biosensor," *Applied Optics,* vol. 40, Nov. 2001, pp. 5742-5747.

[9] R. Yan , S.P. Mestas, G. Yuan, R. Safaisini, and K.L. Lear, "Response of Local Evanescent Array-Coupled Biosensors to Organic Nanofilms," *Selected Topics in Quantum Electronics, IEEE Journal of,* vol. 15, 2009, pp. 1469-1477.

[10] R. Yan, G. Yuan, M.D. Stephens, X. He, C.S. Henry, D.S. Dandy, and K.L. Lear, "Evanescent field response to immunoassay layer thickness on planar waveguides," *Applied Physics Letters,* vol. 93, 2008, pp. 101110-3.

Chapter 2

OPTICAL WAVEGUIDE BASICS

2.1 Overview of waveguide studies

The optical waveguide has applications in many different areas and has been studied for years. In this section we will review some fundamentals of guided-wave devices and conventional waveguide characterization methodologies.

Waveguides are especially useful in the microwave and optical frequency ranges although they can be constructed to carry waves over a wide portion of the electromagnetic spectrum. Hollow metallic waveguide has long been used to manipulate radiation in the microwave portion of the spectrum. The guiding and processing of electromagnetic propagating beams is accomplished within low-loss metallic waveguides with cross sections comparable to the wavelength of the guided wave. These waveguides confine the radiation by repeated reflections from the walls. The power can propagate at a given frequency in a number of spatially distinct modes with different phase and group velocities.

The possibility of applying the microwave approach to laser beams was suggested by the demonstration of discrete propagating modes in optical fiber by Snitzer and Osterberg [1] in 1961 and by the demonstration by Yaric and Leite [2] in 1963 of planar dielectric waveguides in GaAs p-n junctions. Tien and his colleague's work on prism couplers [3] and the work on grating

couplers by Dakss et al [4] also contributed in this area. The effort in this field provided solutions to the problem of coupling Gaussian laser beams into and out of dielectric waveguides.

The characterization methods and tools for the optical research used in our experiments also greatly benefit from many researcher's previous work. An important waveguide characterization method that exploited a scatter light scanning technique on sputtered glass waveguides was adopted in several papers[5-8]. This measurement method is based on the loss property of the glass waveguide and provides a relatively easy way to analyze a waveguide for both industrial and academic research purpose.

The resolution in optical microscopy has been limited by diffraction to about half the wavelength of light. Going beyond this limit requires collecting information which is contained in the near-field. Near-field scanning optical microscopy (NSOM) was developed at a very fast pace from the middle of the 1990s (Fig. 2.1). It has been well adapted to characterization of integrated photonic waveguides world-wide since then [9-13]. Milestones were made in 1999, when a group of researchers at Boston University experimentally demonstrated the application of NSOM tip to measure the local evanescent field [14]. Other experimentalists at the University of Virginia for the first time observed modal interference in a channel waveguide by measuring the evanescent fields [15]. In recent years, the NSOM has become an effective measurement tool for analysis of optical waveguide biosensors, photonics crystals, and active waveguide devices. The improvement of the characterization methods grant the possibility to design, optimize and exploit various novel optical waveguide devices in recent years.

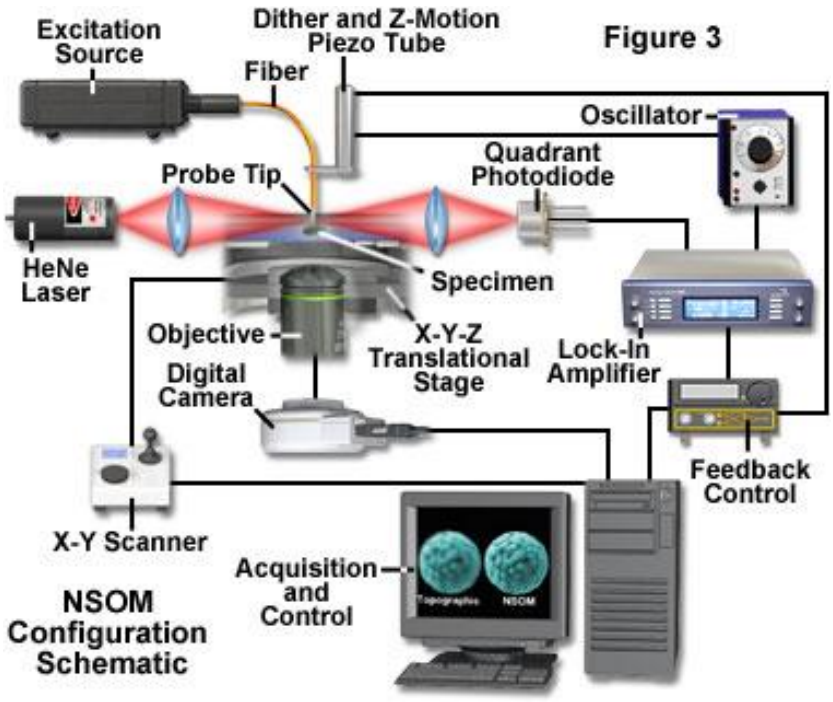

Fig. 2.1. NSOM system with optical feedback mechanism (from olympus).

In this chapter, some necessary basics of optics and waveguides are presented in Section 2.2. Where the methods to solve waveguide modes, losses, and evanescent fields are extensively discussed. In Section 2.3, we will review the background of optical waveguides and waveguide characterization efforts. The advantages and disadvantages of current characterization techniques will be discussed. Waveguide characterization methods are discussed, such as far-field scanning and near-field scanning optical microscopy (NSOM) methods.

2.2 Basic concept of optics and waveguides

2.2.1 Reflection, transmission and phase shift

Fresnel's equations describe the relationship between amplitudes for reflection/transmission and the incident field amplitude at a dielectric interface. From these equations, the power reflectivity / transmissivity as well as the phase shifts for reflected and transmitted wave can be calculated. This is important since it provide a simple way to solve and understand the waveguide problems.

In the following discussions, we assume that all optical properties in the two media are governed by real refractive indices, and thus ignoring absorption losses. The form of Fresnel's equations depends in detail on the type of the incident wave. The electric field perpendicular to the plane of incidence is called the S polarized component (transverse electric (TE) mode in a waveguide), and the electric field parallel to the plane of incidence is called the P polarized component (transverse magnetic (TM) mode in waveguide), as shown in Fig. 2.2. The Fresnel's equations for different components are listed in the equations below.

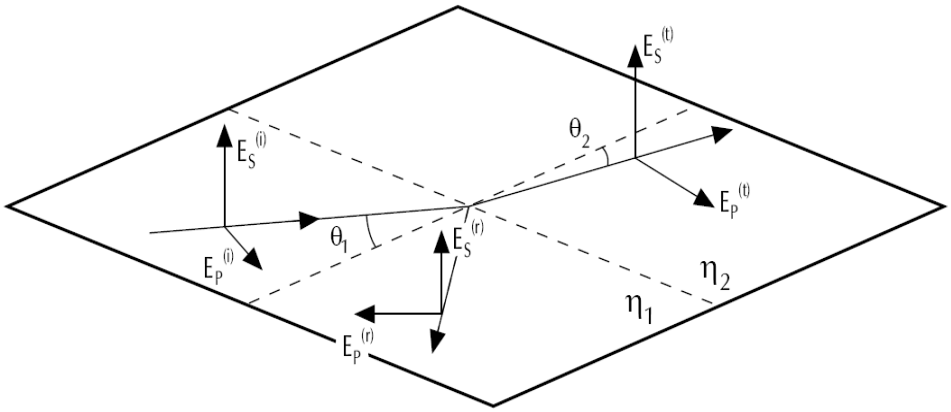

Fig. 2.2. The plane of incidence and the S/P polarized components.

$$t_p = \frac{E_p^{(t)}}{E_p^{(i)}} = \frac{2n_1 \cos\theta_1}{n_2 \cos\theta_1 + n_1 \cos\theta_2} \qquad t_s = \frac{E_s^{(t)}}{E_s^{(i)}} = \frac{2n_1 \cos\theta_1}{n_1 \cos\theta_1 + n_2 \cos\theta_2}$$

$$r_p = \frac{E_p^{(t)}}{E_p^{(i)}} = \frac{n_2 \cos\theta_1 - n_1 \cos\theta_2}{n_2 \cos\theta_1 + n_1 \cos\theta_2} = \frac{\tan(\theta_2 - \theta_1)}{\tan(\theta_2 + \theta_1)} \qquad r_s = \frac{E_s^{(t)}}{E_s^{(i)}} = \frac{n_1 \cos\theta_1 - n_2 \cos\theta_2}{n_1 \cos\theta_1 + n_2 \cos\theta_2} = \frac{\sin(\theta_2 - \theta_1)}{\sin(\theta_2 + \theta_1)} \quad (2.1)$$

where t_p is the transmittivity of P polarized field, t_s is the transmittivity of S polarized field, r_p is the reflectivity of P polarized field and r_s is the reflectivity of S polarized field.

In the Fresnel's equations, θ_2 is calculated from Snell's law:

$$n_1 \sin\theta_1 = n_2 \sin\theta_2 \quad (2.2)$$

The equations 2.1 are valid whenever θ_2 is a real angle. This is always true for external reflection, where $n_1 < n_2$. Plotted below are the examples for power reflectivities and phase shifts for the S and P components.

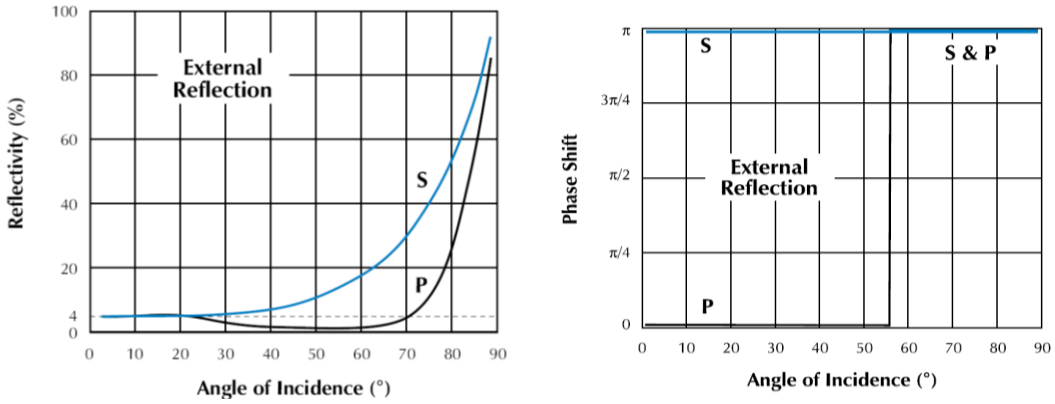

Fig. 2.3. Power reflectivity and phase shift at an n_1=1 to n_2=1.5 air-glass interface. Light is incident in air (external reflection). Transmitted phase shift is zero for both components. (www.cvilaser.com).

The term internal reflection is used when $n_1>n_2$, when the light is incident in the material of higher refractive index. According to Snell's law, when $n_1>n_2$ it is possible to choose an incidence angle θ_1 for which a real value of the angle of refraction θ_2 does not exist. This will occur for angles of incident $\theta_1>\theta_c$ where θ_c is the critical angle,

$$\theta_c = \sin^{-1}(n_2 / n_1) \qquad \text{for } n_2<n_1 \tag{2.3}$$

When the incidence angle is smaller than the critical angle, Fresnel's equations described above could be used to solve the problem. When the incident angle is larger than the critical angle, all the power of the incident light is reflected. This is called the total internal reflection (TIR), based on which the guided light in waveguide propagates. In this case, the amplitude of field reflectivities is 1. They are in the form of pure phase shift. The power reflectivity is 100%. The relative phase shifts for P and S are[16] :

$$\phi_p = -2\tan^{-1}\left(\frac{\sqrt{\sin^2\theta_1 - \sin^2\theta_c}}{\sin^2\theta_c \cos\theta_1}\right),\ \phi_s = -2\tan^{-1}\left(\frac{\sqrt{\sin^2\theta_1 - \sin^2\theta_c}}{\cos\theta_1}\right) \tag{2.4}$$

The plots for power reflectivity and absolute phase shifts are shown below.

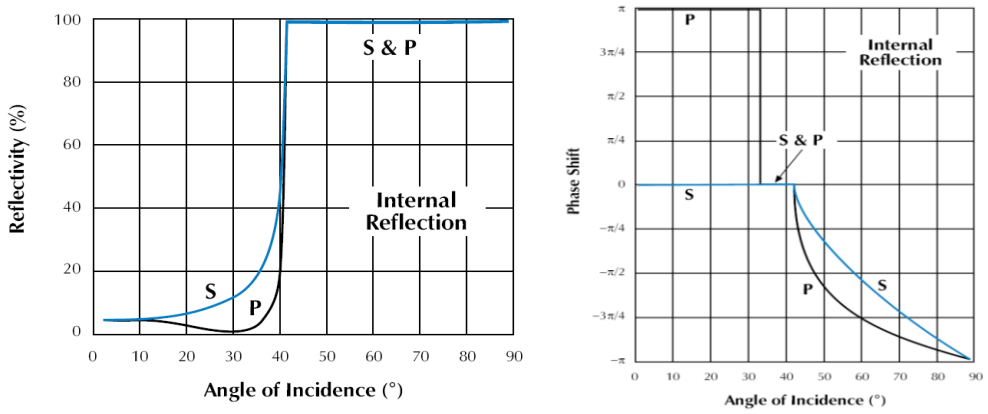

Fig. 2.4. Power reflectivity and phase shift at an n_1=1 to n_2=1.5 air-glass interface. Light is incident in air (external reflection). Transmitted phase shift is zero for both components. (www.cvilaser.com).

2.2.2 Optical waveguides

Optical waveguides have many different forms, such as the slab waveguide, ridge waveguide, and optical fibers. The simplest slab waveguide model will used in the following discussion to get a straightforward understanding of how the guided wave optical devices work.

To travel without loss in a slab waveguide shown as Fig. 2.5, the light must be trapped and guided inside the core of the slab, which has a higher refractive index n_1, by the rules of total internal reflection as discussed in section 2.2.1. Light is incident into the slab and propagates along the length of the waveguide which is taken to be parallel to the z-axis. Light is reflected at the slab boundaries with an angles θ to the z-axis and goes through multiple total internal reflections. The angle φ is required to be larger than the critical angle $\theta_c=\sin^{-1}(n_2/n_1)$ at the slab boundaries to ensure no loss in reflections. Otherwise, light would diminish along the length of the waveguide by losing a fraction of power at each reflection. However, in reality, even when the guided wave condition is met, light still diminishes at the slab boundaries due to scattering

loss. In some case, the side wall scattering could be a major issue for waveguide-based biosensing applications [17].

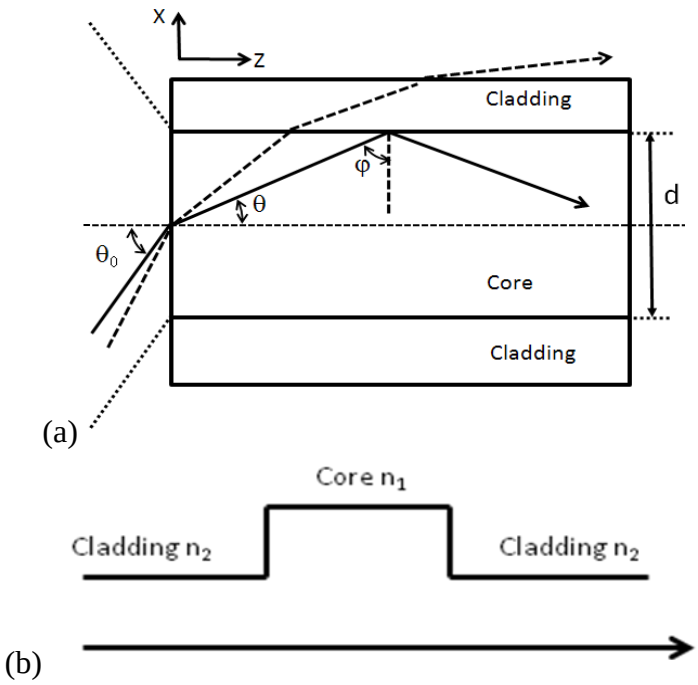

Fig. 2.5. a) Light incident in a slab waveguide with angles $\varphi > \theta_c$ are confined due to total internal reflection, b) corresponding refractive index profile of this slab waveguide.

Among all the different waveguide forms, the slab waveguide is one of the simplest types. However, in practice, waveguides are three-dimensional, so there is still some room left for us to further simplify the model of this waveguide. In the simplified 2-D slab model, only x and z-axis or the x-z plane is considered. This approximation is considered to be appropriate when studying waveguides with a large width-to-thickness ratio. However, when the width-to-thickness ratio is smaller than 10, the effect of width should be considered. In the LEAC biosensor waveguides, since we used a shallow slab waveguide (width-to-thickness ratio is larger than 20) to get a single mode waveguide, this approximation could be applied in our application.

First we will discuss the largest angle of light that can be coupled into a waveguide, which is defined by the numerical aperture (NA). From Snell's law, the minimum angle φ_{min} that supports total internal reflection for the light ray is given by,

$$\sin\varphi_{\min} = \frac{n_2}{n_1} \tag{2.5}$$

By applying the Snell's law to the air-waveguide core face boundary, the condition of equation 2.5 can be related to the maximum entrance angle $\vartheta_{0,max}$, which could be defined as numerical aperture (NA):

$$NA = n\sin\theta_{0,\max} = n_1\sin(\pi/2-\varphi_{\min}) = (n_1^{\,2}-n_2^{\,2})^{1/2} \tag{2.6}$$

Thus, those rays having entrance angle θ_0 less tan $\theta_{0,max}$ will be coupled into the waveguide and totally internally reflected at the core-cladding interface. Equation 2.6 also defines the V number:

$$V=\frac{\pi d}{\lambda}NA=\frac{\pi d}{\lambda}(n_1^2-n_2^2)^{1/2}\approx\frac{\pi d}{\lambda}n_1\sqrt{2\Delta} \quad \text{where} \quad n_2=n_1(1-\Delta) \tag{2.7}$$

where d is the thickness of the waveguide. V number helps to estimate the mode number supported in the waveguide. It will be useful factor to design a single mode waveguide (V<2.405 for optical fiber with step index), which is very important for LEAC biosensor. Not all light rays in the numerical aperture range will be supported as guided modes in the waveguide, instead, only limited angles fulfill the following conditions will propagate in the waveguide as guided "modes".

To begin, we assume that light rays bounce between the boundaries of the slab due to total international reflection. A self-consistency condition requires that the total phase shift in the x-axis must be zero or a multiple of 2π when light completes a round trip in this direction. Otherwise, the light at different wavefronts with different phase will destructively interference, which lead to diminishing of this mode. The total phase shift is contributed from the both propagation phase shift and phase shift due to reflection, as illustrated in Figure 2.6.

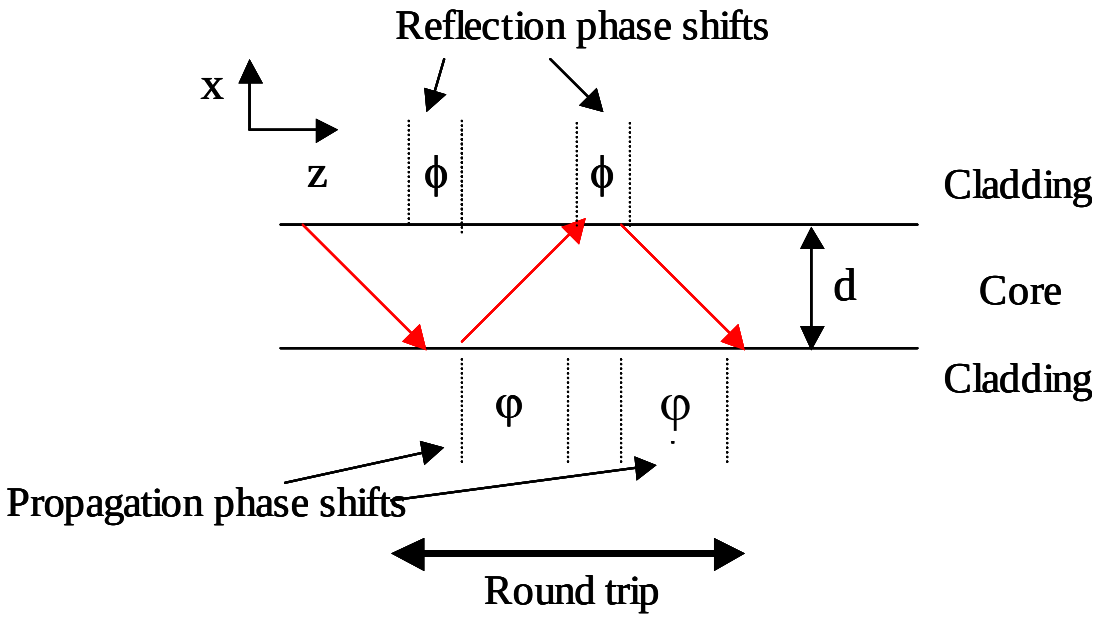

Fig. 2.6. Phase shifts in a slab waveguide.(Figure from Guanwei Yuan's dissertation).

In the following discussions, we will assume only a TE (transverse electric) mode in a slab waveguide. Light propagating along the waveguide is of a monochromatic wavelength λ. In waveguide core with refractive index n_1, the wavevector of the incident light is denoted as $k_0=2\pi n_1/\lambda$. This wavevector can be separated into x and z-components, $k_x = k_0 \sin\theta$ and $k_z = k_0 \cos\theta$, respectively. The phase delay between the twice-reflected wave to the original wave in

term of the thickness of the slab d is $2\varphi=2k_x d$, which is expressed in equation 2.8. The reflection phase shifts, 2ϕ, for the total internal reflections here are expressed in equation 2.9, as we discussed in Section 2.2.1. The sum of propagation phase shift and reflection phase shift must be equal to a multiple of 2π for a complete round trip to fulfill the self-consistency rule, as expressed in equation 2.10.

$$2\varphi = 2k_x d \tag{2.8}$$

$$\tan(\frac{\phi}{2}) = \frac{k_x}{k_{xcladding}} \tag{2.9}$$

$$2(\phi + \varphi) = 2m\pi, m = 0,1... \tag{2.10}$$

When substituting equation 2.8 and 2.10 into 2.9, we obtain the characteristic equation (2.11), where m is an integral number.

$$\tan(\frac{m\pi}{2} - \frac{k_x d}{2}) = \frac{k_x d}{k_{xcladding} d}, m = 0,1... \tag{2.11}$$

As we know, $k_x{}^2 + k_{xcladdng}^2 = V^2 = k_0 d \cdot NA$, we could plot this together with equation 2.11 in Fig. 2.7.

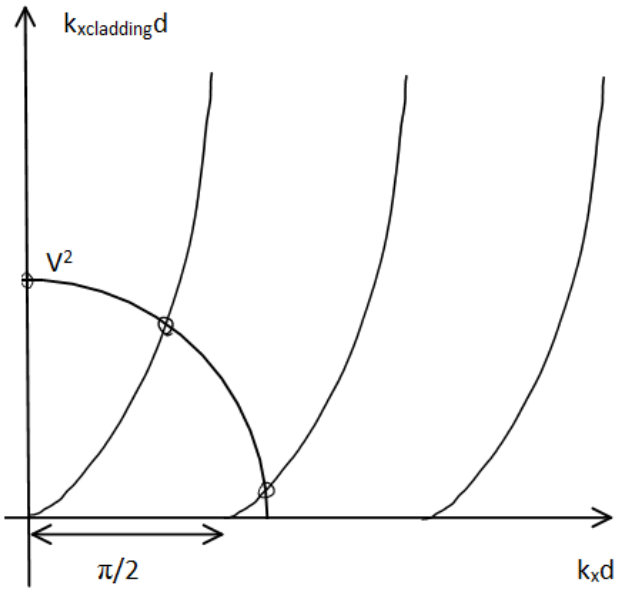

Fig. 2.7. TE mode in a 2-D slab waveguide.

In Fig. 2.7, every intersection point indicates a guided mode that can exist in the waveguide. Recall the propagation constants in the z-axis for each mode are defined as $\beta_{z,m} = n_1 \sin\theta_m k_0$, which are all the same for all three different waveguide regions: upper cladding, core and lower cladding. Notably, the propagation constants in the x-direction in the three regions are defined as $k_{x,m}=(k_0^2 n_1^2-\beta_{z,m}^2)^{1/2}$ in the core and $k_{xcladding,m}=(k_0^2 n_2^2-\beta_{z,m}^2)^{1/2}$ in the claddings, assuming a symmetric waveguide which has same upper and lower cladding refractive indices. We are able to write the E-field distributions in Eq. (2.12), where A_m is the E-field amplitude.

$$E_m(x)=\begin{cases} A_m \cos(k_{x,m}d/2)\exp(-k_{xcladding,m}(x-d/2)) & -d/2 \geq x \\ A_m \cos(k_{x,m}x) & -d/2 \leq x \leq d/2 \\ A_m \cos(k_{x,m}d/2)\exp(k_{xcladding,m}(x+d/2)) & x \geq d/2 \end{cases} \quad (2.12)$$

As shown in Fig. 2.8, the E-field in the cladding exponentially decays along x direction. This is called the evanescent field. On the one hand, the exponential decaying property makes the field only affected by an object with a size similar to the coupled light wavelength and hence the evanescent field detection becomes a popular area in optical biosensing studies. One the other hand, wavelength level penetration depth makes it could not be detected by the traditional microscope, so a NSOM will be a necessary tool to directly monitor the evanescent field on the waveguide surface.

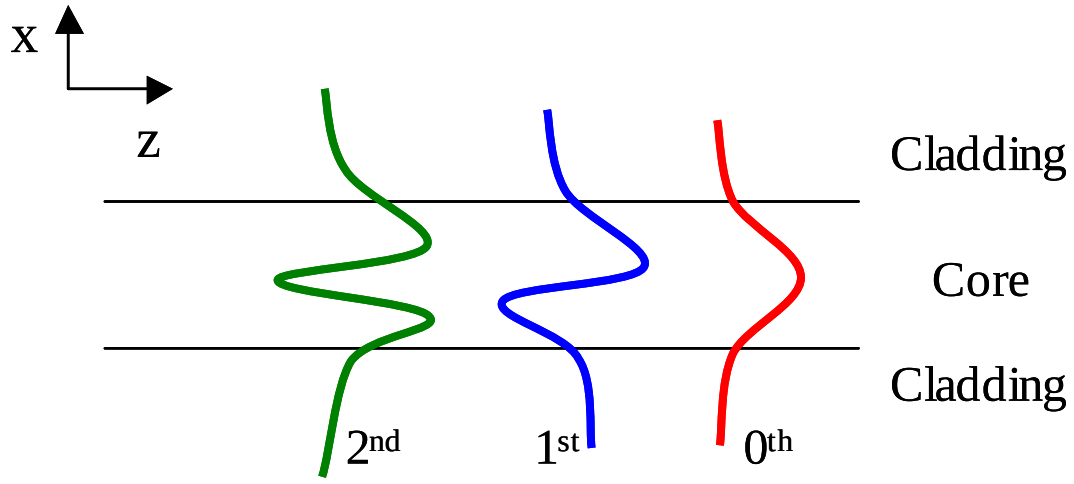

Fig. 2.8. TE mode in a slab waveguide, from Guangwei Yuan's dissertation.

In practice, the waveguide modes will attenuate in the light propagation direction due to the loss in the waveguide. There are three loss mechanisms in a straight optical waveguide: absorptive loss, leaky mode loss and scattering loss. The absorptive and leaky mode loss can be minimized by choosing appropriate waveguide materials and structures. The scattering loss is

mostly due the roughness of interfaces introduced in the fabrication process. The propagation constants now have both real and imaginary part as $\beta_m = \beta_{mr} + i\beta_{mi}$. The imaginary part of the propagation constant determines the attenuation rates, $\alpha_m = 10\log_{10}(e)\beta_{mi}$, the 10log10(e) factor allows the loss to be expressed in dB.

$$\beta_i = \frac{1}{x}\ln(E_x / E_0) \ , \qquad \alpha = \frac{10}{x}\log_{10}(E_x / E_0) = 4.3\beta_i \tag{2.13}$$

2.3 Characterization methodologies

For decades, there were a couple of experimental methodologies most frequently used in optical waveguide characterizations to investigate the properties such as propagation losses, evanescent field perturbations and modal interference. Far-field scattering measurement and near-field evanescent measurement are two of the most important measurement methods.

2.3.1 Far-field scattering measurement

The far-field scattering measurement is mainly used to find the attenuation constant of a waveguide. Long before the near field optical scanning microscopy (NSOM) became a well-developed technique, far-field scattering measurement has been developed into a relatively accurate and easy to use tool to characterize the waveguide devices.

The far-field scattering measurement is based on the assumption that the scattered light in the far field remains a fixed ratio to the light power still confined in the waveguide core. The far-field microscope setup is illustrated in Figure 2.9. The glass fiber with one open end is mounted on a mechanical translation stage to scan in one dimension along the waveguide length. Scattered light is coupled into the open end and fed into a highly sensitive photodetector located at the other open end of the fiber. A major problem of this method is difficulty to maintain the fiber tip over the top of the waveguide at a constant distance, and hence the measured results are not accurate when the sample has some features on it.

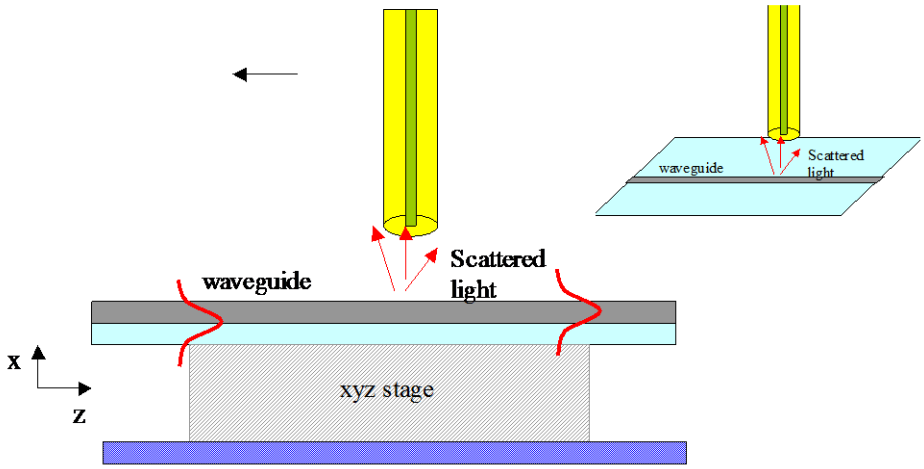

Fig. 2.9. Setup of far-field scanning microscope.

Figure 2.8 (a) shows a far field scanning system developed by the Optoelectronics Research Group at Colorado State University [18]. Here the scanning tip uses a cleaved multimode fiber with 125 μm cladding diameter and 50 m core diameter. The cleaved fiber tip was mounted on a tuning fork shown in Fig. 2.10(a). A motorized translation stage controls the height of the tip and position in the X-Y plane, as shown in Fig. 2.10(b). Fig. 2.11(a) shows far field intensity image of a 4 μm wide straight waveguide. Unlike conventional one-dimensional scanning, far field intensity was measured in the X-Y plane in an area of 80 μm x 90 μm. The red dashed line denotes the centerline of the waveguide. The far-field intensity image shows a Gaussian-like profile. The far field light intensity along the centerline of the waveguide was plotted with the solid line in Figure 2.11(b). The fit curve (dashed line) shows a 13.5 dB/mm intensity decay rate along the waveguide propagation direction.

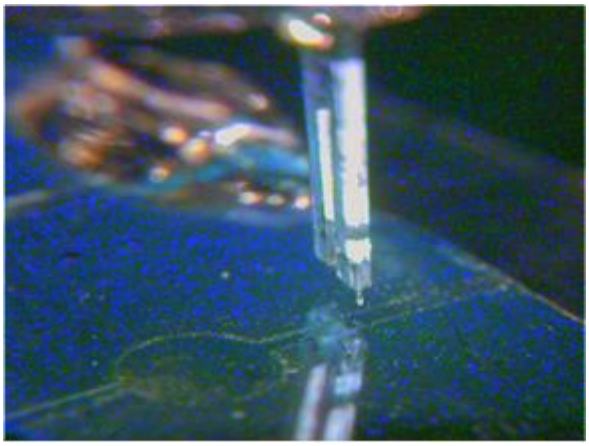

(a)

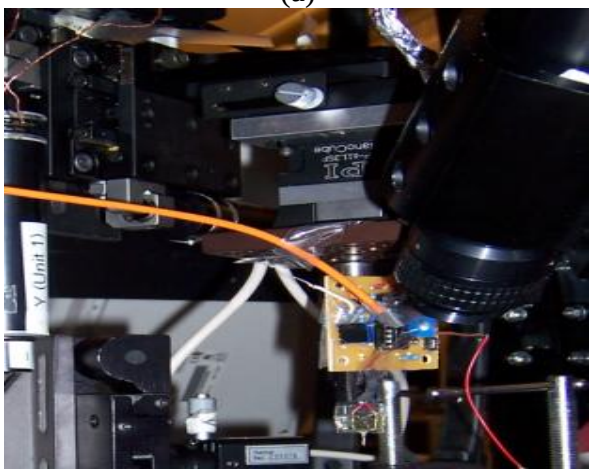

(b)

Fig. 2.10 a) A far field scanning system developed by the Optoelectronics Research Group, Colorado State University b) The cleaved fiber tip mounted on a tuning fork.

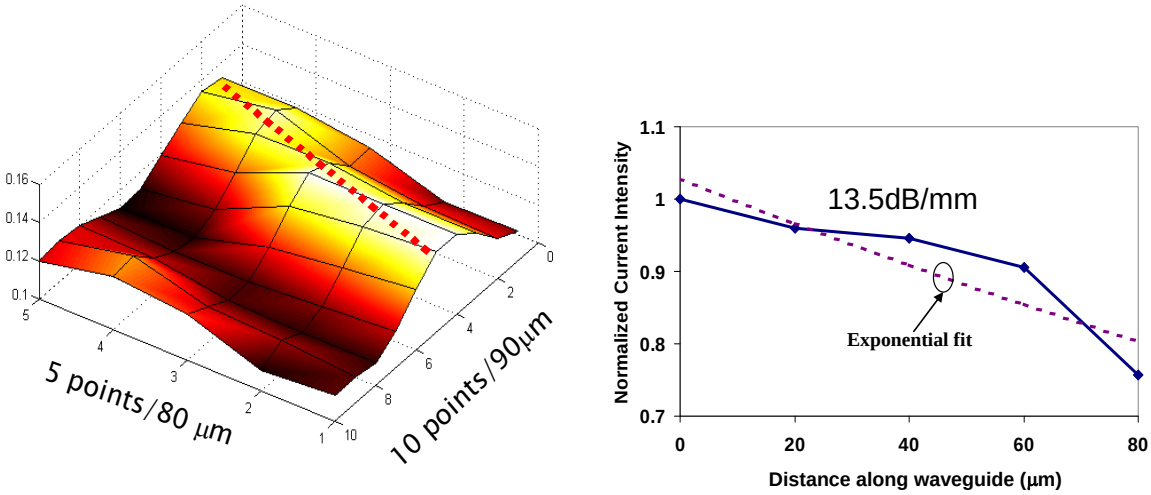

(a) (b)

Fig. 2.11. a) Far field intensity image of a 4 μm wide straight waveguide. The red dashed line denotes the centerline of the waveguide. b) The far field light intensity along the centerline of the waveguide (solid).

2.3.2 Near field scanning optical microscope

In a classical far-field microscope, resolution is limited by the overlap of the field distributions which are circular symmetry to the image points. It is dominated by a central bright spot whose diameter is proportional to $\lambda/n\sin\theta$, surrounded by a series of rings with decaying intensity as a function to the distance with respect to the center. The quantity $n\sin\theta$ is called the numerical aperture (NA) of the microscope objective. Here it has the same definition as we discussed before in the waveguide Section 2.2.2. It describes the max angle an optical system can accept. High resolution microscope objectives can have NA as high as 0.95 - 1.4, depending on the optical index of the medium between the sample and the objective.

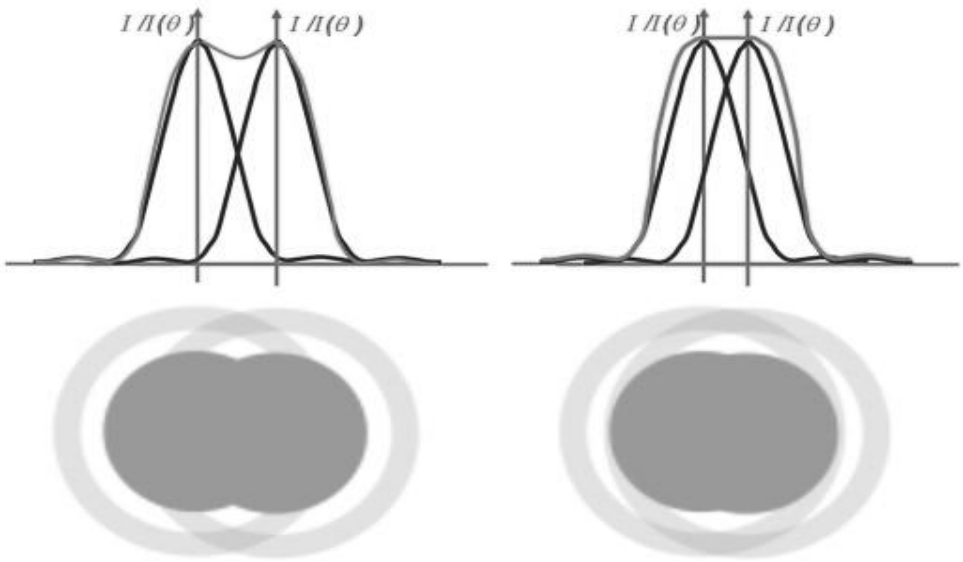

Fig. 2.12 Resolution limit of classical microscopy according to Rayleigh's criterion. When the distance between the two source points is smaller than $\Delta r=1.22\lambda/2NA$, the overlap of the field distribution prevents one from resolving the image of the two points individually. The lower part of the figure shows the microscope views of the image of the source points separated by a distance larger or smaller than Δr. [Image reproduced from http://astronomy.swin.edu.au/cosmos/R/Resolution]

The resolution limit in classical microscopy is generally expressed by Rayleigh's criterion (Fig. 2.12). According to diffraction theory, when the distance between two spots is smaller than Δr, which is given by Equ. 2.14, the image of the two spots could not be distinguished.

$$\Delta r = 1.22\frac{\lambda}{2n\sin\theta} = 1.22\frac{\lambda}{2NA} \tag{2.14}$$

According to Rayleigh's criterion, Δr gives the size of the smallest detail of the object which can be resolved with a classical microscope. Using visible illumination ($\lambda \approx 500$ nm) the best microscopes achieve a resolution which is typically of the order of 250 nm.

In contrast to the far-field scanning method, near-field evanescent measurement techniques provide a means not only of tracking waveguide losses but also obtaining higher resolution information, such as mode profiles. The local field change due to introduction of the sub-wavelength scale object, such as the bio molecular, small defects, abrupt interfaces, or refractive index change could be accurately monitored by this much more complicated system. What's more, the scanning on the device also provides the topographic data of the surface, which benefits study of the relationship between the geometric change along the waveguide and the evanescent field distribution change.

Fig. 2.13 describes the basic principle of an NSOM. According to the discussions above, to obtain an optical image of a nanostructured sample with subwavelength resolution, the information must be collected from the near field. As optical detectors are generally installed in the far-field, the subwavelength probe in NSOM plays the role of an optical transducer that transfers the near field at the probe's location into the far field towards the detector. The recording of the near-field measured at each new location of the probe during scans produces an optical image of the surface with a resolution determined by the probe's size.

One of the most important problems that needs to be solved in building a NSOM is how to keep distance between the sub-wavelength probe and the sample surface a constant value. Several different sensing and feedback systems, including cantilever feedback system, optical reflection feedback system and shear-force feedback system, have been applied to the NSOM[9][19][20]. Most of the NSOM results in our study are measured using the WITec NSOM system operated by optical feedback mechanism which consists of a secondary laser source and a quadrant photodetector. A shear-force feedback system based on the damping of a

tuning fork has been applied to the home-brew SPM system that is still under construction in our lab. It will be discussed in my PhD dissertation.

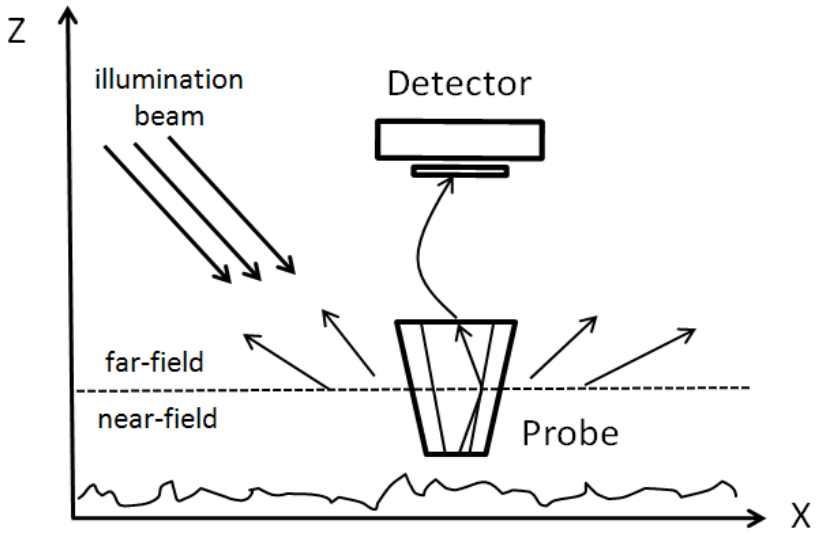

Fig. 2.13. Principles of NSOM.

References:

[1] E. Snitzer and H. Osterberg, "Observed Dielectric Waveguide Modes in the Visible Spectrum," *Journal of the Optical Society of America,* vol. 51, May. 1961, pp. 499-505.

[2] A. Yariv and R.C.C. Leite, "Dielectric-waveguide mode of light propagation in p-n junctions," *Applied Physics Letters,* vol. 2, Feb. 1963, pp. 55-57.

[3] P.K. Tien, R. Ulrich, and R.J. Martin, "modes of propagating light wave in thin deposited semiconductor films," *Applied Physics Letters,* vol. 14, May. 1969, pp. 291-294.

[4] M.L. Dakss, L. Kuhn, P.F. Heidrich, and B.A. Scott, "Grating coupler for efficient exictation of optical guided waves in thin films," *Applied Physics Letters,* vol. 16, Jun. 1970, pp. 523-525.

[5] D. Keck, P. Schultz, and F. Zimar, "Attenuation of multimode glass optical waveguides," *Applied Physics Letters,* vol. 21, 1972, pp. 215-217.

[6] T.C. Rich and D.A. Pinnow, "Total Optical Attenuation in Bulk Fused Silica," *Applied Physics Letters,* vol. 20, Apr. 1972, pp. 264-266.

[7] A.R. Tynes, A.D. Pearson, and D.L. Bisbee, "Loss Mechanisms and Measurements in Clad Glass Fibers and Bulk Glass," *Journal of the Optical Society of America,* vol. 61, Feb. 1971, pp. 143-153.

[8] A. Jacobsen, N. Neuroth, and F. Reitmayer, "Absorption and Scattering Losses in Glasses and Fibers for Light Guidance," *Journal of the American Ceramic Society,* vol. 54, 1971, pp. 186-187.

[9] D.W. Pohl, W. Denk, and M. Lanz, "Optical stethoscopy: Image recording with resolution lambda/20," *Applied Physics Letters,* vol. 44, Apr. 1984, pp. 651-653.

[10] M.L.M. Balistreri, A. Driessen, J.P. Korterik, L. Kuipers, and N.F. van Hulst, "Quasi interference of perpendicularly polarized guided modes observed with a photon scanning tunneling microscope," *Optics Letters,* vol. 25, May. 2000, pp. 637-639.

[11] S. Bourzeix, J.M. Moison, F. Mignard, F. Barthe, A.C. Boccara, C. Licoppe, B. Mersali, M. Allovon, and A. Bruno, "Near-field optical imaging of light propagation in semiconductor waveguide structures," *Applied Physics Letters,* vol. 73, 1998, pp. 1035-1037.

[12] X. Borrise, D. Jimenez, N. Barniol, F. Perez-Murano, and X. Aymerich, "Scanning near-field optical microscope for the characterization of optical integrated waveguides," *Lightwave Technology, Journal of,* vol. 18, 2000, pp. 370-374.

[13] K. Karrai and R.D. Grober, "Piezoelectric tip-sample distance control for near field optical microscopes," *Applied Physics Letters,* vol. 66, Apr. 1995, pp. 1842-1844.

[14] G.H. Vander Rhodes, B.B. Goldberg, M.S. Unlu, S.T. Chu, W. Pan, T. Kaneko, Y. Kokobun, and B.E. Little, "Measurement of internal spatial modes and local propagation properties in optical waveguides," *Applied Physics Letters,* vol. 75, Oct. 1999, pp. 2368-2370.

[15] A.L. Campillo, J.W.P. Hsu, K.R. Parameswaran, and M.M. Fejer, "Direct imaging of multimode interference in a channel waveguide," *Optics Letters,* vol. 28, Mar. 2003, pp. 399-401.

[16] J.N. Damask, *Polarization optics in telecommunications*, Springer, 2004.

[17] R. Yan, G. Yuan, M.D. Stephens, X. He, C.S. Henry, D.S. Dandy, and K.L. Lear, "Evanescent field response to immunoassay layer thickness on planar waveguides," *Applied Physics Letters*, vol. 93, 2008, pp. 101110-3.

[18] R. Yan, G. Yuan, R. Pownall, and K.L. Lear, "Waveguide Characterization Using Shear Force Scanning Optical Microscopy.," *American Physics Sociaty*, vol. 2007 APS March Meeting Volume 52, Number 1 .

[19] E. Betzig, J.K. Trautman, T.D. Harris, J.S. Weiner, and R.L. Kostelak, "Breaking the Diffraction Barrier: Optical Microscopy on a Nanometric Scale," *Science*, vol. 251, Mar. 1991, pp. 1468-1470.

[20] R. Brunner, A. Bietsch, O. Hollricher, and O. Marti, "Distance control in near-field optical microscopy with piezoelectrical shear-force detection suitable for imaging in liquids," *Review of Scientific Instruments*, vol. 68, Apr. 1997, pp. 1769-1772.

Chapter 3

REVIEW OF LABEL-FREE OPTICAL BIOSENSING TECHNOLOGIES

3.1 Introduction of the biosensing technologies

To design a biosensor, different elements need to be considered, such as transducer optimization (increasing sensitivity and decreasing noise level), fluidic design (sample injection and drainage, reduction of sample consumption, reduction in detection time, etc.), surface immobilization chemistry (analyte capture efficiency, elimination of non-specific binding, etc.), detection format (direct binding, sandwich-type binding, etc. shown in Fig. 3.1.) [1]. Among all of these elements, the choice of transducer type is one of the most important, and the biosensors could be categorized into several basic types by the adoption of different transducers, such as optical biosensor, electrochemical biosensors, mass sensitive (piezo property change) biosensors, thermoelectric biosensor and magnetic-based biosensor.

Optical biosensors have many advantages over other kinds of the biosensors, such as they are immune to electromagnetic interference, capable of performing remote sensing, and some of them can provide multiplexed detection within a single device. All of these advantages make the

optical biosensors powerful tools for applications in many fields, including health-care, environment monitoring, biomedical R&D and even homeland securities [2]-[7].

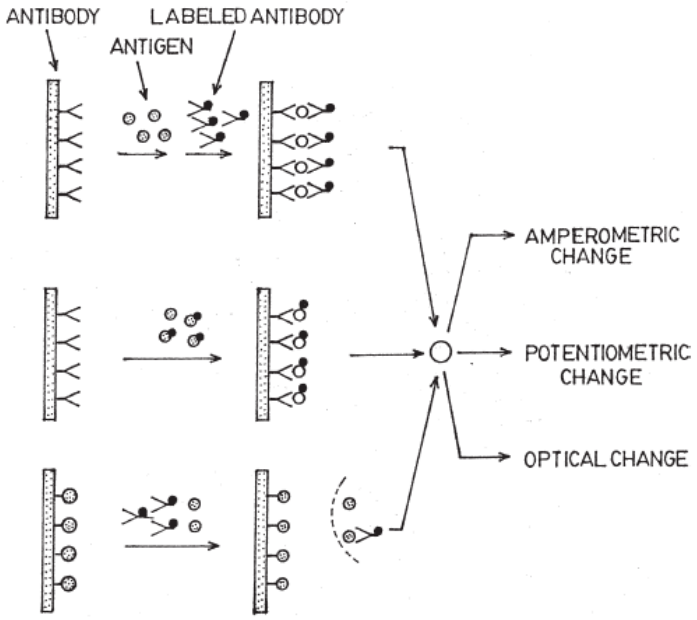

Fig. 3.1. Different detection format for labeled biosensors Reproduced from [1].

Generally, optical biosensors can be categorized into two types: fluorescent-based biosensors and label-free optical biosensors. In fluorescent-based detection, either target molecules or receptor molecules are labeled with fluorescent tags, such as fluorescein isothiocyanate (FITC). The measured intensity of the florescent light shows the presence of the target molecules and the interaction of the target molecules and the receptor molecules. A fluorescent-based biosensor could be extremely sensitive [8]. However, three major disadvantages largely limit its applications. First, laborious labeling processes before the detection may interfere with the function of the biomolecules and hence change some of the properties of the molecules. Second, since it is difficult to accurately control the number of fluorophores on each molecule,

quantitative analysis could be very challenging for fluorescent-based biosensing. Third, detection of fluorescence requires sophisticated and moderately expensive instrumentation including powerful, narrow wavelength range excitation sources such as lasers, sensitive fluorescence detectors or imagers, and optical systems for illumination, collection, and filtering light.

In contrast, there is no need to label or alter the target molecules in label-free biosensing technologies, and hence the detection can be carried out with the molecules in their natural forms, which makes the detection relatively easy and cheap to perform, and allows quantitative measurement of the molecular interactions.

Two different detection methods are usually adopted by label-free optical biosensors: refractive index (RI) detection and optical absorption detection. RI and absorption detection detect the change of real and imaginary part of the more general complex RI constant and they are related via the Kronig-Kramers (KK) relations.

In this chapter, we will limit our discussion to the RI-based label-free detection. Some of the RI based sensor could be used to detect both bulk solution RI change (refractometer) or the RI change induced by molecular binding which happens on the sensor surface (biosensor), while some other sensors could only detect bulk solution RI change

Fig. 3.2 shows a conceptual label-free biosensor. When target molecules captured by the receptor molecules immobilized on the sensor surface, the original solution molecules are replaced with the target biomolecules in these positions and hence the refractive index several to tens of nanometer above the sensor surface is changed due to the RI difference between the target molecules (~1.55) and the solution molecules (~1.33 for water and 1 for air). The RI

change could be detected optically and converted to electrical signal by the transducer. Thus, as mentioned above, optical biosensors usually need the light field to be confined near the sensor surface in order to detect only the molecules captured near the sensor while ignoring all the other molecules in the solution far from the surface. The evanescent field exponentially decays into the solution and the penetration depth is determined by the RI of the solution, and is usually shorter than the light wavelength, which makes it proper for biosensing applications. Actually, most of the popular label-free optical biosensors, including SPR biosensor, ring-resonator biosensor and MZI biosensor, are based on evanescent field detection with different optical structures.

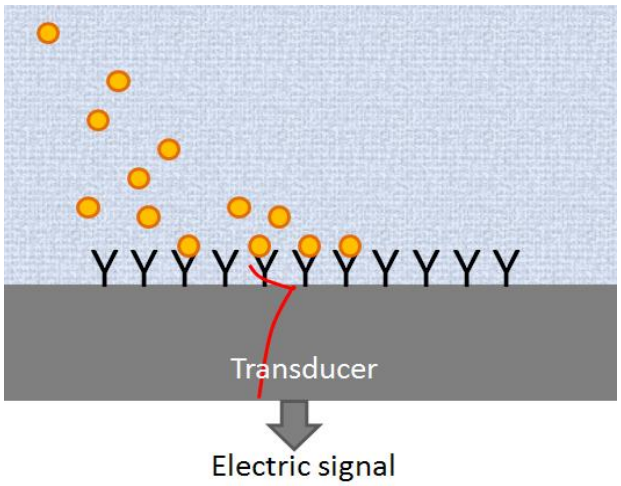

Figure 3.2. Conceptual demonstration of label-free optical biosensor.

Before discussing detailed different label-free optical biosensors, several biosensor terms need to be clarified. Sensitivity is an important parameter to estimate the biosensor's performance. It is defined as the signal change produced by the transducer in response to the change of analyte per unit. Physically it represents how strong the light-matter interaction is, and in most evanescent field based biosensors, the fraction of the light power in the solution

determines the sensitivity, so in most cases, the sensitivity could be increased by increasing the fraction of light near the sensing surface. For the LEAC biosensor, this is not totally true, since in the LEAC sensor, on the one hand, evanescent field is used to interact with analyte to sense the change of analyte, just like other biosensors. On the other hand, unlike other biosensors where the far field light is detected to measure the evanescent field indirectly, the evanescent field below the waveguide is directly used to the sense the change on the other side of waveguide. Hence the LEAC biosensor design requires some special waveguide structures compared with other waveguide design. More details will be discussed in Chapter 4.

Noise level is another key parameter to characterize the performance of the sensor. For most label-free optical biosensors, the most common noise is from temperature fluctuations, which result in the thermal-optic effect (RI change induced by temperature change) and the thermo-mechanic effect (thermal expansion) in the sensor or in the solution. The most direct method to minimize this kind of noise is to use temperature control equipment, such as a thermoelectric cooler to stabilize the temperature. Another method is to cancel the thermo-optic and thermo-mechanic effects by using solvents that have negative thermo-optic coefficients to counteract the positive thermo-optic coefficient of the solid sensor structure. A third method is to employ a reference channel, such as in a MZI biosensor, where a "duplicate" waveguide structure is built into the same sensor to act a reference signal detector[9]. Similar strategy is adopted in the LEAC sensor measurement.

Limit of detection (LOD) is usually defined as 3×standard deviation (SD), and it represents the lowest quantity of a substance that can be distinguished from the absence of that substance (a blank value). For label-free optical biosensors with different detecting principles, there are

different ways to specify the LOD. First, since all these sensors are sensitive to a RI change in a bulk solution, LOD in units of refractive index units (RIU) is the most commonly used to evaluate the sensor's performance, and hence provide a rough standard to compare the performance for different biosensors. The second kind is to use the physical properties of the analytes measured by the biosensor to mark the unit of LOD, such as the surface mass density in units of pg/mm^2, and adlayer thickness in unit of nm. While experimentally determinations of these properties are difficult (usually requiring some special characterization tools, such as AFM or NSOM), these units reflect the intrinsic detection capacity of a sensor and could be used to compare the performance of the sensors with similar detection mechanisms. The third way, which is the most direct way, is the use sample concentration. Concentration of the analyte is very easy to determine from an experimental point of view. However, the LOD defined in this way depends on the target molecule and its receptor biomolecules, and hence needs to be specified for different biomolecules.

In the past 20 years, different kinds of the label-free optical biosensors have been proposed and studied, such as surface plasmon resonance biosensors, interferometer biosensors, ring resonantor biosensors, optical-fiber based biosensors, photonic crystal biosensors and other biosensors based on hybrid structures. In this chapter, three types of biosensors, including the SPR biosensor, MZI biosensor and ring resonator based biosensor, are reviewed, since they represent the major interests in both academic research and practical applications.

3.2 Surface plasmon resonance biosensors

The surface plasmon resonance (SPR) phenomenon has been studied from the 1920s [10][11] and was first demonstrated for biosensing application in 1983 by Liedberg et al.[12]. Since then, the SPR biosensor has gradually become one of the most widely explored and most powerful label-free optical biosensors.

Surface plasmons are surface electromagnetic (EM) waves that propagate in a direction parallel to the metal/dielectric interface based on the interactions of the EM wave and electrons in the metal, as shown in Fig. 3.3.

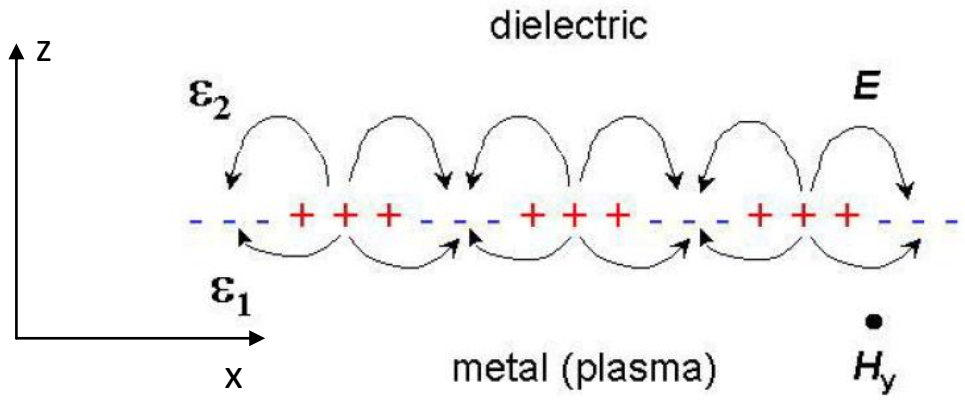

Fig. 3.3. The structure of fields and charges in the surface EM wave at the dielectric/metal interface.

The E-field in such structure could be expressed as

$$E(x,z) = \exp[i(kx-\omega t)]\exp[-(k^2-\varepsilon_2\frac{\omega^2}{c^2})^{1/2}z] \quad \text{when } z \geq 0 \tag{3.1}$$

$$E(x,z) = \exp[i(kx - \omega t)]\exp[+(k^2 - \varepsilon_1 \frac{\omega^2}{c^2})^{1/2} z] \quad \text{when } z \leq 0 \tag{3.2}$$

The boundary condition require continuity of the normal components of B at Z = 0. As the result:

$$\varepsilon_1 (k^2 - \varepsilon_2 \frac{\omega^2}{c^2})^{-1/2} = -\varepsilon_2 (k^2 - \varepsilon_1 \frac{\omega^2}{c^2})^{-1/2} \tag{3.3}$$

This can be true only if $\varepsilon_1 < 0$, which requires that material 1 is a metal. Solving the equation, we get the dispersion relationship as:

$$k_x = \frac{\omega}{c}[\frac{\varepsilon_1(\omega)\varepsilon_2}{\varepsilon_1(\omega) + \varepsilon_2}]^{1/2} \tag{3.4}$$

For metal, the relationship between dielectric constant and frequency is shown in Fig. 3.4(a). Form the dispersion relationship shown in Fig. 3.4(b), the wave vector of SPR supported in the dielectric and metal interface is smaller than that of the light propagating in the dielectric (blue curve, $k_x = \omega\varepsilon_2^{1/2}/c$). This indicates it is impossible to excite the SPR from the dielectric directly.

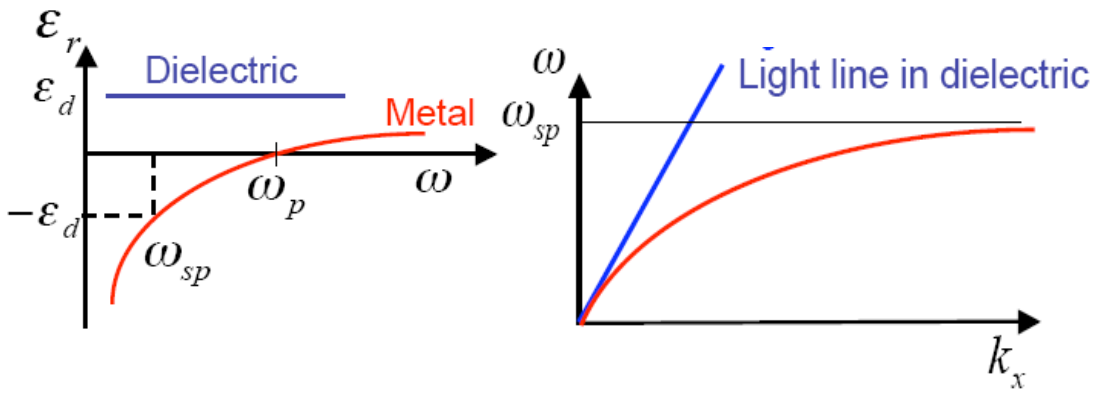

Fig. 3.4. (a) dielectric constant for metal (b) dispersion relationship of SPR. Reproduced from https://nanohub.org/resources/1748.

As shown in Fig. 3.5(a), to get a cross between the excitation light and SP wave, we need to increase the wave vector of the excitation wave while keeping the SP wave has the same dispersion relationship. The simplest way to realize this is to use a glass prism structure as shown in Fig. 3.5(b). The light polarized in plane of incidence forms total internal reflection at the interface of glass and metal. SP wave is excited at the other interface (metal/air) at certain angle, as shown in Fig. 3.5(c).

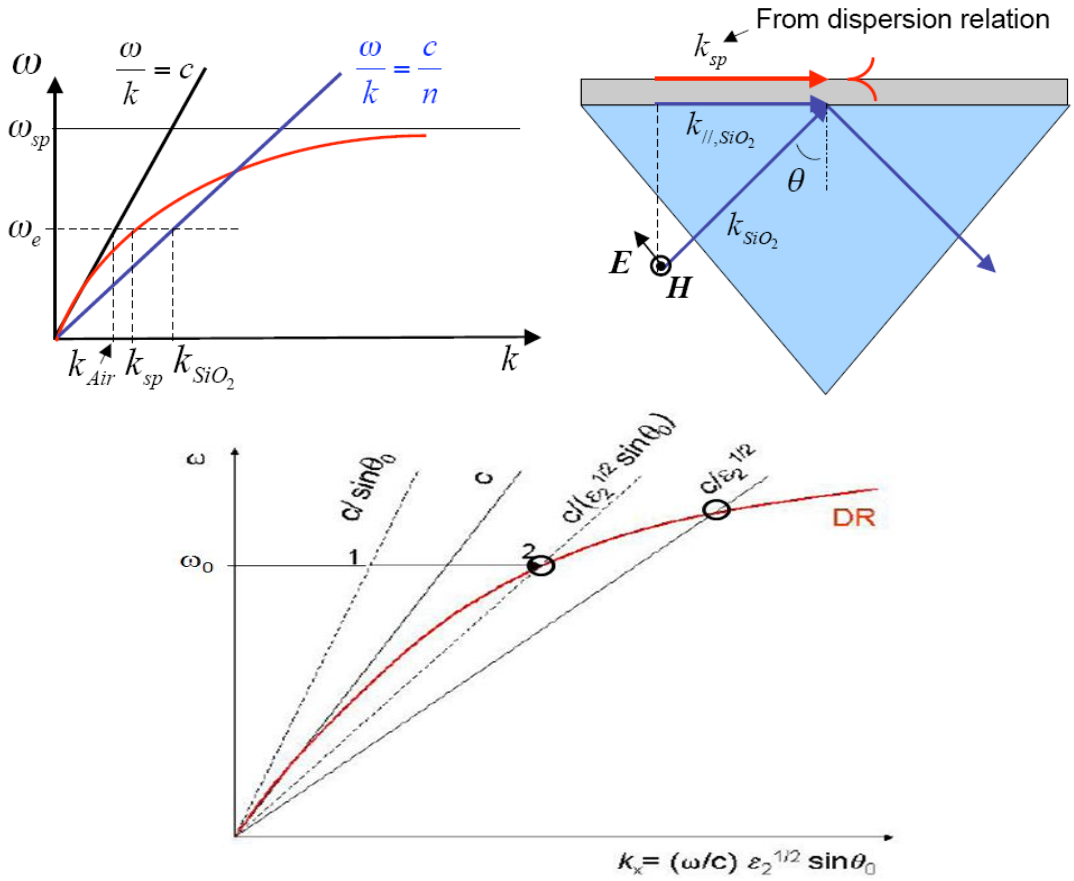

Fig. 3.5. Excitation of SPR with a prism (a) dispersion relationship of SPR and the light in air and glass (b) prism structure (c) when the incident angle makes the crossing point's frequency equal to the frequency of the incident light, SP is excited. Reproduced from https://nanohub.org/resources/1748.

Prism coupling was the first practical configuration for SPR biosensing[12] and has now become the most widely-studied SPR biosensor type[13][14]. Commercialized SPR sensors, such as the Biacore series[15], are typically based on prism coupling and have a LOD between 1×10^{-6} to 1×10^{-7} RIU and a mass surface density LOD around 1 pg/mm^2.

Although prism coupling usually has the best sensing LOD, the prism is bulky and it is difficult to integrate into a compact system. As shown in Fig. 3.6, three other excitation methods have been proposed and developed to provide alternatives to the prism, and they are waveguide coupling, fiber optic coupling, and grating coupling[16][17].

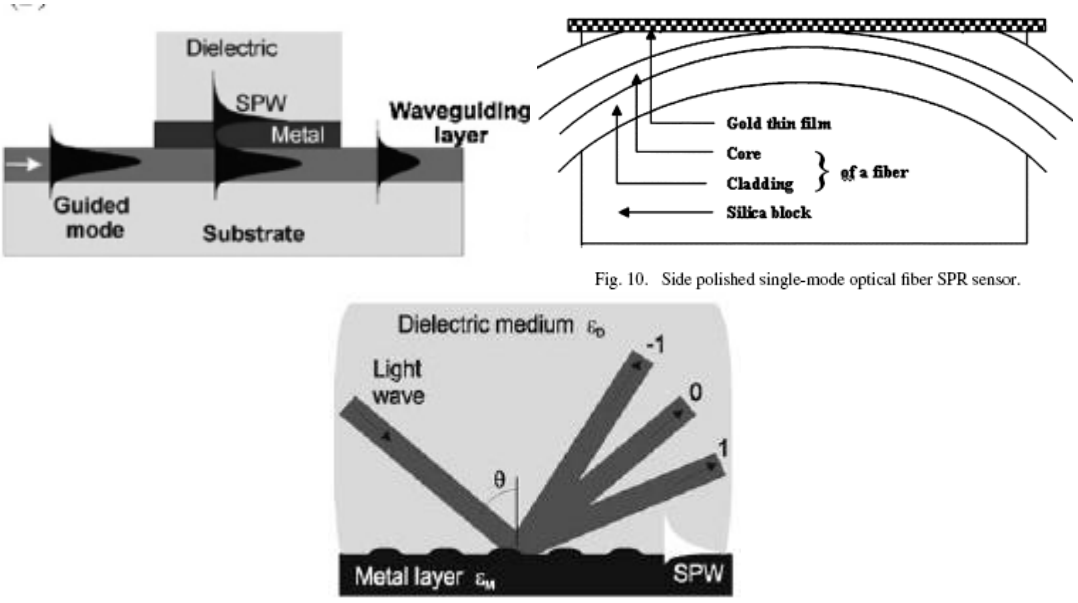

Fig. 3.6. Waveguide-based, fiber coupled and grating coupled SPR biosensors Reproduced from [16][17].

A waveguide is easy to fabricate and to integrate with other optical and electrical components. As discussed in Chapter 2, the total internal reflections (TIR) happen at the

waveguide boundaries when the guided light propagates in a waveguide, and just like what happens in the prism coupling, the evanescent field at the waveguide-metal interface excites the SP wave, as shown in Fig. 3.6. In waveguide-based SPR biosensors, the LOD is usually from 10^{-5} to 10^{-6} RIU[18][19].

Optical fibers are also used to excite the SP wave in a relatively easy and flexible way. In most of these sensors, a small portion of the fiber is removed and then coated with a layer of metal film. For optical fiber coupled SPR biosensors, the typical LOD is around 10^{-5} to 10^{-6} RIU[20][21].

Grating coupling, which can be mass produced with low cost, could also be used to excite the SP waves. The excitation principle for grating coupling is a little different from the other three. A light wave is incident on a metallic grating. If the momentum of diffracted light parallel to grating surface is the same as the propagation constant of the surface plasmon, the light will be coupled into the SP wave as described below:

$$\frac{2\pi}{\lambda} n_2 \sin\theta + m\frac{2\pi}{\Delta} = \pm k_{sp} \tag{3.5}$$

where n_2 is the dielectric medium RI, m is an integer indicating the diffraction order and Δ is the grating period. Because the incident light directly illuminates the metal surface, the sample solution is required to be transparent for the applied wavelength. The LOD of grating coupling biosensors ranges from 10^{-5} to 10^{-6} RIU[22][23].

The detection of the SPR change due to the binding of the target molecules could use the change of resonant angle, resonant wavelength or resonant intensity change[16][24][25].

SPR biosensors usually have high sensitivities; however, there still exist some potential problems that will limit their applications in some field. First, since detection is based on a resonance structure, SPR bisoensors are usually very sensitive to temperature fluctuations or wavelength variations. Second, the evanescent field in these sensors only penetrates into the surrounding medium for ~100nm, and hence it is difficult to detect the large target objects like cells and bacteria.

3.3 Mach-Zehnder Interferometer (MZI) biosensors

Interferometer based biosensors, such as MZI biosensors, Young's interferometer sensors[26][27] and Hartman interferometer sensors[28], have attracted a lot of attention in the label-free optical biosensor research area since the 1980s. Among these interferometer based biosensors, the MZI biosensor is the most widely studied one.

Fig. 3.7 shows the operating principle of the integrated MZI. Polarized laser light is coupled into the input waveguide and is split equally into the sensing arm and the reference arm at the Y-splitter. On the sensing arm, a window is opened over the top of the waveguide to allow it contact the samples, while on the reference arm, a protective layer usually covers the waveguide to "seal" the waveguide from the environment to prevent samples or any possible contamination from reaching this region. The two arms combine at the output waveguide, and a photodetector is used to detect the light intensity.

A change in RI above the surface of the waveguide in the sensing arm results in an optical phase change, ΔΦ, and the phase change will lead to a light intensity change at the output of the waveguide in the relationship of

$$P_{out} = P_0 \cos^2(\frac{\Delta\Phi}{2}) = \frac{P_0}{2}(1+\cos\Delta\Phi) \ , \ \ \Delta\Phi = \Delta n \ k_0 L \quad (3.6)$$

Where P_0 is the input power, Δn is the effective RI change, k_0 is the wave vector and L is the length of the sensing are on the sensing waveguide. Typically, increasing the length of the sensing window increases the sensing signal. However, since the cosine-dependent intensity function, the signal change is not easily observed near the maximum and minimum of the cosine function. This is a built-in disadvantage of MZI device compared to sensors that have the linear intensity response. Work by Heideman's group[29] in 1999 proposed a method to eliminates this problem by tracking the quadrature points, where $\Delta\Phi=(n+1/2)\pi$, instead of the output intensity. By modulating the phase change on the reference arm to track the quadrature points, phase change due to the sample existence can be determined.

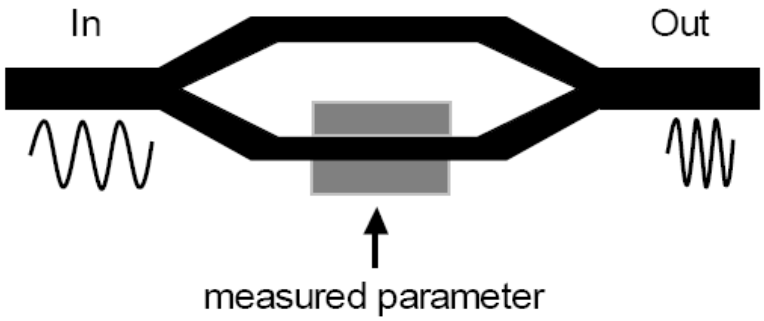

Fig. 3.7. MZI bionsensor.

The first biosesning demonstration using an integrated MZI was proposed by Heideman, et al.[30]. A SiN_x waveguide on a Si substrate was used to create a MZI structure. The RI LOD demonstrated experimentally in the paper was $\sim 4 \times 10^{-6}$ RIU. An antibody for human chorionic gonadotropin (hCG) was used to test the sensor, and LOD was 50pM hCG.

As mentioned before, temperature fluctuation and other unpredictable RI change in the sensor structure are the major noise source for label-free optical biosensors. Schipper, et al.'s [9]work in the early 1990s demonstrated the reference arm of MZI can be used to cancel out some major factors that caused the unwanted RI change, such as the temperature fluctuations and non-specific adsorptions. A specially designed microfluidic system was used to allow different surface treatments on each of the exposed arms. One was used as the sensing arm and another was used as the reference arm to cancel out the non-specific binding noises. The LOD of this MZI was $\sim 10^{-5}$ RIU.

Since the waveguide in a MZI biosensor needs to be single mode to avoid multimode interference, the thickness of the waveguide is usually limited to the order of 100 nm. This causes high loss at the input coupling interface, and highly decreased the power of the guided light in the waveguide. Jimenez et al.[31] proposed a structure based on one well-studied antiresonant reflective optical waveguide (ARROW) [32] architecture that can achieve single-mode behavior with micrometer dimensions. Unlike a traditional TIR-based waveguide structure, an ARROW relies on the interference reflection in the alternating layers below the waveguide to filter out the higher modes while keeping the fundamental mode with low loss propagating along the waveguide. Besides decreasing the coupling loss, ARROW structured also help to push more light above the surface of the waveguide, which benefits the sensitivity of

MZI biosensors since this increases the fraction of power distributed into the evanescent field in the sensing region, as discussed in Section 3.1.

In recent publications, the merging of SPR biosensors with MZI detection principles[33] is also an interesting topic in this research area.

3.4 Ring resonator based biosensors

Because a ring resonator based biosensor could provide extreme high sensitivity with relatively small geometric size and some types have the potential to be mass produced with high density integration, intensive investigation has been put on the optical ring resonator based biosensors in recent years[34][35].

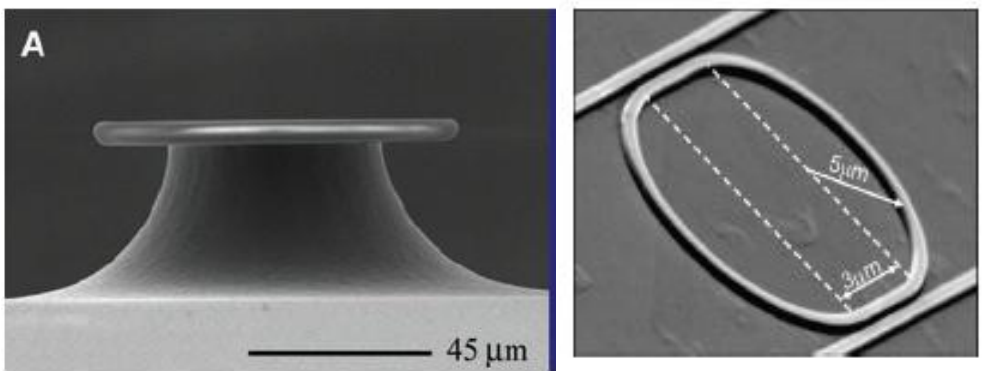

Fig. 3.8. Ring based resonators [34][35].

The detection principle of ring resonator based biosensors (Fig. 3.8) is based on the direct or indirect detection of the whispering gallery modes (WGM) spectral shift. In a ring resonator, the light propagates in the form of WGM modes or circulating waveguide modes, which could be

considered as WGM modes in most cases. The WGM spectral position is related to the RI of the core and cladding through the resonant condition:

$$\lambda = 2\pi r n_{eff} / m \tag{3.7}$$

where r is the ring outer radius, n_{eff} is the effective RI, and m is the mode number, an integer number. When the RI near the ring structure surface is changed due to the capture of the target biomolecule, the n_{eff} will be changed, and this lead to the WGM spectral position shift. The capture of the target biomolecule thus could be sensed by the detection system by measuring this shift directly or indirectly.

Different from MZI sensor we discussed in previous section, the effective evanescent light field-analyte interaction length is not determined by the actual device geometric size, but by the quality factor (Q factor) of the resonator.

$$Q = \frac{\omega_0}{\Delta\omega} = \frac{2\pi\nu / \lambda}{2/\tau} = \frac{\pi\nu\tau}{\lambda} = \frac{\pi L_{eff}}{\lambda_0 / n}, \qquad L_{eff} = \frac{Q\lambda_0}{\pi n} \tag{3.7}$$

where τ is the life time, n is the refractive index of the material and L_{eff} is the interaction length.

The typical Q factor of ring resonator is 10^4-10^6, so the effective interaction length of the ring resonator based biosensor is ~0.1-10cm for light wavelength of ~1μm. This feature grants the ring resonator based biosensor two advantages: (a) compared with straight waveguide based biosensor, it provides better sensitivity with similar or even smaller surface area, which lower the requirement on the sample total volume. (b) smaller surface area makes the high density

integration of this kind of biosensor possible. On the other hand, resonance based sensing principle makes it is sensitive to the temperature fluctuations discussed in Section 3.1.

For the ring resonator based biosensors, three major configurations have been well studied: (a) chip-based microring/disk shaped resonator based biosensors[34][35][36] (b) stand-alone microsphere resonator based biosensors[37][38][39] (c) capillary-based opto-fluidic ring resonator (OFRR) based biosensors[40].

The chip-based microring/disk resonator biosensors have the potential to be integrated with other optical components and be mass produced. However, their Q factors were usually limited by the surface roughness (~10^4-10^5). A polymer ring with radius of 45μm and a Q factor of 2×10^4 was reported with a LOD of 5×10^{-5} RIU[36]. In another work[35], microring cavities in silicon-on-insulator (SOI) with a Q factor of 2×10^4 demonstrated a LOD of 10^{-5} RIU for bulk solution and 10ng/ml for avidin/biotin detection. To solve the surface roughness problem, thermal reflow (CO_2 laser heating) was used to smooth the resonator surface. The Q factor of a reflowed ring resonator was reported as 10^8, and single molecule detection ability was achieved by using this sensor[34].

Since microsphere resonators have a smoother surface due to their fabrication procedures, they usually demonstrated higher Q factor[37][39]. Frank Vollmer et al showed DNA detection with a microsphere ($Q=5\times10^5$) had a LOD of 6ng/mm^2[37]. A recent work[38] studied virus detection with a microsphere both theoretically and experimentally. They investigated the LODs of microsphere resonators with different diameters excited with two wavelengths (100nm and 780nm). The lowest LOD is calculated to be 6×10^{-3}ng/cm2 for a microsphere ($Q=10^6$) with

30μm radius operated with a 780nm laser. Experiment showed the LOD was 0.2ng/cm^2 for a microsphere with 200μm radius, which agreed with the calculation results.

Microsphere based biosensors can't be the mass produced and are hard to integrate with microfluidic systems. The OFRR is new ring resonator based biosensor introduced in recent years. A capillary is used to deliver the analytes and the wall is used as the ring resonator. Its Q factor is ~10^6 and the LOD is 4pg/mm^2 as reported in reference [40].

3.5 Local evanescent array coupled (LEAC) biosensor

As discussed above, limited by their detection priniciples, most of the traditional RI based sensors cannot detect the RI change locally, suffer from strong temperature dependence, and require sophisticated and expensive external components or instrumentation. These issues complicate integration of multi-analyte versions of these biosensors into a robust chip-scale system, and hence restrict their application. If appropriate biosensor technology could be reduced to a single integrated circuit platform, it would be extremely well suited for applications including the sensing of infectious disease biomarkers. Recent experiments have demonstrated that the LEAC biosensor could also be used for virus detection. More details will be discussed in chapter 8.

The local evanescent array coupled (LEAC) biosensor concept is based on the physical phenomenon of local field redistribution when a waveguide cross-section changes in response to biofilm formation due to specific binding of molecules in localized regions. Compared to SPR biosensors or ring/disk resonator biosensors, the LEAC biosensor is a non-resonant device with

minimal temperature dependence. Furthermore, it does not require a laser source but can be operated with LEDs that offer both noise and system simplification advantages. An entire multianalyte LEAC system including optical source, detector array, integrated signal processing and telemetry electronics with a simple capillary force driven microfluidics system should occupy a volume < 1 cm^3. More details will be discussed in the following chapters.

References:

[1] S.C. Raman, M. Raje, and G.C. Varshney, "Immunosensors for pesticide analysis: antibody production and sensor development," *Critical Reviews in Biotechnology*, vol. 22, 2002, pp. 15-32.

[2] D.A. Chang-Yen and B.K. Gale, "Design, fabrication, and packaging of a practical multianalyte-capable optical biosensor," *Journal of Microlithography, Microfabrication, and Microsystems*, vol. 5, Apr. 2006, pp. 021105-8.

[3] R.D. Harris and J.S. Wilkinson, "Waveguide surface plasmon resonance sensors," *Sensors and Actuators B: Chemical*, vol. 29, Oct. 1995, pp. 261-267.

[4] M.R. Lee and P.M. Fauchet, "Two-dimensional silicon photonic crystal based biosensing platform for protein detection," *Optics Express*, vol. 15, Apr. 2007, pp. 4530-4535.

[5] C.A. Rowe, S.B. Scruggs, M.J. Feldstein, J.P. Golden, and F.S. Ligler, "An array immunosensor for simultaneous detection of clinical analytes," *Analytical Chemistry*, vol. 71, Jan. 1999, pp. 433-439.

[6] C.A. Rowe-Taitt, J.W. Hazzard, K.E. Hoffman, J.J. Cras, J.P. Golden, and F.S. Ligler, "Simultaneous detection of six biohazardous agents using a planar waveguide array biosensor," *Biosensors and Bioelectronics*, vol. 15, Dec. 2000, pp. 579-589.

[7] M. Weisser, G. Tovar, S. Mittler-Neher, W. Knoll, F. Brosinger, H. Freimuth, M. Lacher, and W. Ehrfeld, "Specific bio-recognition reactions observed with an integrated Mach-Zehnder interferometer," *Biosensors and Bioelectronics*, vol. 14, Apr. 1999, pp. 405-411.

[8] W.E. Moerner, "New directions in single-molecule imaging and analysis," *Proceedings of the National Academy of Sciences*, vol. 104, Jul. 2007, pp. 12596-12602.

[9] F. Brosinger, H. Freimuth, M. Lacher, W. Ehrfeld, E. Gedig, A. Katerkamp, F. Spener, and K. Cammann, "A label-free affinity sensor with compensation of unspecific protein interaction by a highly sensitive integrated optical Mach-Zehnder interferometer on silicon," *Sensors and Actuators B: Chemical*, vol. 44, Oct. 1997, pp. 350-355.

[10] L. Tonks and I. Langmuir, "Oscillations in Ionized Gases," *Physical Review*, vol. 33, Feb. 1929, p. 195.

[11] D. Pines and D. Bohm, "A Collective Description of Electron Interactions: II. Collective vs Individual Particle Aspects of the Interactions," *Physical Review*, vol. 85, Jan. 1952, p. 338.

[12] B. Liedberg, C. Nylander, and I. Lunström, "Surface plasmon resonance for gas detection and biosensing," *Sensors and Actuators*, vol. 4, 1983, pp. 299-304.

[13] K. Matsubara, S. Kawata, and S. Minami, "Multilayer system for a high-precision surface plasmon resonance sensor," *Optics Letters*, vol. 15, Jan. 1990, pp. 75-77.

[14] P. Fratamico, T. Strobaugh, M. Medina, and A. Gehring, "Detection of Escherichia coli 0157:H7 using a surface plasmon resonance biosensor," *Biotechnology Techniques*, vol. 12, Jul. 1998, pp. 571-576.

[15] "http://www.biacore.com/lifesciences/index.html."

[16] J. Homola, "Present and future of surface plasmon resonance biosensors," *Analytical and Bioanalytical Chemistry*, vol. 377, Oct. 2003, pp. 528-539.

[17] A. Sharma, R. Jha, and B. Gupta, "Fiber-Optic Sensors Based on Surface Plasmon Resonance: A Comprehensive Review," *Sensors Journal, IEEE*, vol. 7, 2007, pp. 1118-1129.

[18] Dostalek J., Ctyroky J., Homola J.[1], Brynda E., Skalsky M., Nekvindova P., Spirkova J., Skvor J., and Schrofel J., "Surface plasmon resonance biosensor based on integrated optical waveguide," *Sensors and Actuators B: Chemical*, vol. 76, Jun. 2001, pp. 8-12.

[19] A. Suzuki, J. Kondoh, Y. Matsui, S. Shiokawa, and K. Suzuki, "Development of novel optical waveguide surface plasmon resonance (SPR) sensor with dual light emitting diodes," *Sensors and Actuators B: Chemical*, vol. 106, Apr. 2005, pp. 383-387.

[20] M. Chiu, S. Wang, and R. Chang, "D-type fiber biosensor based on surface-plasmon resonance technologyand heterodyne interferometry," *Optics Letters*, vol. 30, Feb. 2005, pp. 233-235.

[21] R. Slavík, J. Homola, and J. Ctyroký, "Single-mode optical fiber surface plasmon resonance sensor," *Sensors and Actuators B: Chemical*, vol. 54, Jan. 1999, pp. 74-79.

[22] F. Chien, C. Lin, J. Yih, K. Lee, C. Chang, P. Wei, C. Sun, and S. Chen, "Coupled waveguide-surface plasmon resonance biosensor with subwavelength grating," *Biosensors and Bioelectronics*, vol. 22, May. 2007, pp. 2737-2742.

[23] J. Dostálek, J. Homola, and M. Miler, "Rich information format surface plasmon resonance biosensor based on array of diffraction gratings," *Sensors and Actuators B: Chemical*, vol. 107, May. 2005, pp. 154-161.

[24] X. Fan, I.M. White, S.I. Shopova, H. Zhu, J.D. Suter, and Y. Sun, "Sensitive optical biosensors for unlabeled targets: A review," *Analytica Chimica Acta*, vol. 620, Jul. 2008, pp. 8-26.

[25] J. Homola, S.S. Yee, and G. Gauglitz, "Surface plasmon resonance sensors: review," *Sensors and Actuators B: Chemical*, vol. 54, Jan. 1999, pp. 3-15.

[26] A. Brandenburg, R. Krauter, C. Knzel, M. Stefan, and H. Schulte, "Interferometric Sensor for Detection of Surface-Bound Bioreactions," *Applied Optics*, vol. 39, Dec. 2000, pp. 6396-6405.

[27] A. Ymeti, J.S. Kanger, J. Greve, P.V. Lambeck, R. Wijn, and R.G. Heideman, "Realization of a multichannel integrated Young interferometer chemical sensor," *Applied Optics*, vol. 42, Oct. 2003, pp. 5649-5660.

[28] B.H. Schneider, J.G. Edwards, and N.F. Hartman, "Hartman interferometer: versatile integrated optic sensor for label-free, real-time quantification of nucleic acids, proteins, and pathogens," *Clin Chem*, vol. 43, Sep. 1997, pp. 1757-1763.

[29] R.G. Heideman and P.V. Lambeck, "Remote opto-chemical sensing with extreme sensitivity: design, fabrication and performance of a pigtailed integrated optical phase-modulated Mach-Zehnder interferometer system," *Sensors and Actuators B: Chemical*, vol. 61, Dec. 1999, pp. 100-127.

[30] R. Heideman, R. Kooyman, and J. Greve, "Performance of a highly sensitive optical waveguide Mach-Zehnder interferometer immunosensor," *Sensors and Actuators B: Chemical*, vol. 10, Feb. 1993, pp. 209-217.

[31] D. Jiménez, E. Bartolomé, M. Moreno, J. Muñoz, and C. Domínguez, "An integrated silicon ARROW Mach-Zehnder interferometer for sensing applications," *Optics Communications*, vol. 132, Dec. 1996, pp. 437-441.

[32] T. Baba and Y. Kokubun, "Dispersion and radiation loss characteristics of antiresonant reflecting optical waveguides-numerical results and analytical expressions," *Quantum Electronics, IEEE Journal of*, vol. 28, 1992, pp. 1689-1700.

[33] G. Nemova, A.V. Kabashin, and R. Kashyap, "Surface plasmon-polariton Mach-Zehnder refractive index sensor," *Journal of the Optical Society of America B*, vol. 25, Oct. 2008, pp. 1673-1677.

[34] A.M. Armani, R.P. Kulkarni, S.E. Fraser, R.C. Flagan, and K.J. Vahala, "Label-Free, Single-Molecule Detection with Optical Microcavities," *Science*, vol. 317, Aug. 2007, pp. 783-787.

[35] K. De Vos, I. Bartolozzi, E. Schacht, P. Bienstman, and R. Baets, "Silicon-on-Insulator microring resonator for sensitive and label-free biosensing," *Optics Express*, vol. 15, Jun. 2007, pp. 7610-7615.

[36] Chung-Yen Chao, W. Fung, and L. Guo, "Polymer microring resonators for biochemical sensing applications," *Selected Topics in Quantum Electronics, IEEE Journal of*, vol. 12, 2006, pp. 134-142.

[37] F. Vollmer, S. Arnold, D. Braun, I. Teraoka, and A. Libchaber, "Multiplexed DNA Quantification by Spectroscopic Shift of Two Microsphere Cavities," *Biophysical Journal*, vol. 85, Sep. 2003, pp. 1974-1979.

[38] S. Arnold, R. Ramjit, D. Keng, V. Kolchenko, and I. Teraoka, "MicroParticle photophysics illuminates viral bio-sensing," *Faraday Discussions*, vol. 137, 2008, pp. 65-83; discussion 99-113.

[39] M.L. Gorodetsky, A.A. Savchenkov, and V.S. Ilchenko, "Ultimate Q of optical microsphere resonators," *Optics Letters*, vol. 21, Apr. 1996, pp. 453-455.

[40] J.D. Suter, I.M. White, H. Zhu, H. Shi, C.W. Caldwell, and X. Fan, "Label-free quantitative DNA detection using the liquid core optical ring resonator," *Biosensors & Bioelectronics*, vol. 23, Feb. 2008, pp. 1003-1009.

Chapter 4

BIOSENSOR DESIGN, SAMPLE FABRICATION AND EXPERIMENT SETUP

As stated in Chapter 1, point-of-care clinical diagnostics, food safety, environmental monitoring, and biosecurity applications require inexpensive, compact, rugged, and simple to operate chip-scale diagnostic tools.

Conventional optical waveguide sensor techniques such as surface plasmon resonance biosensor, MZI biosensor, ring resonator biosensor, and other waveguided based biosensor have been well investigated and some of them have been employed for biosensor applications[1][2][3][4][5][6]. However, the disadvantages of most of these techniques such as low limited number of analytes that can be simultaneously detected using a single waveguide, extremely sensitive to temperature fluctuations, as well as dependence on the expensive external equipment, restrict their applications. A novel sensor is designed for needs of detecting small volumes of multiple analytes while possessing comparable sensitivity to conventional techniques for various medical, biological and environmental situations.

4.1 local evanescent-field array coupled (LEAC) biosensor

The detection principle of the LEAC sensor is called as local field shift principle. Increased local refractive index at the waveguide's upper surface due to the formation of a biological adlayer shifts the evanescent field distribution up and hence changes the evanescent optical intensity both above and below the waveguide structure in the LEAC biosensor. The principle is illustrated in Fig. 4.1 on a proof-of-concept structure consisting of a shallow ridge waveguide made from a SiN_x core over a lower cladding of SiO_2. Nanoscale organic layers, such as those formed by the binding of target antigens or antibodies, increase the effective refractive index just above the silicon nitride waveguide core and hence shift the evanescent field profile up. The evanescent field shift can be detected by a near field scanning optical microscope above the waveguide or buried detector arrays positioned below the waveguide. To increase the light intensity modulation caused by a thin film on the waveguide surface, an asymmetric ridge waveguide structure is employed where the lower cladding has a higher index than the upper cladding and the core thickness is small enough to place the waveguide close to cutoff. As molecules bind to the upper surface of the thin core, the effective refractive index of the upper cladding increases causing both an upward shift in the guided mode as well as tighter optical confinement which increases the evanescent field decay constant in the lower cladding.

In contrast to SPR biosensors or ring/disk resonator biosensors, the LEAC biosensor is a non-resonant device with minimal temperature dependence. Furthermore, it does not require a laser source but can be operated with LEDs that offer both noise and system simplification

advantages. An entire multianalyte LEAC system including optical source, detector array, integrated signal processing and telemetry electronics with a simple capillary force driven microfluidics system should occupy a volume < 1 cm^3.

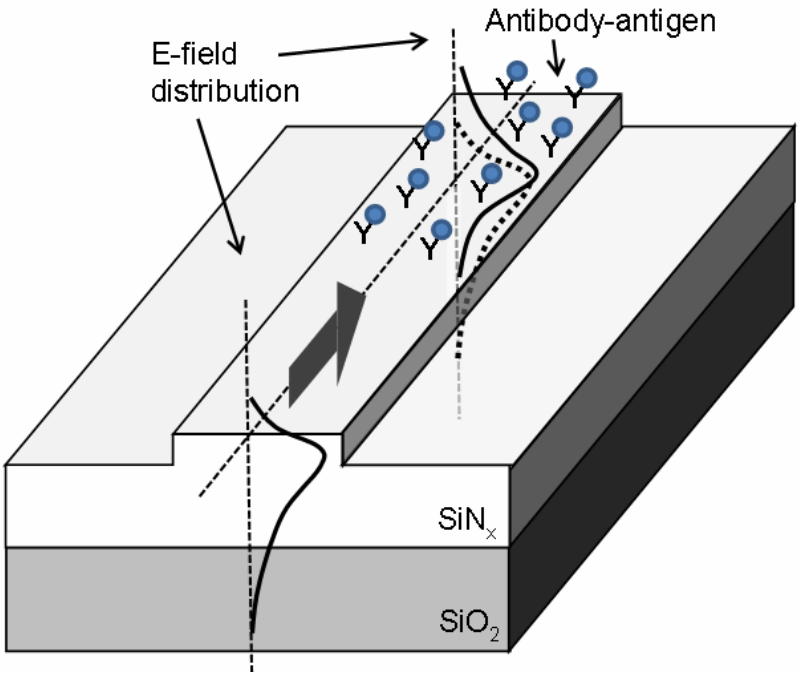

Fig. 4.1. LEAC sensor concept: the E-field shifts up when light propagates into a waveguide region covered by an adlayer. Immobilization of molecular probes such as antibodies on the waveguide surface allows sensitive detection of target molecules such as antigens via specific binding.

4.2 BPM simulation results on LEAC biosensor

As mentioned in last section, nanoscale organic layers, such as those formed by the binding of target antigens or antibodies, increases the effective refractive index just above the silicon nitride waveguide core and hence shifts the evanescent field profile away from the underlying buried detectors, reducing the associated photocurrent. An asymmetric waveguide structure amplifies the modulation of light intensity below the waveguide where the buried detector array is placed. Beam propagation method (BPM) simulations were used to study the electromagnetic field distribution of guided light in a ridge waveguide structure when organic films of different thicknesses were patterned on the waveguide surface.

In Fig. 4.2, a logarithmic plot of the electric field profiles for film thicknesses from 0 to 40 nm shows that thicker films make small normalized changes in the field strength near the core but very large relative changes at large distances from the core. The slopes of the E-field plots in the cladding are proportional to the evanescent decay constant, γ.

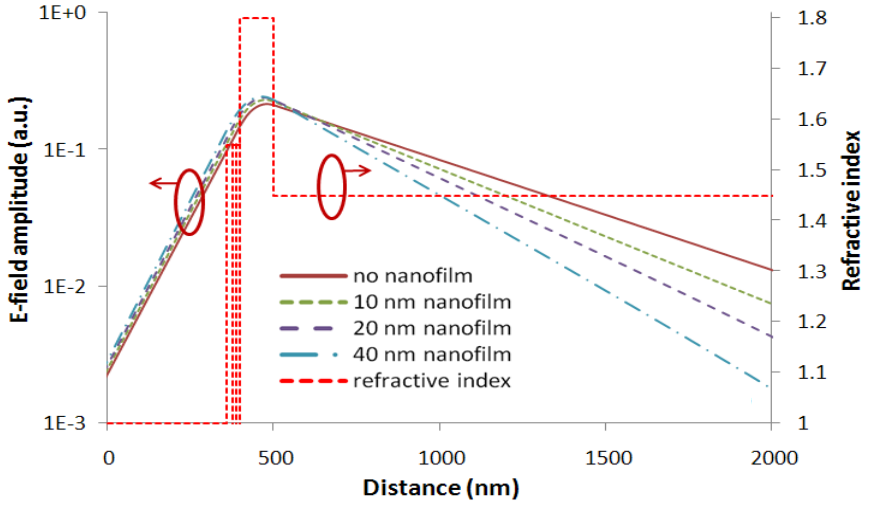

Fig.4.2. E-field decays exponentially as a function of depth into the lower waveguide cladding at different rates depending on nanofilm thickness (0 - 40 nm). The refractive index profile of the waveguide structure is shown (dotted lines) with air as the upper cladding, SiN_x, as the waveguide core, and SiO_2 as the lower cladding.

The simulated dependence of the decay constant on film thickness, d, appears in Fig. 4.3. Since the light intensity decays exponentially in the lower cladding, positioning a detector further from the waveguide core can increase its light intensity modulation ratio,

$$\frac{\Delta I}{I_0} \approx \frac{\exp(-2\gamma_{\text{film}} s) - \exp(-2\gamma_0 s)}{\exp(-2\gamma_0 s)} = \exp\left(-2(\gamma_{\text{film}} - \gamma_0)s\right) - 1 \qquad (4.1)$$

at a distance s below the waveguide core in response to the adsorption of a film on the surface that shifts the evanescent field decay constant from γ_0 to γ_{film}. The normalized photocurrent modulation of a thin linear detector will be approximately the same as the intensity modulation ratio. The evanescent decay constant varies along the waveguide according to the local film thickness in that region, so that a photodetector array can sense varying organic film thicknesses such as those that would result from different levels of specific binding along the waveguide if it were patterned with different probe molecules in different regions.

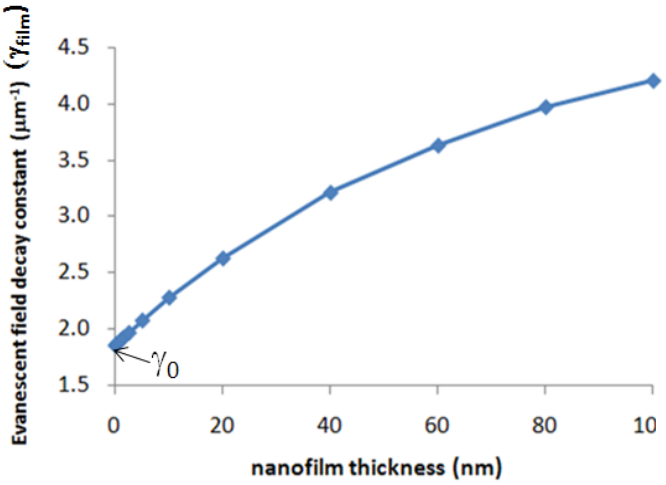

Fig. 4.3. Evanescent field decay constant dependence on nanofilm thickness.

As presented in Fig. 4.4, sensing with an integrated photodetector array s = 1.5 μm below the waveguide core results in a light intensity modulation ratio of approximately 16% upon a 1 nm change in thickness, which is about 10 times larger than the NSOM measured result (1.7%/nm) on the waveguide surface[7], and eliminates the need for large instrumentation. This conclusion will be confirmed by the experiment results showed in chapter 5&6. Thus, the integrated photodetector array configuration of the LEAC sensor, which we will discussed in Chap. 6, demonstrates greater sensitivity and enables system miniaturization which lends to the potential of an ambulatory or point-of-care device.

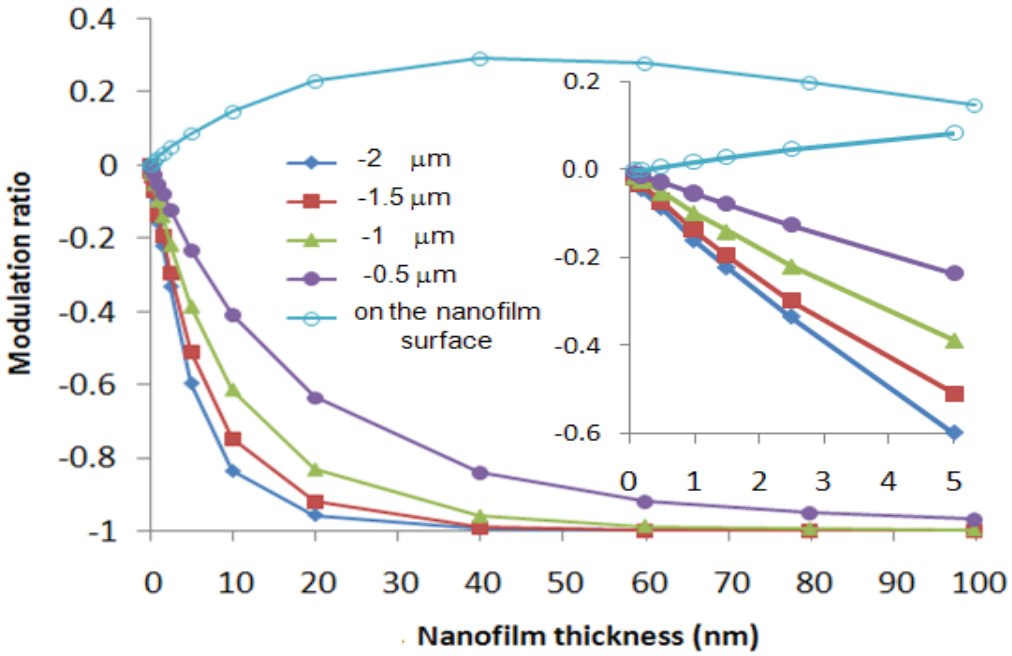

Fig 4.4. Simulated modulation ratio as a function of nanofilm thicknesses on the waveguide's top surface and for different vertical positions below the waveguide. Inset, zoom in view when nanofilm thickness is 0-5 nm.

BPM simulations were used to investigate the light intensity modulation ratios in response to the addition of surface films of varying thicknesses for different potential detector positions above and below the waveguide core. The modulation ratios due to the change in intensity from the case with no film to a film up to 100 nm thick are shown in Fig. 4.4. For a biofilm thickness of 2.5 nm, the light intensity modulation on the waveguide and film surface, approximating the case of NSOM measurements, is expected to be +5%, while the modulation ratio 1.5 μm under the waveguide, corresponding to a buried photodetector, is predicted to be 30%. These simulations predict that much larger modulation ratios can be obtained using buried detector arrays, and this trend is confirmed by the following experimental results. While the sensor's non-linear response to organic film thickness would slightly complicate calibration, which can easily

be implemented with future on-chip electronics, the approximately logarithmic behavior simultaneously offers a lower limit of detection and larger dynamic range.

According to Eq. 4.1, positioning the buried detector farther from the waveguide core structure, ie. increasing s, provides a larger modulation ratio and hence higher sensitivity. Analysis of the simulation data quantifies the relationship between the modulation ratio sensitivity and the detector's position and is presented in Fig. 4.5.

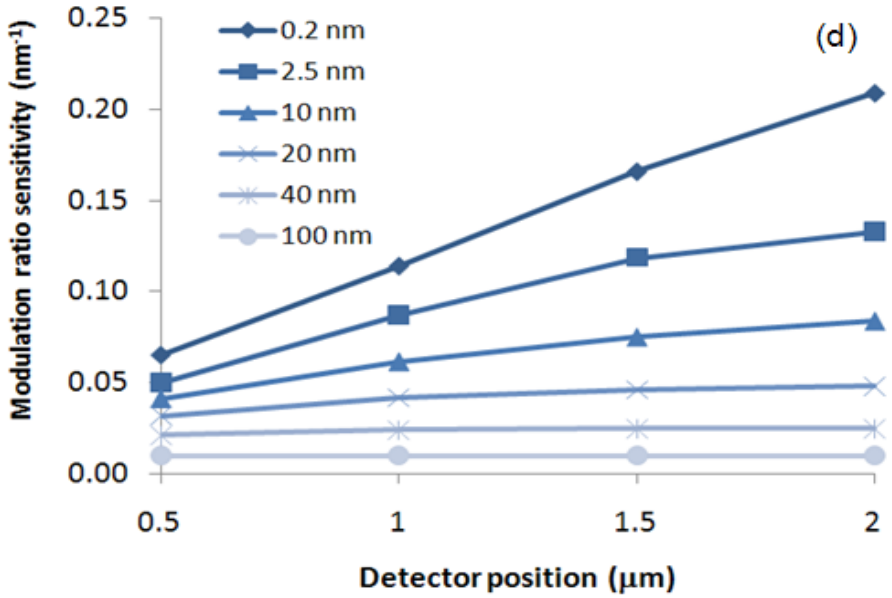

Fig. 4.5. Sensitivity analysis of the LEAC sensor based on simulation data for different detector positions and film thicknesses.

For moderately thick organic layers, the sensitivity changes little at different detector positions since the modulation ratios have saturated in these cases. However, when the organic films are thinner there is a strong dependence on detector depth. For example, for a subnanometer layer of d = 0.2 nm, the sensitivity increases from 6.4%/nm at 0.5 µm below the waveguide to 21%/nm at 2 µm, which indicates deeper detector positions offer a significantly increased sensitivity when

the LEAC sensor is used to detect nano-scale biomolecules or biofilms. While moving the detector further from the waveguide core decreases the absolute magnitude of photocurrents, this trend could be counteracted by increasing guided mode power.

According to the simulation results, an asymmetric waveguide design is adopted in the LEAC biosensor. Air serves as the upper cladding to make it is easy to pattern the biomaterial samples to the waveguide surface as well as to characterize the sample using NSOM before using buried detector array. All other parts of the waveguide, including the waveguide core, lower cladding and buried detector arrays, are fabricated using materials with proper refractive index and compatible with CMOS technology to lower cost. More details will be discussed in the following section.

Since the LEAC sensor relies on the detection of the local relative signal change due to the binding of target analytes and capture molecules, two parameters, modulation ratio and evanescent field power, are the key factors to determine the performance of the LEAC sensor. For a waveguide core patterned with nanofilm thickness, d_{nano}, the modulation ratio, M, is defined by $M(d_{nano}) = [P(d_{nano}) - P(0)]/P(0) = [I(d_{nano}) - I(0)]/I(0)$, where P and I are the evanescent field power and detected photocurrent across the buried detectors. Modulation ratio represents the percentage of current change caused by the nanofilm bound onto the surface of the waveguide. Sensitivity of LEAC sensor is defined as the modulation ratio normalized to the nanofilm thickness, representing the induced fractional current change per nanometer of film. Another parameter, the evanescent field power determines the measured photocurrent level measured across the buried detector. The evanescent field power affects the signal to noise ratio (SNR) and the metrology limit of the system. A metrology limit solely depends on the detection ability of

the optoelectronic hardware. Both modulation ratio and the evanescent field power are affected by the waveguide core thickness, d_{wg}, and the distance between the waveguide core to the buried detector, s.

A custom 1D Helmholtz solver and Beam Propagation Method (BPM) simulations were conducted to investigate the optimized waveguide core thicknesses and detector positions. The biomolecular nanofilms in all simulations are assumed to have the same index of refraction, n = 1.55. In the BPM simulation, a Gaussian light profile is launched into the center of waveguide core at one end, and all the data points of detected evanescent field power are obtained at 2 mm distance from the launching point along the waveguide. The nanofilm is located 1.6 mm away from the launching point with a length of 800 μm on top of the waveguide core.

The first set of simulations was performed using 1D Helmholtz solver to investigate the evanescent field power profile in response to nanofilms of varying thicknesses for different detector positions below the waveguide core, as shown in Fig. 4.6. The waveguide core thickness is 100nm, similar to the core thickness used on LEAC samples in previous experiments. The calculated modulation ratio from the case with 10nm, 20nm and 40nm biomolecular layers is shown in the same plot. All modulation ratios are presented in the form of their absolute values. The optical power at a distance s from the core can be written analytically as $P(d_{nano}) = P_{wg} \exp(-2\gamma(d_{nano}) \cdot s)$, where P_{wg} is the guided power in the waveguide. Thus, the optical power decreases exponentially with the increase of s, and decays faster with thicker nanofilm due to larger decay constant. On the other hand, positioning a detector further from the waveguide core increases the modulation ratio and sensitivity. The simulation plots of the evanescent field power and the modulation ratio amplitudes suggest a tradeoff between the

maximums of the two performance parameters as the detector position is moved farther from the waveguide core. As a result, a new parameter, the optimization parameter, is needed. Considering the shot noise, $i_{shot}^2 = 2qRP(0)\Delta f$, for a measurement bandwidth Δf using a buried detector with responsivity R that intercepts a power $P(0)$ in the absence of an adlayer, the signal to noise ratio of the system for small changes in nanofilm thickness causing a power $P(d_{bio})$ is, $SNR = [I(d_{nano}) - I(0)]/i_{shot} = A \times M(d_{nano}) \times \sqrt{P(0)}$, where $A = \sqrt{2qR\Delta f}$ is a constant. A calculated optimization parameter, $M(d_{nano})\sqrt{p(0)}$, with varying detector positions is shown in Fig. 4.7. Based on simulation results, the optimized detector positions for 10 nm, 20 nm, and 40 nm ad-layer thicknesses are respectively 560 nm, 500 nm, and 400 nm.

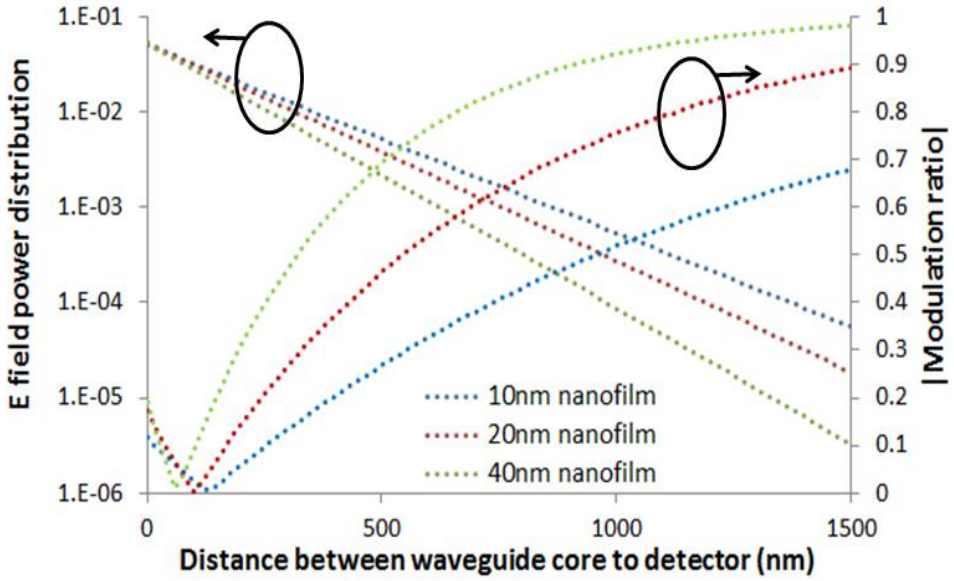

Fig. 4.6 The impact of both the evanescent field power and the absolute values of the modulation ratio on the various distances from the waveguide core bottom boundary to the detectors.

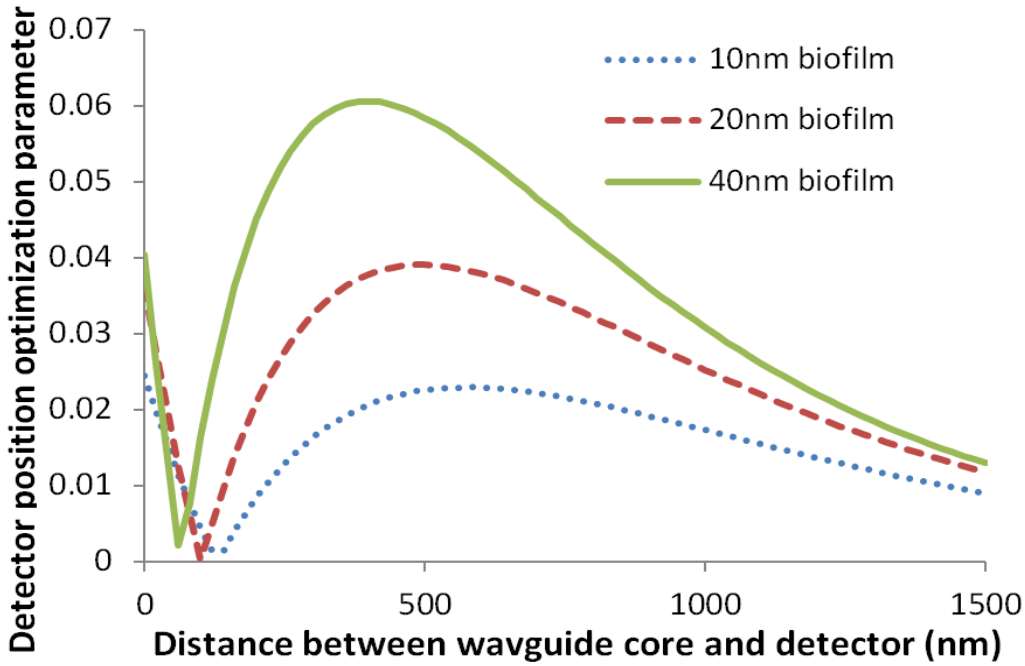

Fig. 4.7. BPM simulation results of the relationship between the detector position optimization parameter with the various detector positions, the peak values are the optimal values, where the maximum evanescent field power and the maximum absolute value of modulation ratio are achieved at the same time.

The impact of different waveguide core thicknesses on the system performance was studied through BPM simulations. The launch point used in this simulation was a 4 μm diameter Gaussian beam, similar to that emerging from a visible single mode fiber. Normalized power monitored at different depths below the core with different core thicknesses is plotted in Fig. 4.8. As the waveguide core thickness increases, the total coupled optical power of the guided mode in the waveguide core increases; however, at the same time, the evanescent distribution portion of the total optical power decreases due to the better confinement of the waveguide. Core thicknesses for maximal evanescent field power were found to be 90 nm and 63 nm for air and

water as the upper cladding, respectively. The waveguide core thicknesses for maximal power decreased slightly when the detector to waveguide core distance increased. The evanescent field power diminished when the waveguide core thicknesses were below the cut-off thicknesses, $d_{cutoff} = [\lambda \times \arctan(\sqrt{n_{SiN_x}^2 - n_{SiO_2}^2} / \sqrt{n_{SiO_2}^2 - n_{air}^2}]/(2\pi\sqrt{n_{SiN_x}^2 - n_{SiO_2}^2})$, which were 76 nm and 48 nm, respectively, for air and water as the upper cladding.

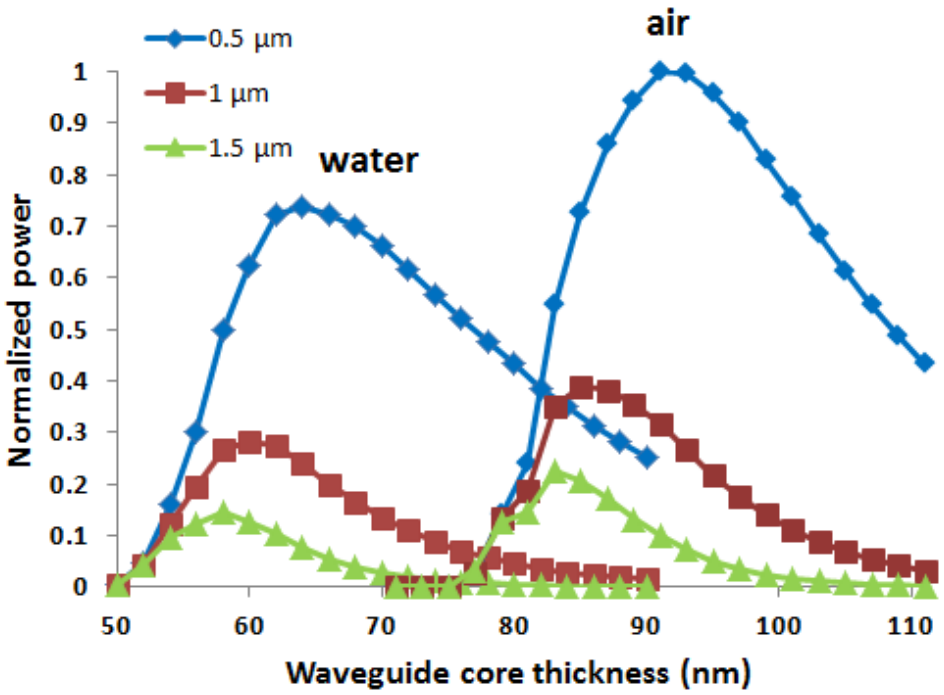

Fig. 4.8. (a) Evanescent field power (normalized) at different detection positions (0.5, 1 and 1.5 µm) from waveguide core with different waveguide thicknesses when the upper cladding is air and water.

The optimization parameters, $M(d_{nano})\sqrt{p(0)}$, are calculated and shown in Fig. 4.9 to optimize the waveguide core thickness. For the 10nm nanofilm, the optimal waveguide core thickness is 66 nm when the upper cladding is water and 93 nm when the upper cladding is air. As predicted from the first set of simulation results, when the waveguide core thickness is 100nm, the optimal

detector position is around 500 nm. The optimization parameter for nanofilm of 1nm, whose thickness is similar to most patterned bimolecular layers, is plotted in Fig. 4.9(b). The optimal waveguide core thickness is 58 nm when the upper cladding is water and 85 nm when the upper cladding is air. The optimal detector position is at 1.5 μm below the waveguide core. Compared with the 0.5 μm optimal detector distance for 10 nm nanofilm, the increase is because the smaller decaying constant leads to smaller evanescent power change along *s* in the lower cladding. On the other hand, thinner nanofilm results in larger modulation ratio sensitivity due to the stronger interaction with the exponential decaying evanescent field power in the upper cladding. Thus, compared with 10 nm nanofilm, modulation ratio, rather than evanescent field power, plays a dominating role in the optimization parameter for 1 nm nanofilm.

Considering the waveguide thickness of 100 nm and detector position of 1.5 μm employed in previous experiments are far from optimal values, the detection performance of the LEAC sensor can be significantly improved with the simulated optimal structure. The average standard deviation (SD) of the photocurrent modulation measurements is ~0.6% corresponding to ~0.04 nm in ad-layer thickness. The average sensitivity of the LEAC sensor with a core thickness of 100 nm used in this experiment is 16%/nm as determined from previous simulations. Thus the metrology limit of the LEAC sensor for changes in average layer thickness and based on optoelectronic system noise in these experiments is ~14 pm. By employing optimized parameters, LEAC performance can be improved largely. When the upper cladding is air the estimation metrology limit is 3.9 pm. For real-time measurements performed using an integrated microfluidic channel and water upper cladding, the estimated metrology limit is 5.4 pm.

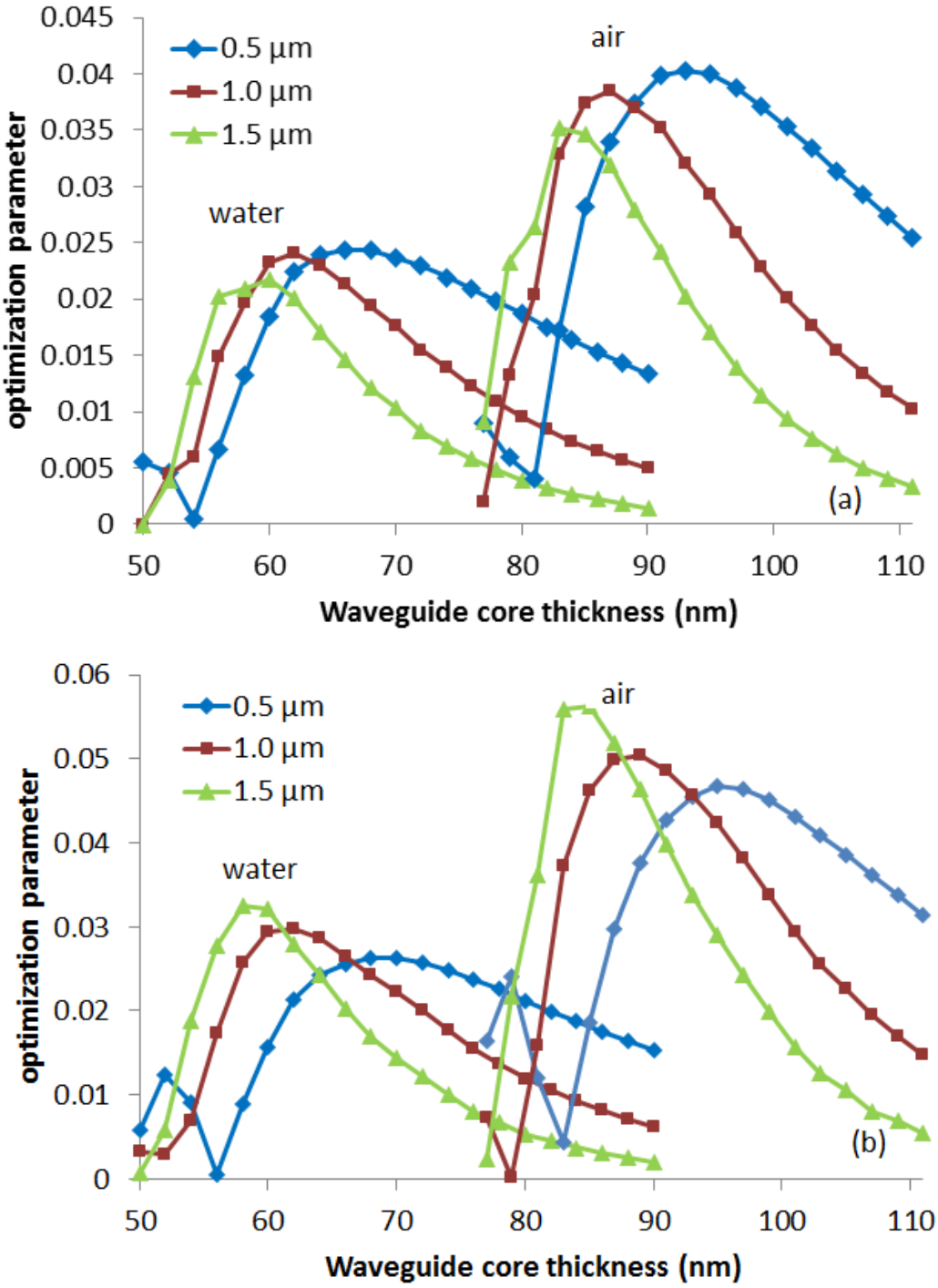

Fig. 4.9. BPM simulation results of the relationship between the waveguide optimization parameter with the various waveguide core thicknesses, the peak values are the optimal values, at were the maximum evanescent field power and the maximum absolute value of modulation ratio are achieved at the same time.

4.3 Sample fabrication

4.3.1 Review of the sample without buried detectors

The work reviewed below is mainly done by Matthew Stephens & Guangwei Yuan.

To fabricate this device (Fig. 4.10), an approximately 100nm thick silicon nitride film is deposited by reactive ion sputtering on a thermally oxidized silicon wafer. The film was deposited using a Nordiko 7000 with a silicon target and NH_3 as the nitrogen source. The substrates used to deposit the silicon nitride are thermally oxidized silicon wafers with 2 μm of oxide (Noel Technologies, Campbell, CA).

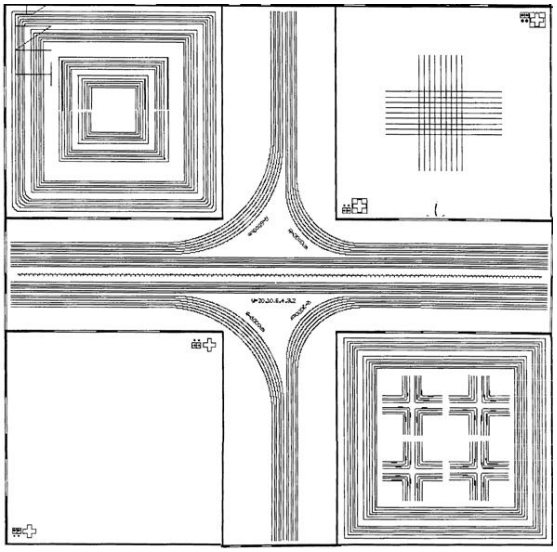

Fig. 4.10 4 × 4 inches Mask design for fabrication of 2 to 30 mm wide waveguides. Reproduced from [8].

To fabricate waveguide on the sample, approximately 1 in × 1 in chips were scribed from the wafer and prepared for processing by rinsing in acetone, methanol, and deionized water. After a 120℃ dehydration bake, Microposit S1818 positive photoresist was spun on a chip at 5000 to

6000 rpm to obtain a 1.8 μm thick layer. Following a 90 ℃ prebake, the photoresist was exposed using a Karl Suss contact aligner, and the sample was developed and inspected. As shown in Fig 4.11, ridge waveguides were etched in a Technics MicroRIE plasma etcher in a two step process. An initial etch using O_2 at 50W was used to descum the sample then the 15 nm waveguide ridges were etched at 50 W using a 4:1 CF_4:O_2 mixture[8][9]. Waveguides and the light coupling to these waveguides are shown in Fig. 4.12. The measurement data on these waveguide samples will be discussed in Chapter 5.

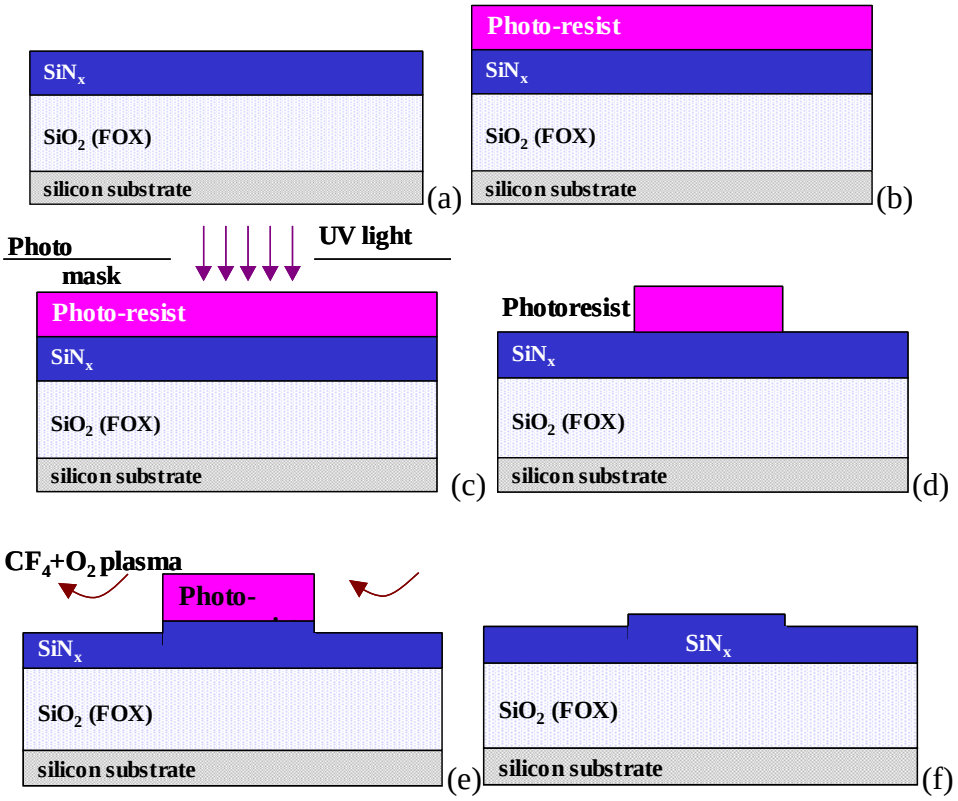

Fig. 4.11. Waveguide fabrication flow of the LEAC sensor without buried detector array (a)SiNx on SiO2/Si wafer (b) Spinning photoresist (c)Masking (d)Developing (e)Plasma etch (f) Cleaning. Reproduced from [8].

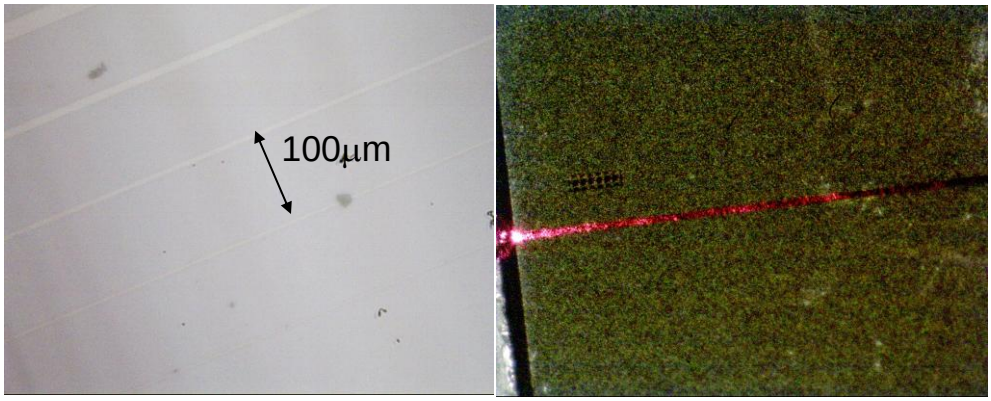

Fig 4.12. Microscope picture of the waveguide and the Light coupling into the waveguide. Reproduced from [9].

4.3.2 Avago sample fabrication

After the first try of the LEAC sensor with buried detector array in CSU's cleanroom[9], the second design that was implemented was the Avago detector. This detector had the general structure and dimensions shown in Fig. 4.13. The chip is designed by Guangwei Yuan and fabricated in Avago Technology Inc.

The MSM photodiode and waveguide structures, shown in cross-section in Fig. 4.14, are obtained by following a sequence of steps similar to those employed in conventional CMOS gate, dielectric, contact, and first layer metal processes. The first steps are the deposition of 250 nm thick polysilicon on 300 nm of thermal field oxide (FOX) on a silicon substrate, masking, and etching to form isolated polysilicon mesas. The polysilicon differs from that used for gate and resistor layers only in the fact that it is not doped with a subsequent implant process. A 1500 nm phosphosilicate glass (PSG) and tetraethyl orthosilicate (TEOS) silicon dioxide dual film is deposited over the polysilicon to serve as intermetal dielectric layers as well as the waveguide's

lower cladding. PSG and TEOS are silicon dioxide with different formations and have the same refractive index 1.45 here. A 100 nm thick SiN_x layer (n=1.8) was used to serve as the waveguide core. The 2.3 μm wide waveguide core structure is defined by two 1μm wide trench structures etched in the SiNx layer. The buried detector array was connected to probe pads in metal-2 on the wafer surface by the metal-1 layer and two levels of vias. The photodetector array elements are 95 μm long with 5 μm separations.

The Avago chip was the first generation of the LEAC sensor with buried detector array; many useful data has been collected by using it. However, there were many problems with it. First, there were three waveguide widths in the Avago chip design, 0.8μm, 1.6μm and 2.3μm, and it was proved that only the widest waveguide could be coupled with enough light power into to provide a long enough region for the detection. Three groups of the buried detector arrays were included in the design, 10μm, 50μm and 100μm. Detection region was limited by the number of the metal pads which connected the detectors out for probing, and the room on the chip could only contain 25 metal pads. Hence, smaller buried detectors led to smaller detection region. For example, the detection region for 10um long detector is just 250um. Considering the mode-beating induced oscillation and the size of adlayer, the detection region should be longer than 1000um, so only the 100μm detector array could be used in the experiment. Overall, on the whole avago chip, there was only one waveguide (2.3μm) /buried detector (100μm) combination could be used in the experiment. Second, to reach a more compact layout in the avago chip, the metal pads were designed too near the waveguide. This design made it impossible to measure the signal while the waveguide was covered by the microfluidic channel. Third, the scattering light from the polished edge will be collected by the buried detector, which is one of the major noises

in the measurement. Forth, the waveguides on the Avago chip have very rough sidewalls, which increased the sidewall scattering and hence increased the signal noise level.

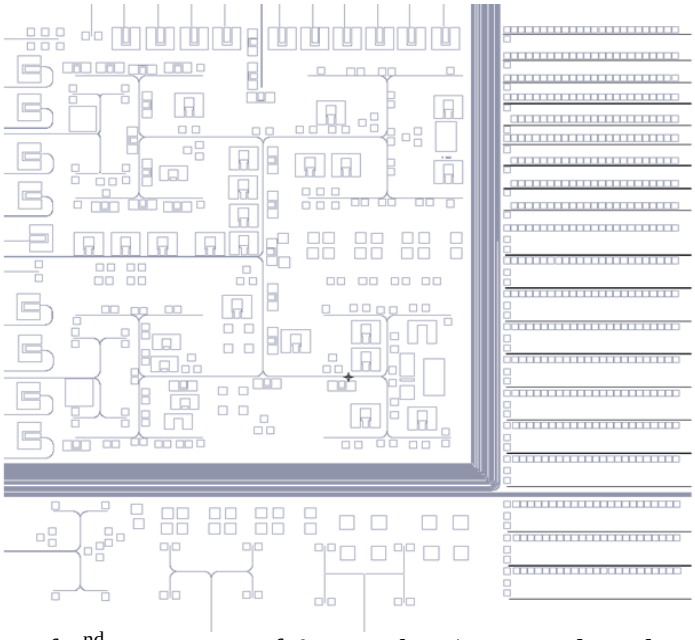

Fig.4.13. Mask design of 2nd generation of Avago chip (waveguide and pads part) Designed by Guangwei Yuan using LASI.

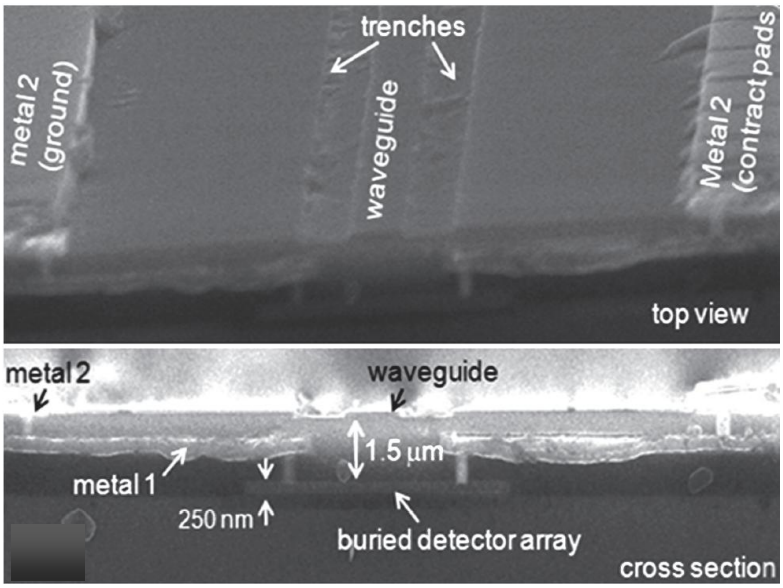

Fig.4.14. SEM picture of Avago chip (top view and cross section) .

4.3.3 Fabrication of the 3rd generation of the LEAC sensor

During the characterization of the Avago chip, a lot of problems have been revealed, such as the waveguide width and detector length design, the non-optimized position of detector pads for real-time monitoring, the photocurrent generated by the scattering light from the polishing edge.

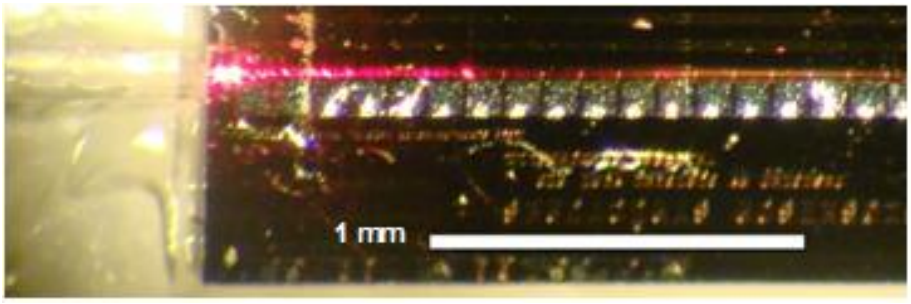

Fig. 4.15. Scattering from the polished edge.

Hence, a new LEAC sensor chip was designed to allow real-time monitoring and the compatibility with microfluidic channel integration. LASI was used to design the new mask. A waveguide bend was used to minimize the effect of the scattering light from the polishing edge during the fiber light coupling. Metal pads were put far from waveguides for three reasons: 1) Enable the detection while the waveguide was covered by microfluidic channels. 2) Reduce the possibility to scratch the waveguide using micro probes. 3) Avoid the possible PDMS channel leaking problem due to the bad adhesion between PDMS and Al. Limited by the cost and equipment, chemical mechanical polishing (CMP) won't be included in the new LEAC sensor fabrication flow, so different strategies were adopted to make sure the gaps between polysilicon detectors under waveguides won't cause too much light scattering. These strategies included 1)

besides traditional discrete buried detectors, continuous buried detectors, which had no gaps between each detecting spot, were also included in the mask. 2) Tapered polysilicon buried detector was introduced to decrease the angle of the step in the gap. 3) Thinner detectors were tested to find the best trade-off point between light scattering loss and the sensitivity of the detector. Positions for grating coupling have been reserved on the new mask design.

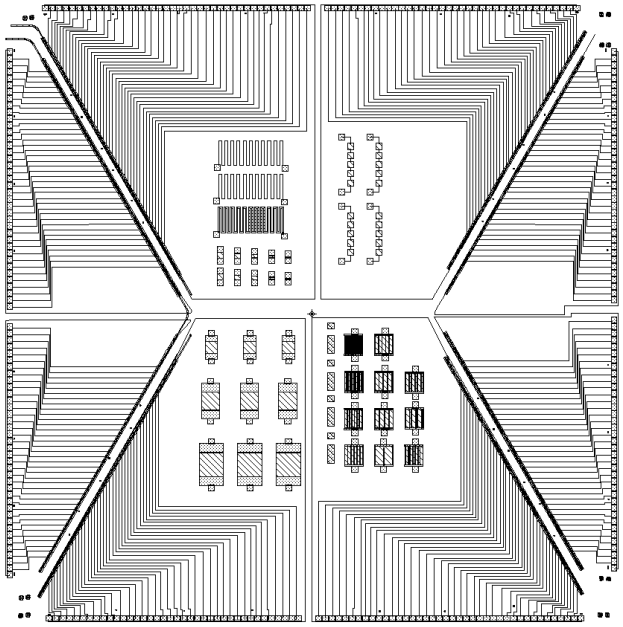

Fig. 4.16. 2nd generation LEAC mask design ver.1.

In the mask design ver.1 shown in Fig. 4.16, a waveguide bend is used to avoid the scattering from the polishing edge. 100μm long buried detector was used to provide a longer detection region. Metal pads are designed far from the waveguide to allow the probing while the waveguide is coved by PDMS microfluidic channels.

Problems were found during the fabrication and characterization of the LEAC samples using the 2nd generation LEAC mask ver.1. 2nd version of the LEAC mask was design based on the following modifications:

1) The width of the metal wire in the 1st version was 10um, and problems such as broken wires due to the under developing using existing negative photoresist (AZ2070) were found in the fabrication. In the 2nd version of the mask design, the width of the metal wire was increased from 10 um to 30um to address this problem.

2) To avoid the MSM detector collecting the light from environment, the effective absorption area of the detector was designed as small as possible. In the 1st version of the mask design, the gap between the two metal connectors on the MSM detector was design to be 10um, which was the same as the Avago design. However, it was found that the overdevelopment of the photoresist before the lift-off process will decrease the gap from 10um to 5-6um. This made the alignment of the waveguide in the middle of the metal connectors extremely hard and time-consuming. In the 2nd version of the mask design, the gap was increased to 20um to address this problem.

3) Due to the structure of the detector under the waveguide, strong scattering was observed when the guided light propagated into the detection region. In the characterization, if the guided light in the waveguide was weak in the end fire coupling, it was hard to tell the reason behind that. It could be the scattering due to the high detector step or the defective waveguide structure due to some mistakes made during fabrication. In the 2nd version of the mask design, a diagnostic waveguide without any detector structures was added near the positions of the "real" waveguides.

4) In the new design, the length of metal pads was increased from 100um to 300um to make it was easier to probe with probe card

5) Different diagnostic structures, including serpentine resistors, and test MSM detectors, were added to the design. Grating coupling structures were added before waveguides. An arrow structure was added to help distinguish the correct directions during the mask aligning and polishing with bared eyes.

Shown below in Figure 4.17 is the 2nd version mask design and the mask layout. The four different quadrants show the four main mask layers: Metal, Waveguide, Metal Via, and Buried Detectors. Within each quadrant are variations within each mask layer. These variations have different dimensions and features that will be tested on the LEAC chip.

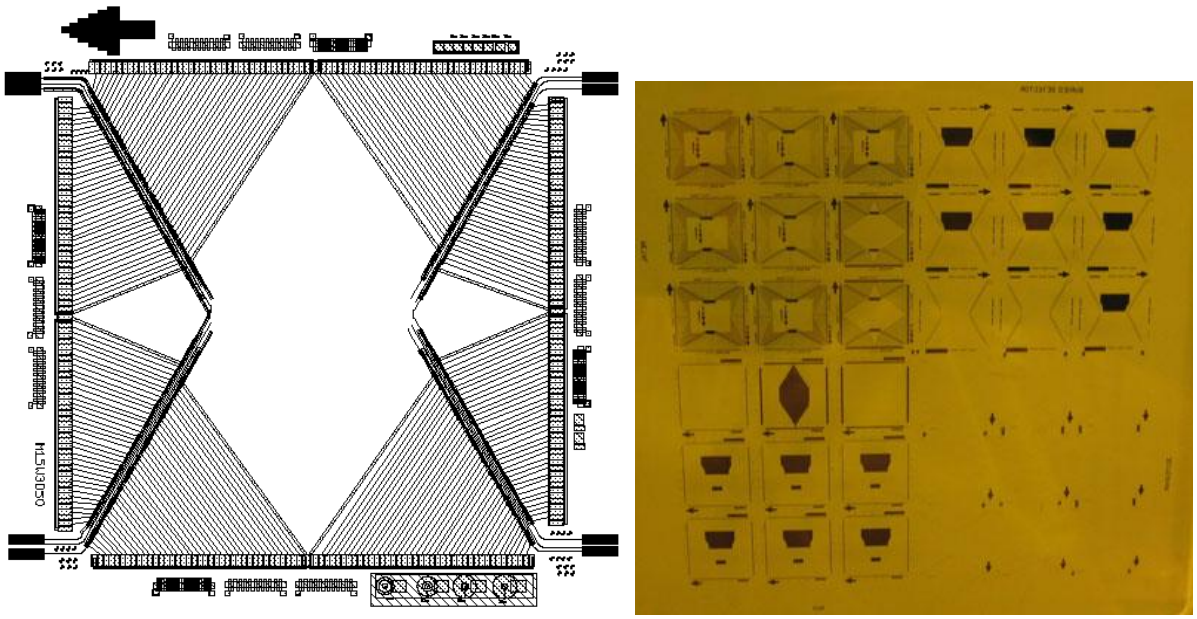

Fig. 4.17. 2nd generation LEAC mask design ver. 2.

Fabrication of the 3rd generation LEAC sensor is done in the CSU. A brief introduction to the fabrication processes and technology used in the manufacture of the LEAC chip will be introduced. A short walkthrough of the LEAC chip fabrication in particular will then be discussed. The full fabrication flow for our chip may be found in Appendix A: LEAC Chip Fabrication Flow.

The LEAC chip is fabricated using many common processes and techniques used in the semiconductor manufacturing industry. Among these are photolithography, etching, and deposition. Using individual layers of the mask shown in Fig. 4.17 one at a time, all of the features can slowly be developed from a featureless silicon wafer.

LEAC biosensors were fabricated in the CSU cleanroom. The LEAC chip is fabricated using multiple steps of photolithography, etching and thin film deposition. The first several batch of LEAC sensor is fabricated using a polysilicon wafer. The fabrication flow described here will correspond to the cross sectional view seen in Fig. 4.17.

Fabrication begins with a silicon wafer with 100nm silicon dioxide (SiO_2) and 255nm polysilicon layer on top of it. The SiO_2 layer is for insulating the polysilicon layer from the silicon substrate. The first step in fabrication is etching the polysilicon layer into the buried detector structures. This is done by using the buried detector mask to place a mask of photoresist on the top of the chip and etching it down. In this case the etching is performed by the micro-RIE machine, and thus is dry etched (CF_4+8%O_2). We also used a wet etch of KOH to remove the polysilicon as the dry etching is not very selective and at times has removed our insulating

silicon dioxide layer. In this case, however, a mask of SiN_x must be used as the photoresist cannot stand up to the KOH.

Next the metal pads and wires are laid down. This is done by first applying a layer of negative photoresist and performing what is known as lift off. After the photoresist is applied and has been developed using the metal mask layer, aluminum is deposited using the e-beam evaporation machine. After, the whole sample is submerged in acetone with dissolves the photoresist and thus "lifting off" the metal lying on top of it. This leaves the aluminum only in the positions that we wish.

After this, a silicon dioxide lower cladding was deposited to separate the buried detectors from the waveguide. This is done by using the PECVD machine, which will deposit silicon dioxide all over the top surface of the chip. We normally deposit at least 1.5um of SiO_2 on the surface. Immediately following this lower cladding deposition, a layer of SiN_x is then applied directly on top of the SiO_2, again using the PECVD machine. This layer of SiN_x then etched into the waveguide features by using positive photoresist (S1818) and the waveguide mask.

All that is left after these steps is to gain access to the metal pads that are buried beneath the SiO_2 layer. To achieve this we use the "via" mask to cover the whole chip with photoresist except for the locations with the metal pads. The SiO_2 layer is so thick that dry etching would take way too long to perform so we use wet etching once again. Hydrogen fluoride (HF) with different concentrations was tested to remove the 1.5 μm SiO2 layer on the 300 nm Al pads. It was proved that the HF selective etching rate for SiO2 and Al is not large enough for this

application, so a commercial etchant, Silox Vapox III (Transene Co.) was adopted in the via etching process.

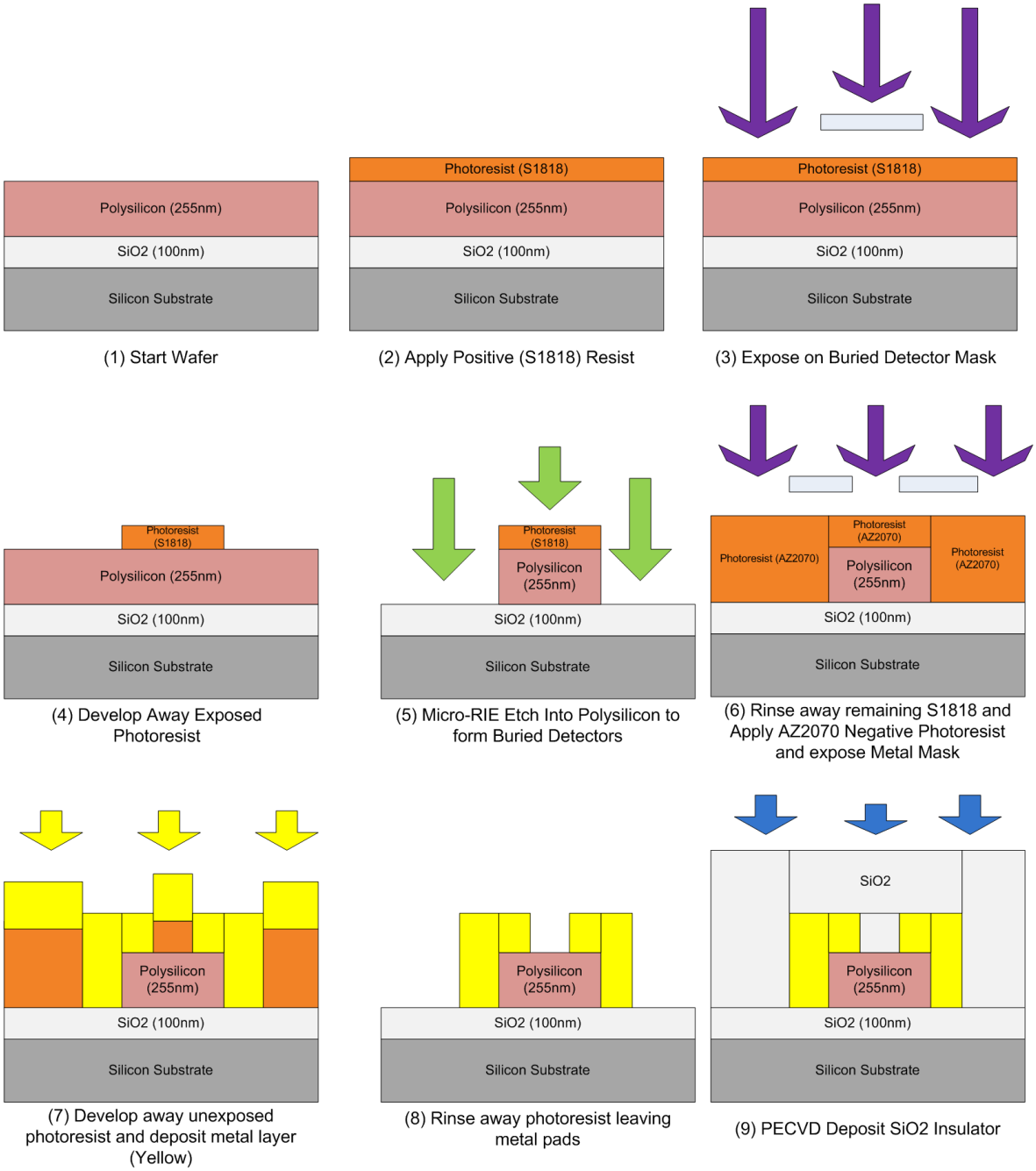

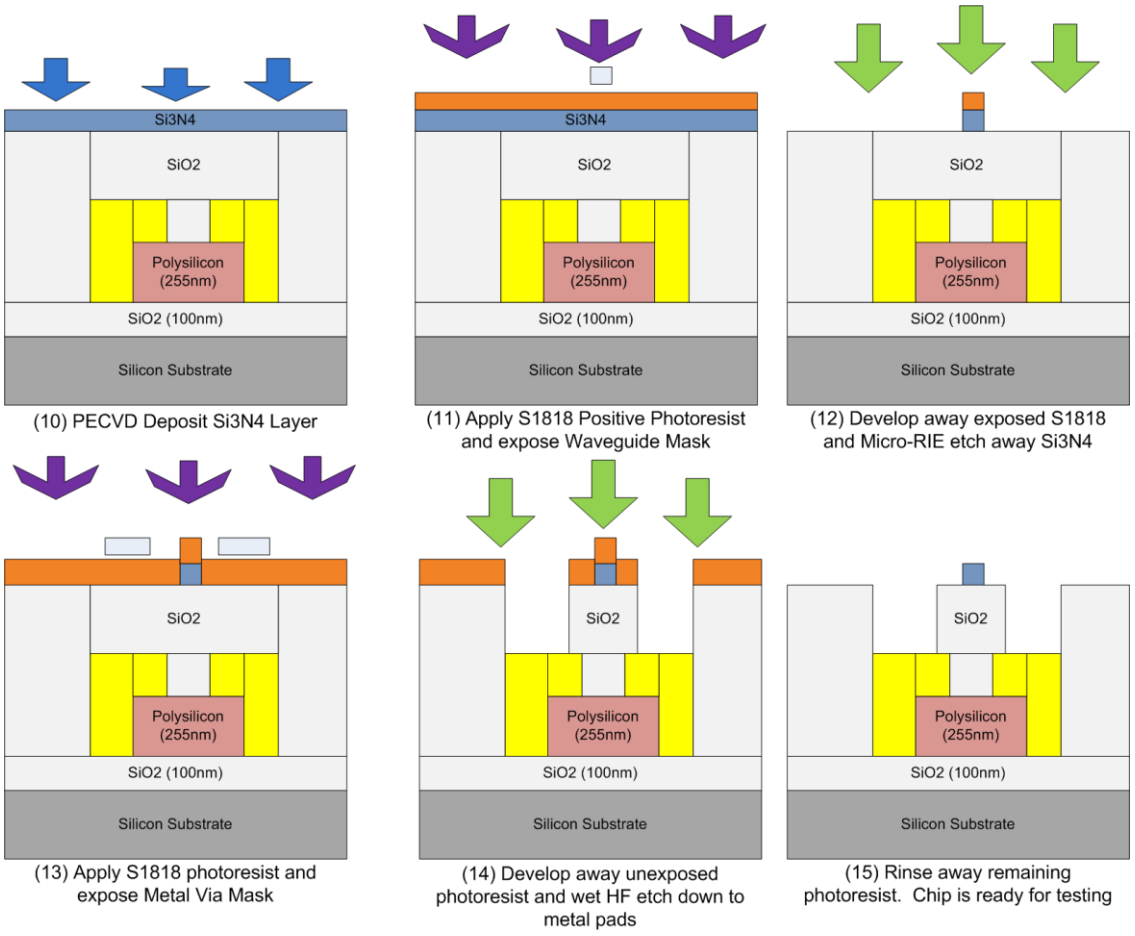

Fig. 4.18 LEAC sensor fabrication flow using polysilicon wafers.

In recent LEAC sensor fabrications, SOI wafer was used to replace the polysilicon wafer because it was hard to find a vendor to provide undoped or high resistance polysilicon wafer, or any facilities that could be used to deposit polysilicon for a reasonable price. The SOI wafer is not suitable to fabricate the LEAC sensor structure, because except some high cost ultra-uniform SOI wafers, the thickness variation of device layer for most SOI wafer was ~200-500nm. If we

used the traditional Si island MSM detector structure, as shown in Fig. 4.18, the waveguide thickness should be larger than the step formed by the buried detector structure to allow the guided light propagate through. The waveguide thickness in this case was much larger than the cutoff thickness of 100nm required by the device. On the other hand, even if we could fabricate a thin enough Si layer to make the waveguide work, the limited thickness of the detector would lead to a small photocurrent.

To address these problems, we introduced a new structure in Fig. 4.19 to replace the Si island structure in the SOI LEAC sample fabrication. This new structure gave us the freedom to separate the thickness of the buried detector and the step height. The fabrication flow in Appendix A is based on this structure.

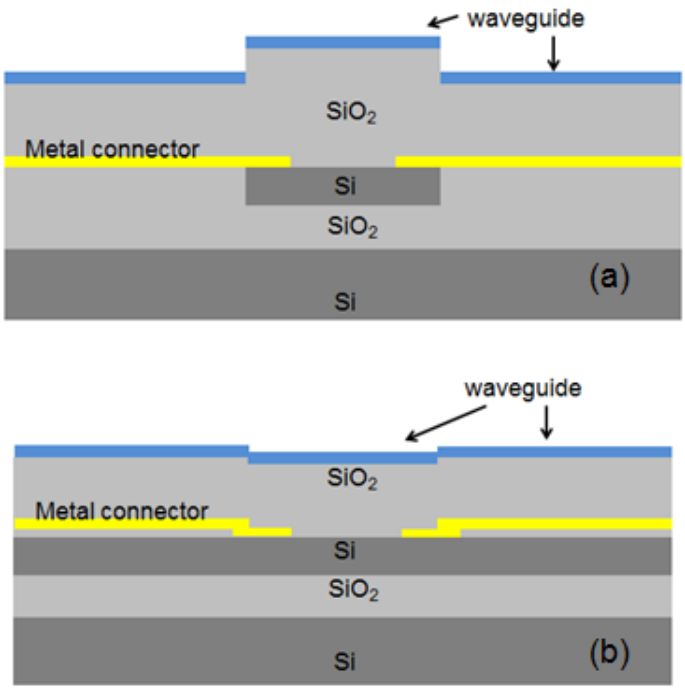

Fig. 4.19 (a) Si island structure MSM detector (b) Thin SiO_2 insulator MSM detector.

4.4 Sample polishing and end-fire light coupling

After the fabrication, samples were scribed and cleaved perpendicular to the waveguides. Facets on this cleaved edge, as shown in Fig. 4.20(a), were usually too rough to couple light into the waveguide. Thus, they were polished using polishing papers a progression of 9 decreasing alumina grit sizes from 30 down to 0.05 μm. As shown in Fig. 4.20(b), polishing process made the facet of the sample smooth enough for the following end-fire light coupling.

In our studies, we use the end-fire method to couple light into the waveguide simply by aligning the end of the optical fiber against the waveguide facet as illustrated in Fig. 4.21. A 3-axis piezoelectric translation stage from Thorlabs (resolution of 10 nm and range of 15 μm in all 3 axis) was used to align the fiber to the edge of the chip. A laser diode to fiber coupler was used to deliver light from a 654 nm laser diode into the 4 μm core signal mode fiber. Fiber was stripped from the jacket and glued to a glass substrate to make the core of the fiber in the same height with the waveguide core. The waveguide under test was mounted on a height adaptor and aligned using the translation stage. The typical beam diameter of visible single mode fibers used for the studies is approximately 4 μm.

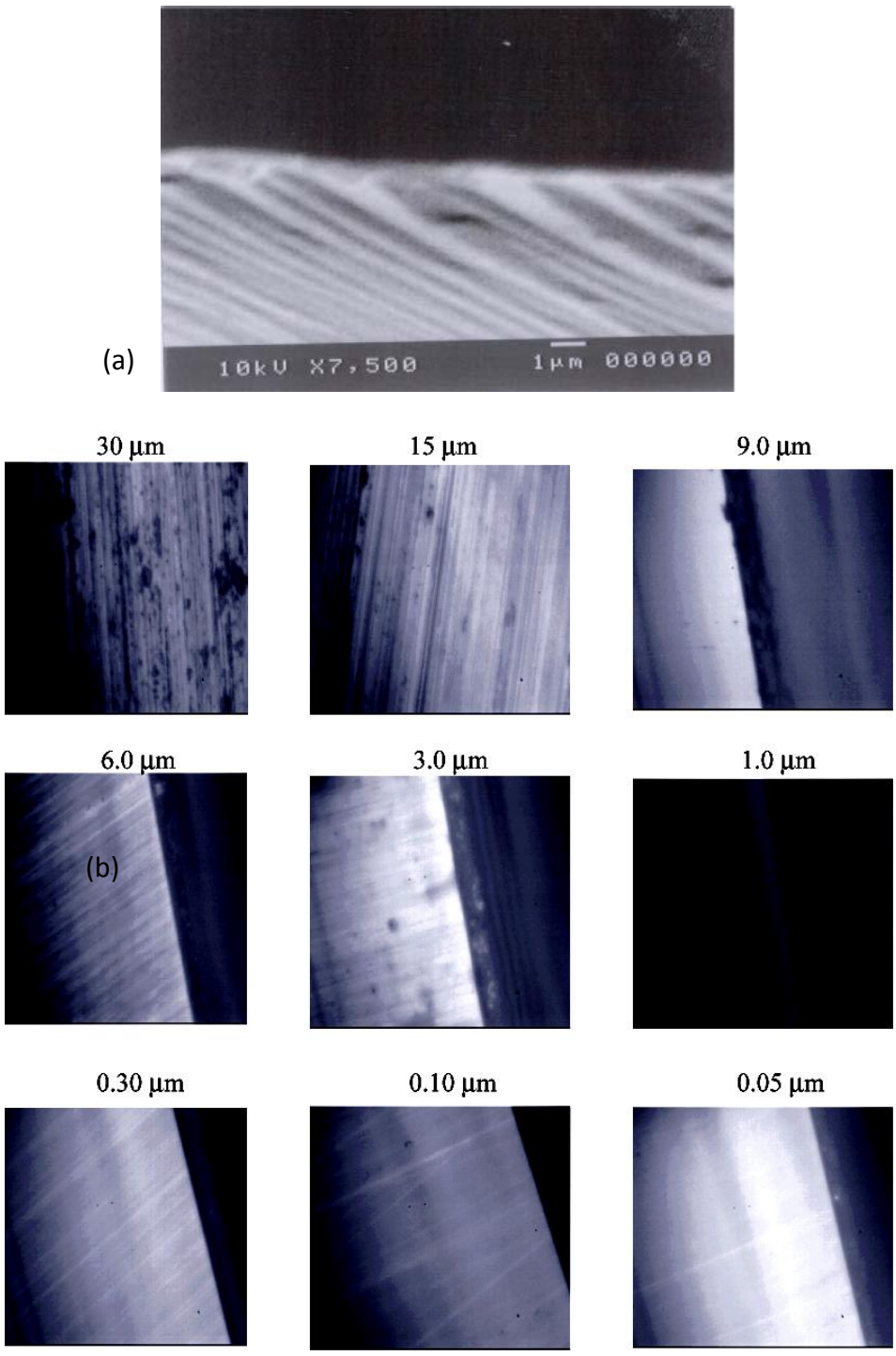

Fig. 4.20 (a)waveguide facet before polishing (b)facet polishing using polishing papers with different grit sizes. Reproduced from [8].

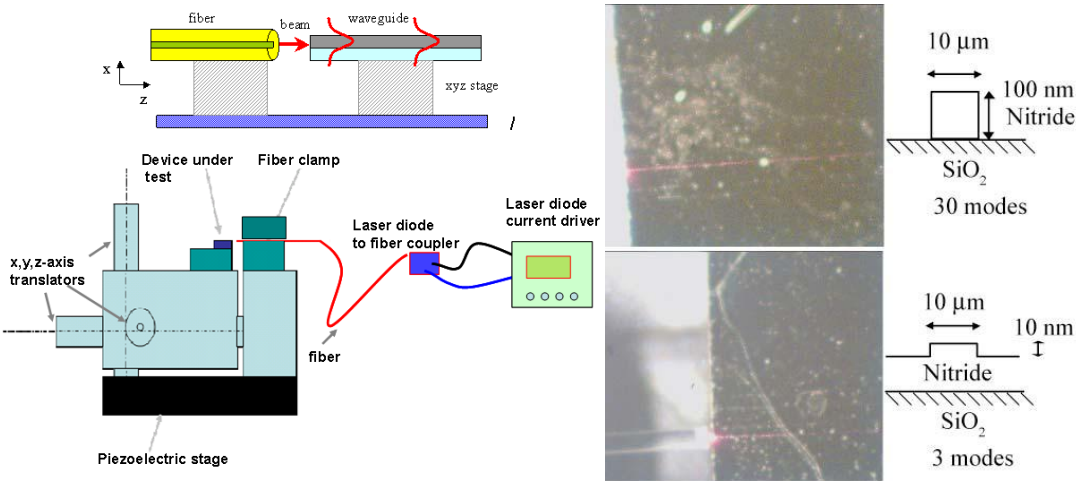

Fig. 4.21: End-fire coupling diagram [8] and coupled light into different waveguides.

4.5 NSOM setup & measurement

NSOM measurements reported in the following chapters employed an Alpha-SNOM system from WiTec. NSOM tip is a hollow aluminum pyramid integrated onto a Si cantilever, as shown in Fig. 4.22, which converts the evanescent field to a propagating wave by locally frustrated total internal reflection, as discussed in section 2.3.2. A piezo-stage controlled scanning system scans the tip over the sample surface in the contact mode, and a reference laser beam reflecting off the cantilever is directed to a quadrant detector by a beam splitter and is used to sense tip deflection in atomic force microscopy (AFM) mode, as shown in Fig. 4.23, which grants this system simultaneous optical and topographical profiling capability.

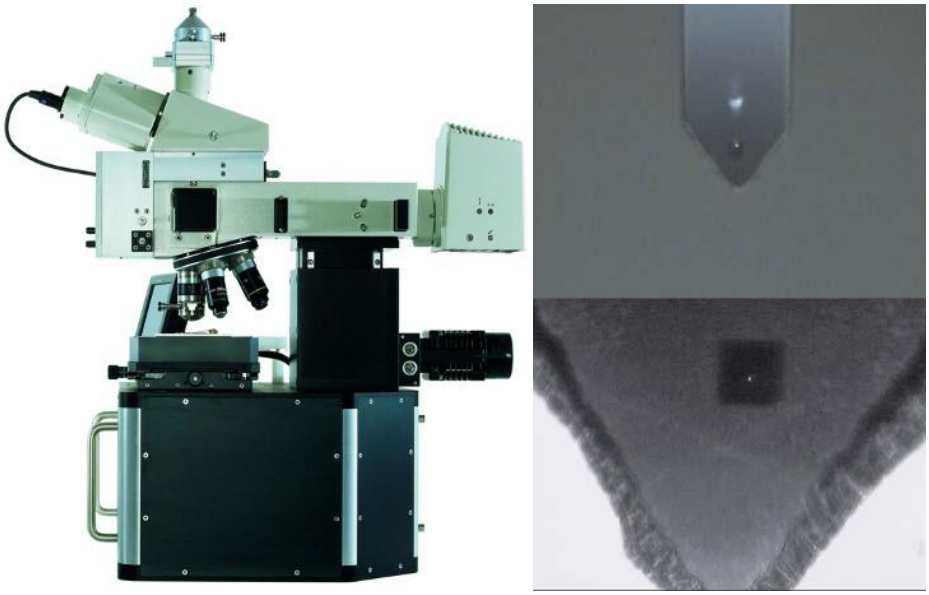

Fig. 4.22. α-SNOM (WiTec, Ulm, Germany) and Image of the NSOM cantilever tip. Reproduced from [8].

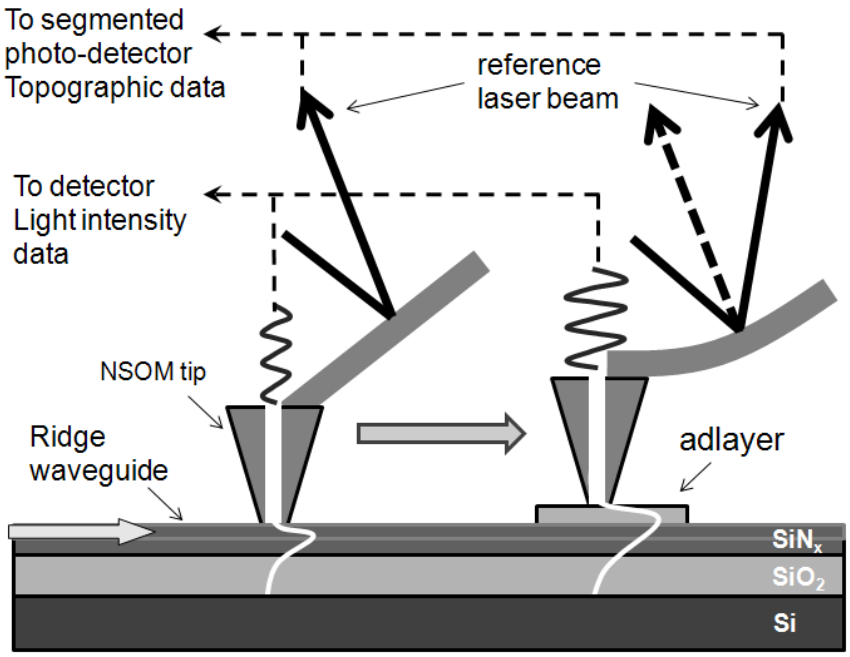

Fig.4.23. Schematic diagram (not to scale) of the NSOM system for imaging the optical distribution in a waveguide with an adlayer.

As the tip is moved toward the top surface of the waveguide studied here, an exponentially increasing optical field is observed in addition to a constant signal due to reference beam scattering, verifying that the evanescent field can be distinguished from scattered reference beam light. During in-plane optical profiling, the NSOM was operated in contact mode so that the field at the top surface of the waveguide was measured.

4.6 Measurement with buried photodetector arrays

For the samples with integrated buried detector arrays, it is possible for us to monitor the photocurrents from the chip, which are proportional to the light intensity penetrating into the detectors, to characterize the light response of the LEAC sensor to different patternings.

The simplest configuration is shown in Fig. 4.24. The chip facet is polished as described in Section 4.4 to allow the end-fire coupling of 654nm light from a single mode fiber into the waveguide on the chip. The measurement system uses a DC signal. A Keithley K2400 source meter was used to apply the voltage cross the buried detector and determine the current signal passing it. Two thin flexible microprobe needles are used to probe the metal pads on the chip to minimize disturbances that could be introduced into the light-coupled system, which may change the guided light power in the waveguide. Besides the probe-induced coupled-light decay problem, the dark current is another factor that may significantly affect the measurement results in this DC system.

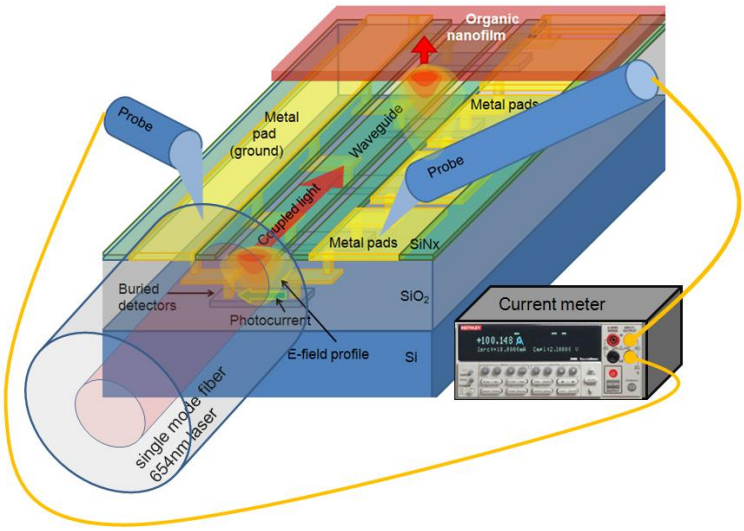

Fig. 4.24. DC measurement of LEAC biosensor with buried detector array using Keithley K2400.

To further decrease the noise level, an AC measurement system as shown in Fig. 4.25 was used in the HspX experiment[10]. Two notch filters (60Hz and 120Hz) were added before the demodulator in the lock-in amplifier, which lead to a signal decrease around there two frequencies, so the modulation frequency should be chosen far enough from these two frequencies. A measurement scanning the frequencies from 10Hz to 1 kHz showed DC output from lock-in amplifier decreased with frequency increased. Hence, a 16.8 Hz 3 V peak-to-peak AC signal with 2.6 V offset was generated by the HP8116A function generator and was used to modulate 654nm laser diode and as the reference signal for lock-in amplifier. The photocurrents generated from the DC-biased buried detectors were collected by the 5210 dual-phase lock-in amplifier. To cancel out the coupled light power decaying in the waveguide due to vibration of the fiber, a reference probe needle was applied to the last detector pad in the AC measurement to monitor the reference current. To make the process of testing the LEAC chip quicker we

implemented a probe card to enable probing multiple photodetectors of the LEAC chip simultaneously.

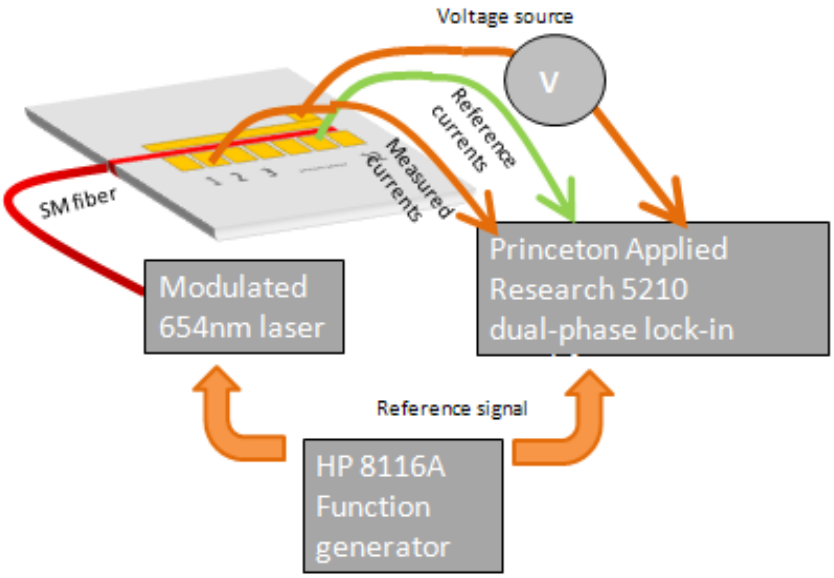

Fig. 4.25. Configuration of the AC measurement system.

References:

[1] Chung-Yen Chao, W. Fung, and L. Guo, "Polymer microring resonators for biochemical sensing applications," *Selected Topics in Quantum Electronics, IEEE Journal of*, vol. 12, 2006, pp. 134-142.

[2] K. De Vos, I. Bartolozzi, E. Schacht, P. Bienstman, and R. Baets, "Silicon-on-Insulator microring resonator for sensitive and label-free biosensing," *Optics Express*, vol. 15, Jun. 2007, pp. 7610-7615.

[3] M.L. Gorodetsky, A.A. Savchenkov, and V.S. Ilchenko, "Ultimate Q of optical microsphere resonators," *Optics Letters*, vol. 21, Apr. 1996, pp. 453-455.

[4] R.D. Harris and J.S. Wilkinson, "Waveguide surface plasmon resonance sensors," *Sensors and Actuators B: Chemical*, vol. 29, Oct. 1995, pp. 261-267.

[5] R. Slav ķ, J. Homola, and J. Ctyroký, "Single-mode optical fiber surface plasmon resonance sensor," *Sensors and Actuators B: Chemical*, vol. 54, Jan. 1999, pp. 74-79.

[6] J.D. Suter, I.M. White, H. Zhu, H. Shi, C.W. Caldwell, and X. Fan, "Label-free quantitative DNA detection using the liquid core optical ring resonator," *Biosensors & Bioelectronics*, vol. 23, Feb. 2008, pp. 1003-1009.

[7] R. Yan, G. Yuan, M.D. Stephens, X. He, C.S. Henry, D.S. Dandy, and K.L. Lear, "Evanescent field response to immunoassay layer thickness on planar waveguides," *Applied Physics Letters*, vol. 93, 2008, pp. 101110-3.

[8] Y. Guangwei, "Characterization of integrated optical waveguide devices," *Dissertation, Colorado State University, 2007*.

[9] S. Matthew, "Thin film integrated optical waveguides for biosensing using local evanescent field detection," *Dissertation, Colorado State University, 2009*.

[10] R. Yan, S.P. Mestas, G. Yuan, R. Safaisini, D.S. Dandy, and K.L. Lear, "Label-free silicon photonic biosensor system with integrated detector array," Lab on a Chip, vol. 9, 2009, pp. 2163-2168.

Chapter 5

LEAC BIOSENSOR MEASURED USING NSOM

In this chapter, experimental results for this project measured using NSOM will be reviewed. In the first part we will discuss some basic waveguide structures, and some previous work finished by Guangwei Yuan & Matt Stephens will be included as Section 5.1.1 and 5.2.1 to provide context for the rest of the work. In the second part, proof of concept experiments on different adlayers will be mentioned. Most of the experiment data were obtained using the near-field scanning optical microscope (NSOM) system from WiTec Inc. (α-SNOM system). The NSOM was operated in the contact mode so that the evanescent field optical intensity at the top surface of the waveguide was measured, and the topological height of waveguides was imaged simultaneously. Some of results discussed in this chapter has been published in journal papers and presented in conference presentations, as listed in the reference part.

5.1 Measurement on basic waveguide structures

In this section, some of the NSOM measurement on the single/multimode straight waveguides, which are the most basic optical component in most waveguide based biosensors, will be discussed. A study of y-type splitter structures will included in Section 5.1.2.

5.1.1 Previous work on single mode and multimode waveguide

Straight waveguides are used to carry optical power or signals from sources to receivers, and they are a fundamental element of many popular biosensing systems, such as waveguide-based SPR biosensors, ring resonator biosensor and MZI biosensors. Other novel biosensors include waveguides in the system to help shrink the system size and lower the cost[1][2][3]. Therefore, determining the modal behavior in straight waveguides was vital in order to understand complex waveguide devices. In this section, we are going to investigate different straight waveguides, including single mode and multimode waveguides, as well as waveguide bends, which are important for the future LEAC biosensor design.

The single mode waveguide is the simplest and one of the most important forms of all waveguide devices, and it is very useful for the LEAC biosensor since it has a uniform power distribution along the light propagation direction, which makes it is easier to detect adlayer-induced light power change along the waveguide.

In this experiment, the waveguide core consisted of an 88-nm-thick SiN_x film deposited onto a ~2 μm thick SiO_2 lower cladding supported on a Si substrate. No solid upper cladding was deposited above the SiN_x. This approach also provided the NSOM ready access to the evanescent field in the air above the core, which served as the upper cladding. Dry etching of 21 nm of the SiNx outside a ~2 μm-wide ridge defined the lateral extent of the core. Although 3D simulation could provide accurate result for this structure, considering the small step (ridge waveguide in LEAC biosensor has height of ~100nm) and relatively large geometric size of the waveguide structure, a simpler and faster effective index method was used to help to characterize this single mode waveguide. Effective index is the propagation constant of one guided mode in the waveguide divided by the wave vector of light in free space, which means this parameter defines the "refractive index" this guided mode has in this waveguide structure.

In our case, the method helped us to calculate the guided/leaky modes in a ridge waveguide by solving two 1D waveguide problems using the 1D modal solver codes. Original version could be found in Guangwei's dissertation and a revised version could be found in Appendix B. The solver solved the E-field and effective index in the vertical direction. The calculated effective index of the waveguide core in the lateral direction was n_{eff}=1.4529. Therefore, the vertical and horizontal V-parameters were 0.45 and 0.735, respectively.

NSOM was used to directly measure the evanescent field on the upper surface of the waveguide. The NSOM instrument used was a α-SNOM system from WiTec. NSOM experiments yielded light intensity and topography maps simultaneously, as shown in Fig. 5.1. The optical intensity pattern reveals a smooth, fundamental mode distribution without oscillations associated with mode beating.

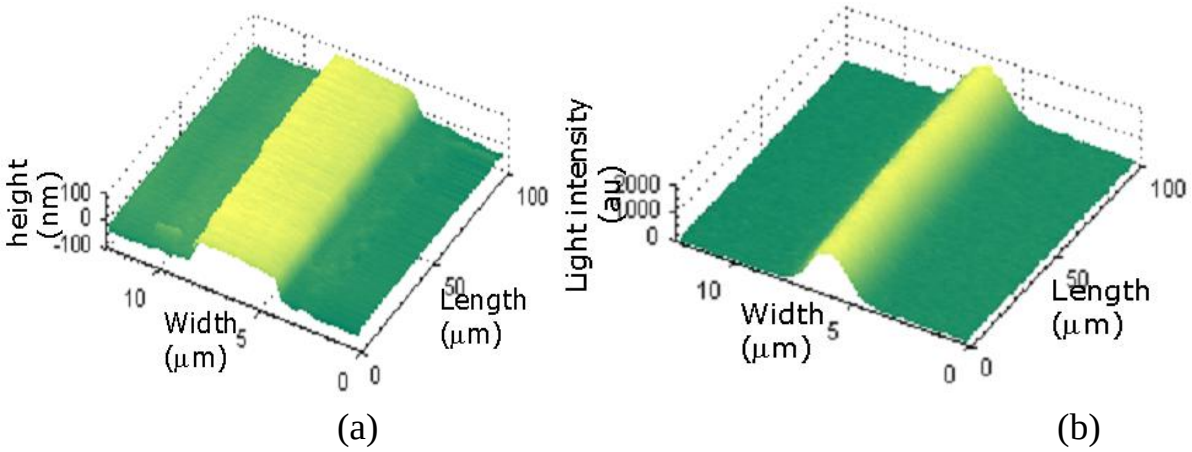

(a) (b)

Fig. 5.1. NSOM measurements of (a) surface topography and (b) optical intensity of a single mode straight waveguide.

5.1.2 Y-type splitter structure

Splitter structures are important elements of on-chip optical interconnect systems[4]. Some applications, such as H-tree optical clock distribution need balanced splitters to evenly distribute signals to many nodes while other applications such as reconfigurable signal routing could benefit from simple splitters. For the LEAC biosensor, optical splitter will grant the chip multi-detection ability with minimal number of the light source, as shown in Fig. 5.2.

The splitters are studied using near-field scanning optical microscope (NSOM) measurements as well as finite difference time domain (FDTD) simulations. Both symmetric and asymmetric Y-branching waveguides have been well studied by various authors [5][6].

A multimode waveguide, which is much narrower than the conventional multimode waveguides and hence only supports two eigenmodes, is adopted to fabricate a novel y-type

splitter, and it is proved that a wide range of the branching ratio can be achieved by adjusting the phase difference between modes.

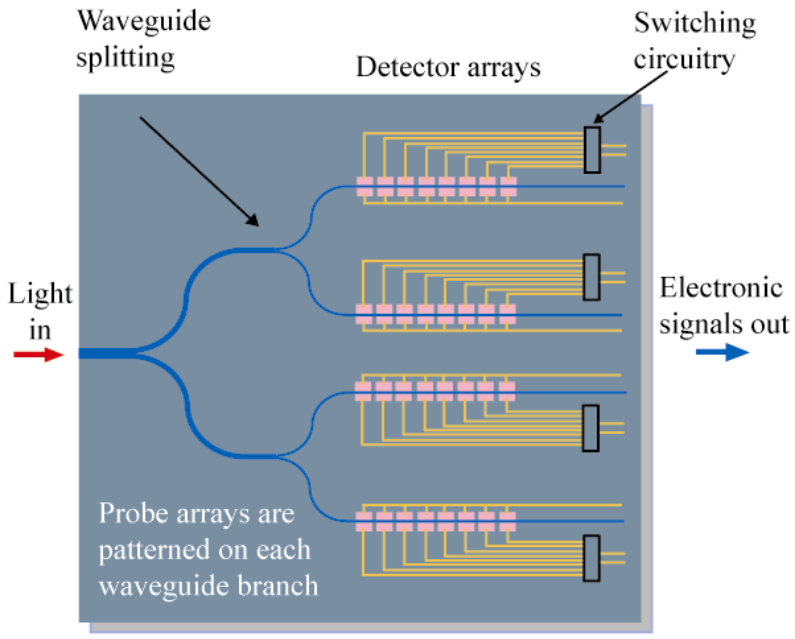

Fig. 5.2. Surface optical intensity shows modal interference between the schematically illustrated modes for a) a 105 nm thick and 4 μm wide waveguide, and b) a 500 nm thick and 10 μm wide waveguide. (from Guangwei)

Similar fabrication flow for LEAC sample without buried detectors (Section 4.3.1) was used to fabricate the these samples. Individual waveguide chips are fabricated from the dielectric coated wafer using conventional photolithography and dry etching techniques. The 110-nm-thick/2-μm-wide rib waveguide core of index 1.8 is made of SiN_x and sits on a 2-um-thick SiO_2 lower cladding of index 1.45 deposited on a Si wafer (Fig.5.3).

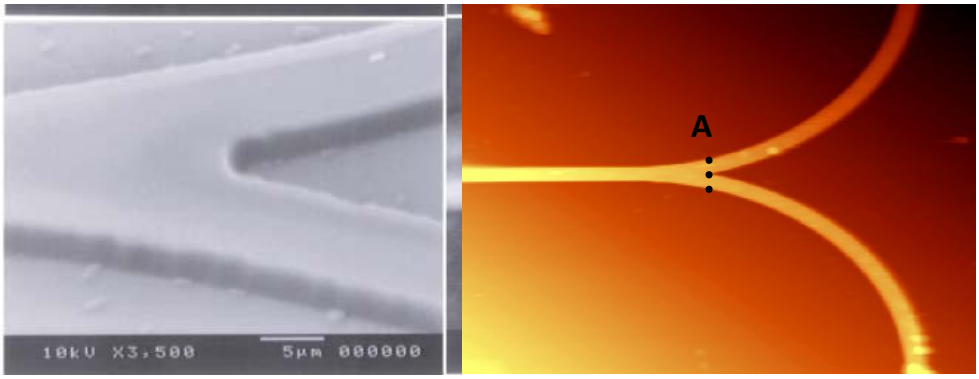

Fig. 5.3. SEM picture of photoresist structure for fabricating y-type splits, and the NSOM Topographic picture of one y-type splitter.

Although this is a 3D waveguide structure, a one-dimensional effective index (core 1.468 surrounded by a region with an effective index of 1.45) is sufficient to determine the lateral mode profiles (Fig.5.4). By comparing the light intensity on cross section A (Fig.5.5) of three y-type splitter samples with the theoretical results obtained by solving the Helmholtz equation, we determined the power ratio and the phase differences ($\Delta\Phi$) of two modes at the start of each splitter.

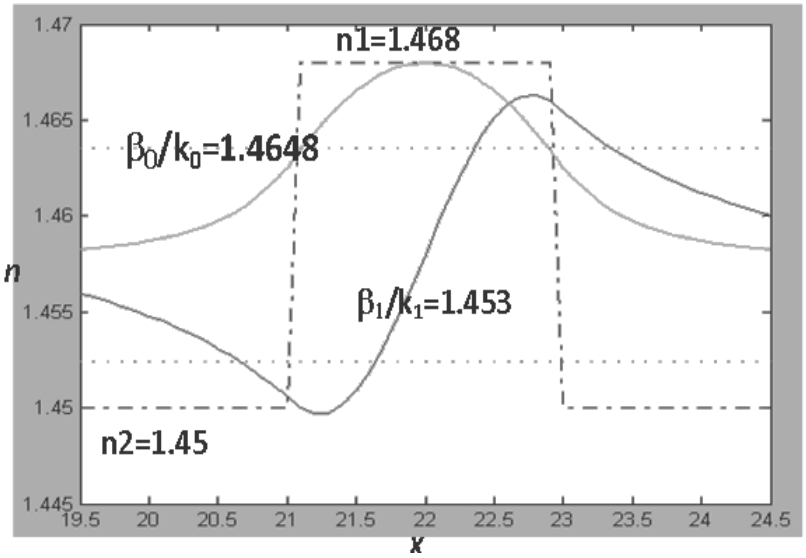

Fig. 5.4 E-field profile of guided modes in the waveguide.

As shown in Fig. 5.5, the FDTD simulation shows that the branching ratio of waveguides was dramatically affected by the phase differences between two modes in waveguides. We measured the branching ratio of three y-splitter samples by using a Near-field Scanning Optical Microscope (NSOM). Comparing the NSOM data on cross section A (Fig. 5.3) of three y-type splitter samples with the theoretical results getting by solving Helmholtz equation, we got the phase differences ($\Delta\Phi$) of two modes at the start of each splitter. With branching ratio and $\Delta\Phi$ of these samples, we found the experiment data matched well with the previous FDTD simulation results, as shown in Fig. 5.6. The phase difference between two modes dramatically affected the branching ratio of the y-type splitter; hence, the length of straight waveguide, which affects $\Delta\Phi$, could be used to adjust the branching ratio in such y-type splitter as shown in Fig 5.5.

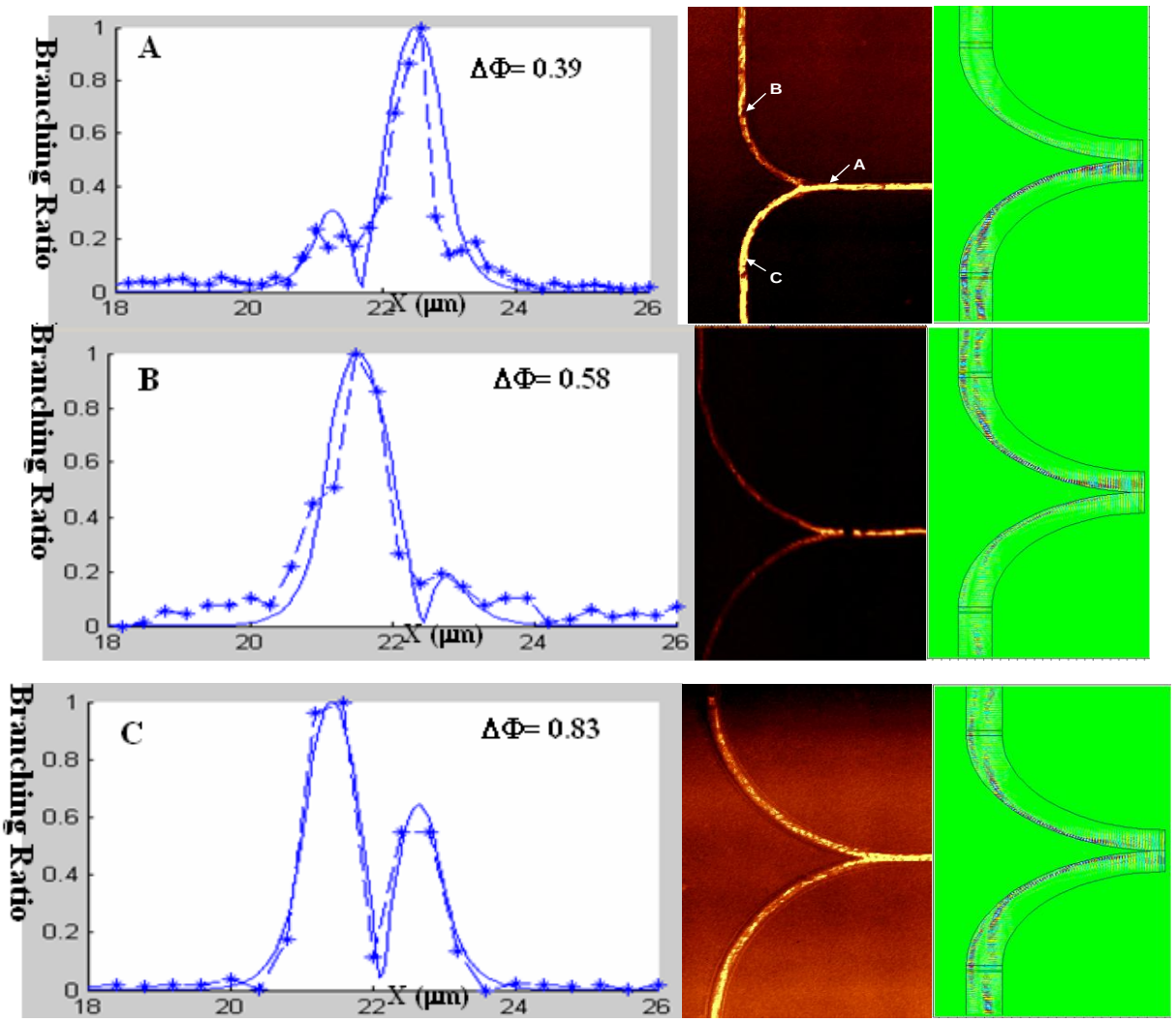

Fig. 5.5. Optical intensity distribution (normalized), NSOM measurement results and the FDTD simulation results of three Y-type splitter samples. Points on dash line are NSOM experiment data and solid curves are theoretical calculation fit.

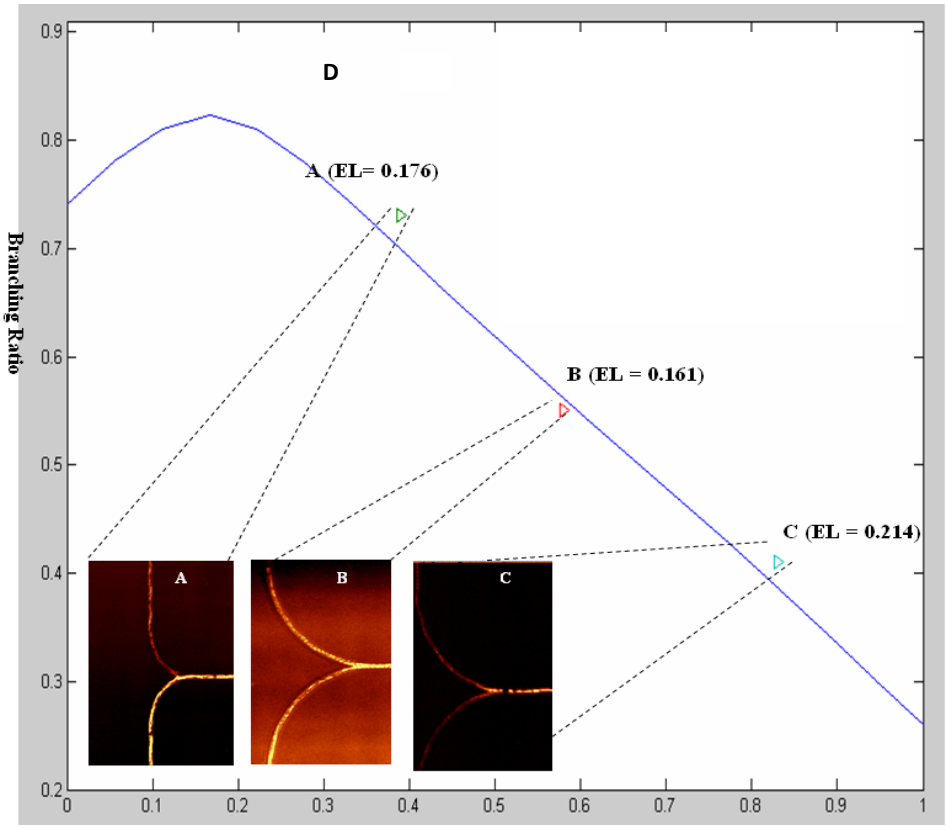

Fig. 5.6. (A) branch ratios as the phase difference varies, points are NSOM experiment results. Insets A, B and C, Near-field images of the measured light intensity on splitters with different branching ratio.

5.2 NSOM measurement on LEAC sensor with BSA & immunoassay adlayers

To determine the evanescent field response to features on a waveguide, different adlayers, including inorganic SiN_x adlayer, photoresist film and C-Reaction Protein (CRP) films were added on a waveguide surface.

5.2.1 Previous measurement with pseudo-adlayer & photoresist adlayer [4][7]

The work reviewed in this section is mostly done by Guangwei Yuan and Matt Stephens. Many interesting phenomena were observed in their work, so we will discuss it to help understand some results we get in later experiments. The most easily fabricated features are of the same refractive index as the core of the waveguide. This type required only an additional lithography and etching step to fabricate. The waveguide fabrication details are discussed in Chapter 4. A 2 μm wide ridge waveguide core was defined by partially dry etching the surrounding SiN_x layer in CF4/O2 plasma on a 2μm thick SiO_2 substrate. The etch depth and thus ridge height was determined to be 21 nm. An artificial adlayer was created by masking 10 μm wide bars oriented perpendicular to the waveguide, and etching the exposed SiNx an additional 17 nm. The waveguide core thickness after the adlayer etch was 88 nm, and the ridge depth was 21 nm. Fabrication flow diagram is shown in the Fig. 5.7.

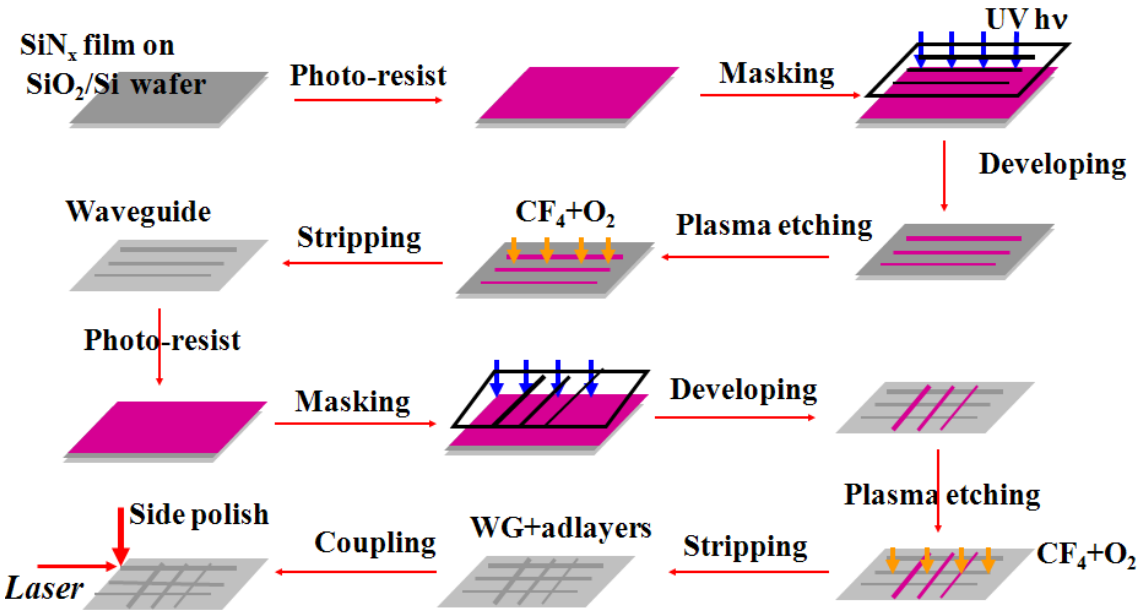

Fig. 5.7. Fabrication flow diagram for waveguide and surface feature. Reproduced from [4].

NSOM was used to measure the evanescent field changes due to SiN_x adlayer formed on top surface of the waveguide core (Fig.5.8(a)). NSOM experiments yielded light intensity and topography maps simultaneously. Fig.5.8(b) shows a topography image over a 10 μm × 100 μm scanned area based on surface height information. The waveguide width appears larger than 2 μm because of the NSOM tip size. Light was coupled into the waveguide from left of the area shown. Fig.5.8(c) illustrates a simultaneously obtained contour plot of the measured light intensity from the same scanned area. The image clearly shows a strong change in the optical evanescent field when the wave encounters the adlayer region.

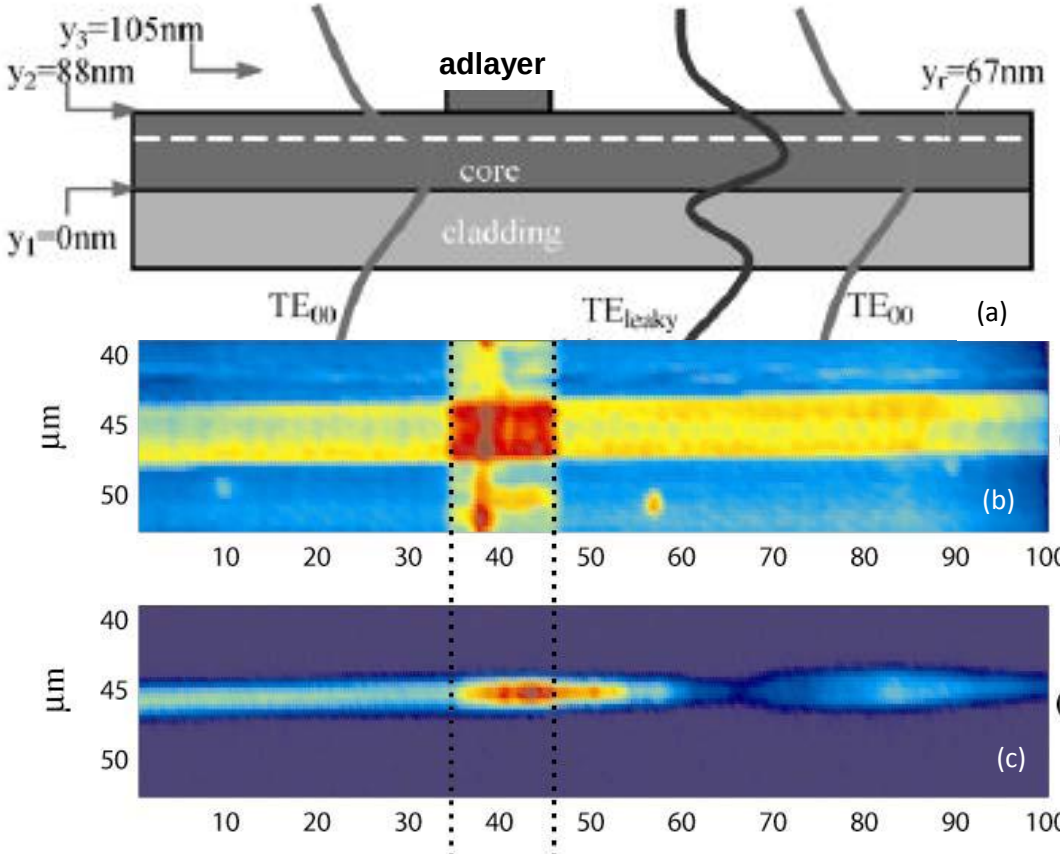

Fig. 5.8. (a) Cross section of waveguide and adlayer (b) plot of the topography along the waveguide and (c) contour plot of measured light intensity for the same region.

The intensity distribution along the centerline of the waveguide from both NSOM measurements and BPM simulations were presented in Fig.5.9, along with the surface height. The BPM simulation results, which include no adjustable parameters, agree very well with the measured results. The input power level when subtracted off the background (P_{bg}=1000 counts) was P=1760 counts and the maximum intensity change, in Figure 6.11, was ΔP=1420 counts. Thus optical intensity modulation capability of the adlayer was about ΔP/P=81%.

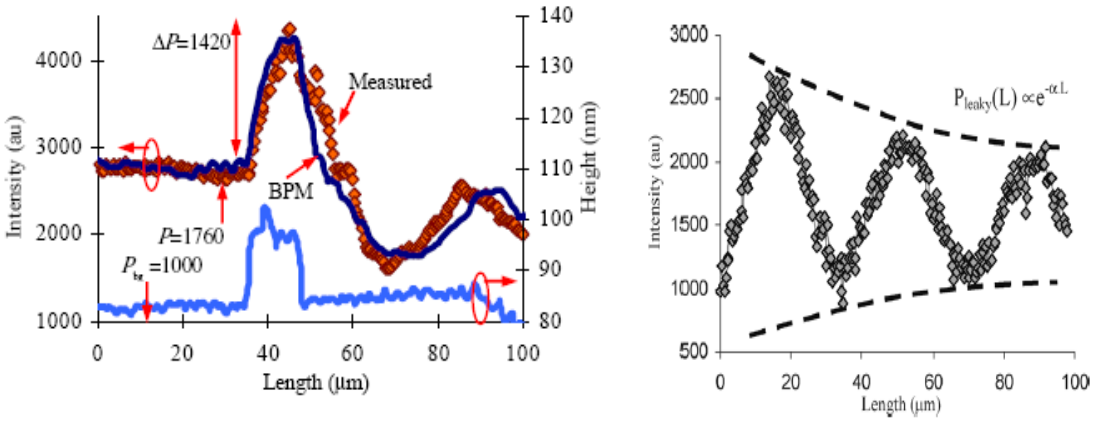

Fig. 5.9. (a) contour plot of measured light intensity for the patterned region. (b) damped oscillation after the patterned region.

In Region after the adlayer, a large, damped oscillation of the evanescent field was observed as well as predicted by BPM calculations. The effective index of the guided mode was 1.459. In addition to the guided mode, a strong leaky mode of effective index 1.441 was also excited by the field perturbation in the adlayer region, which gradually dissipates in this region by leaking into the lower cladding (SiO_2, n=1.45). Fitting the measured data with an exponential decay curve produces an estimated attenuation coefficient of 152 dB/cm for the leaky mode while the guided mode attenuation was 8 dB/cm. The average interference period was measured to be 36 μm, again in good agreement with the 38 μm period predicted by BPM simulations and corresponding to a difference of in effective index for the guided and leaky mode. Similar phenomena was observed in the following experiments. More detail could be found in reference[8][9].

Although strong evanescent field modulations were observed with intentional step changes of the waveguide core, the adlayers' refractive indices were too high to represent that of real

biological materials, which have an average refractive index ~1.5. Thus, photoresist (Shipley 1818) which has a refractive index of 1.55 was patterned cross the waveguide, and field response of the LEAC sensor to this adlayer was investigated using NSOM.

For the waveguides, a 2 μm wide ridge waveguide core was defined by dry etching 16 nm of the surrounding SiNx layer in CF_4/O_2 plasma. 10 μm wide photoresist adlayer (Shipley 1818, n=1.56) was patterned by photolithography perpendicular to the waveguide. To get a thin layer of photoresist (~100 nm), a special method was used to dilute the photoresist. More details will be discussed in Chapter 6. The NSOM measurement showed the thickness of the photoresist ranged from 90-120 nm. Fig. 5.10 shows the longitudinal cross-sectional view of the waveguide and the photoresist adlayer. [4]

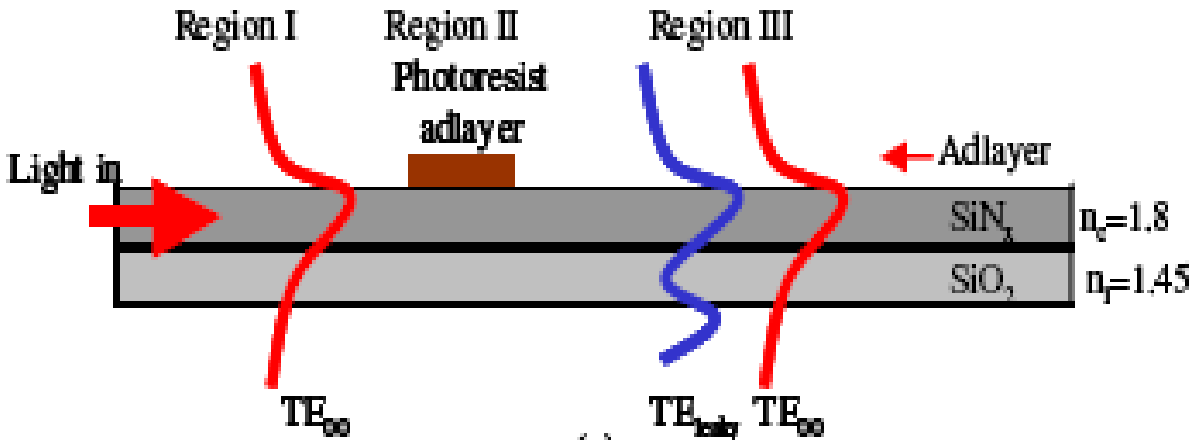

Fig. 5.10. Longitudinal cross-sectional view of the waveguide and photoresist adlayer configuration.

Similar to our previous observations, NSOM measurement revealed a transient modal interference originating from the mode beating between the guided mode and the leaky mode in Region III. Since the optical intensity modulation depth was directly related to the thickness of

the adlayer and the adlayer's refractive index, the strength of the oscillation was taken as an important indicator of the adlayer's optical properties.

The thin blue curve in Fig. 5.11 represents the corresponding plot of the measured light intensity along the top surface of the waveguide in Region I and III, and along the top surface of the photoresist in Region II. The signal in the patterned region decreased rather than increased due to the thickness of the photoresist which lift the NSOM tip up too far from the waveguide surface, and hence the detected power decreased although the total evanescent power in this region increased..

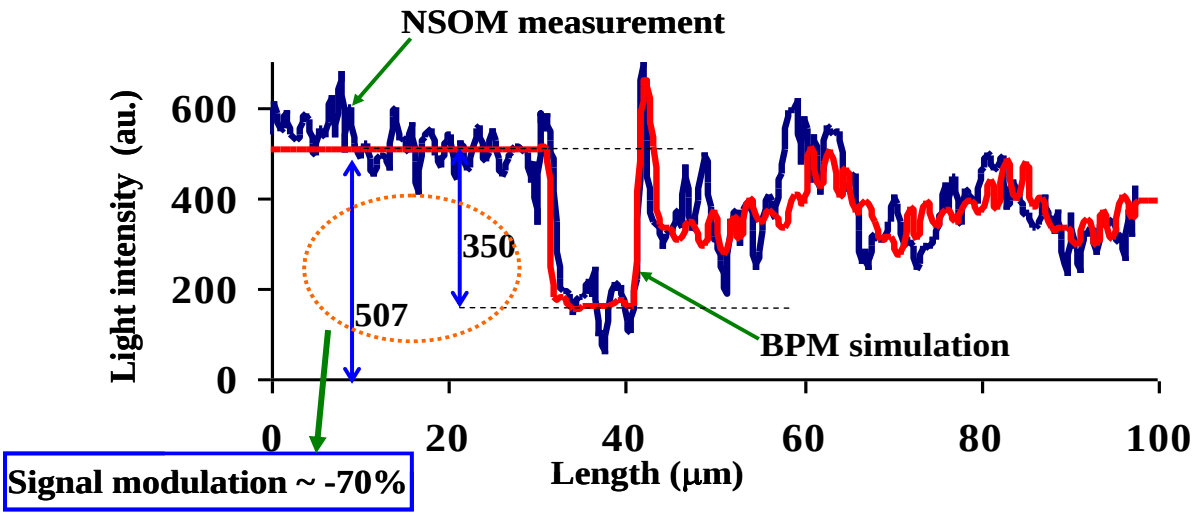

Fig. 5.11. the corresponding plots of the NSOM measured (thin blue) and BPM simulated (thick red) light intensity along the top surface of the waveguide in Region I and III and the photoresist in Region II.

5.2.2 Immunoassay adlayers measurement

The NSOM measurement on the waveguide with inorganic / photoresist (PR) patterning proved the local field shift concept works in the previous experiments. In this section, NSOM measurements were conducted by the LEAC sensor investigators on immunoassay complex adlayers (Fig. 5.12) [8]. The adlayer consists of biotinylated BSA, strept-avidin, anti-CRP and CRP layers. The total thickness of the immunoassay adlayer ranges from 12nm without CRP to 15nm with 95% CRP coverage (Fig. 5.13). Polydimethylsiloxane (PDMS) microfluidic channels were used to pattern the complex onto the waveguide surface. This study was a step in the process of developing an integrated device for biosensing using immunoassay chemistry and presented a more realistic representation of a bioassay than the experiment described previously.

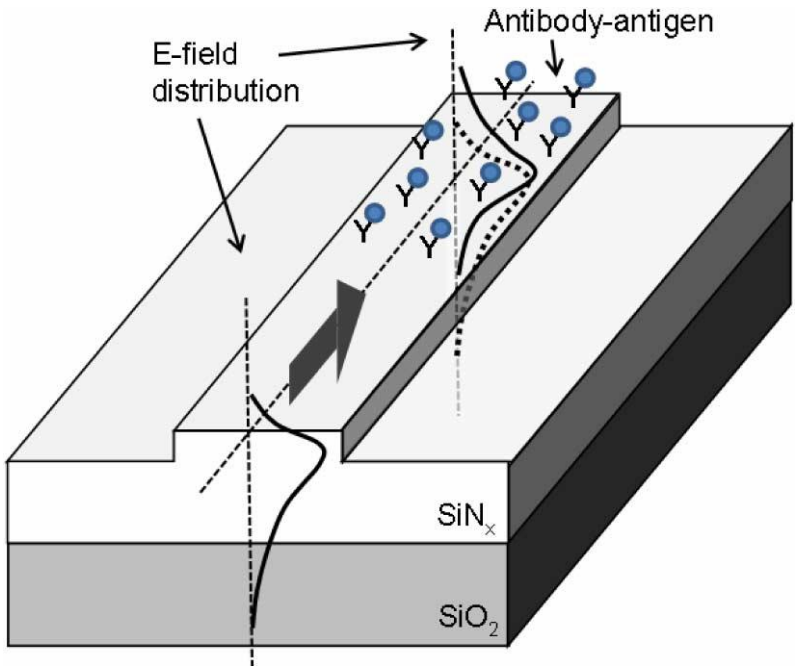

Fig. 5.12. Immobilization of molecular probes such as antibodies on the waveguide surface allows sensitive detection of target molecules such as antigens via specific binding.

A PDMS microfluidic network (Fig.5.14) was used to pattern a four-layer C-reactive protein (CRP) immunoassay on the waveguide surface. The anti-CRP/CRP system (see Fig. 5.13) was selected to be representative of typical antibody/antigen interaction, and it is an important oxidative stress biomarker. In the first step, anti-CRP molecular is immobilized on the waveguide surface using an avidin/biotin non-covalent link, and anti-CRP will act as the bio-receptors on the biosensor surface. Analyte in the buffer solutions was then incubated with the antibody region. The CRP used as analyte here was labeled with a fluorescent tag FITC to allow redundant quantification of the CRP binding using fluorescence microscopy, which will not contribute to the NSOM scanning result.

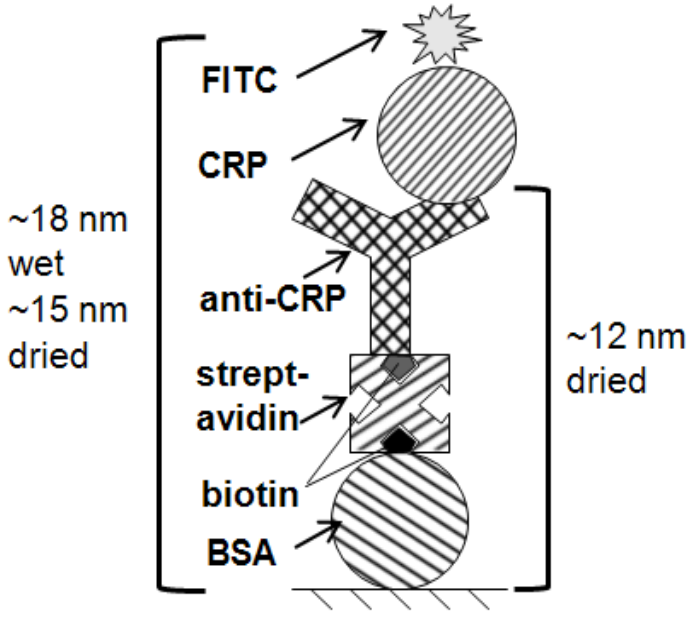

Fig. 5.13. Schematic of CRP adlayer.

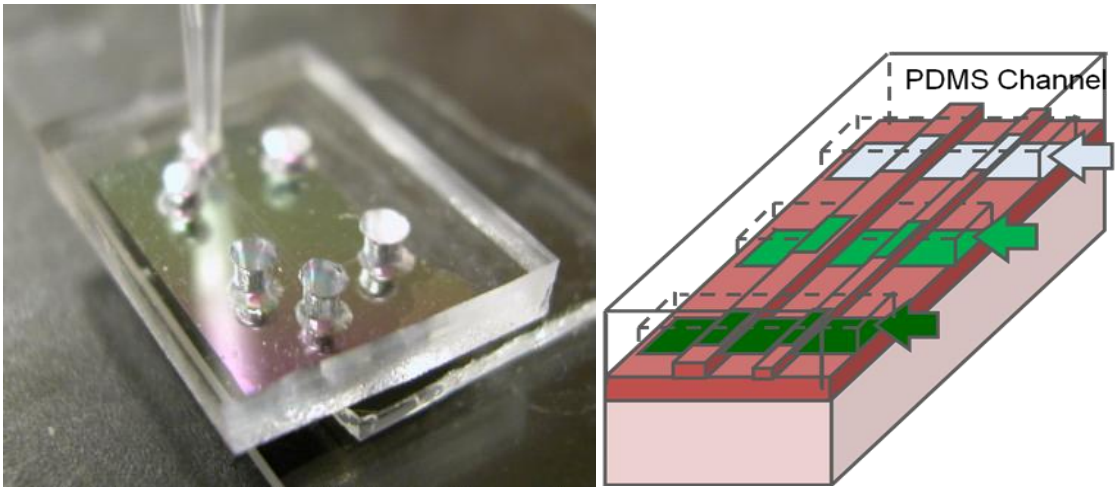

(a) *(b)*

Fig. 5.14. (a) PDMS microfluidic channels (b) Three 50 mm long features are patterned on the waveguide.

Two experiments were done to test the response of LEAC sensor to the CRP patterning. In the first experiment, a high concentration of the CRP (1mg/ml) was selected to apply to the waveguide sample to saturate the binding site and get a uniform CRP monolayer on the patterned region. A single microfluidic channel was used to deliver the CRP molecules to the sample surface. The channel length was 75 mm. NSOM topographic scanning showed the thickness of the CRP region is 15nm. Fig. 5.15 shows the combined picture of a series of NSOM topography and light intensity scans over a 20 μm by 100 μm region. The adlayer measured approximately 75 μm long, and the 2 μm wide ridge waveguide only supports one waveguide mode, the fundamental TE mode. The total SiN_x thickness is 90 nm and the waveguide ridge height is 10nm.

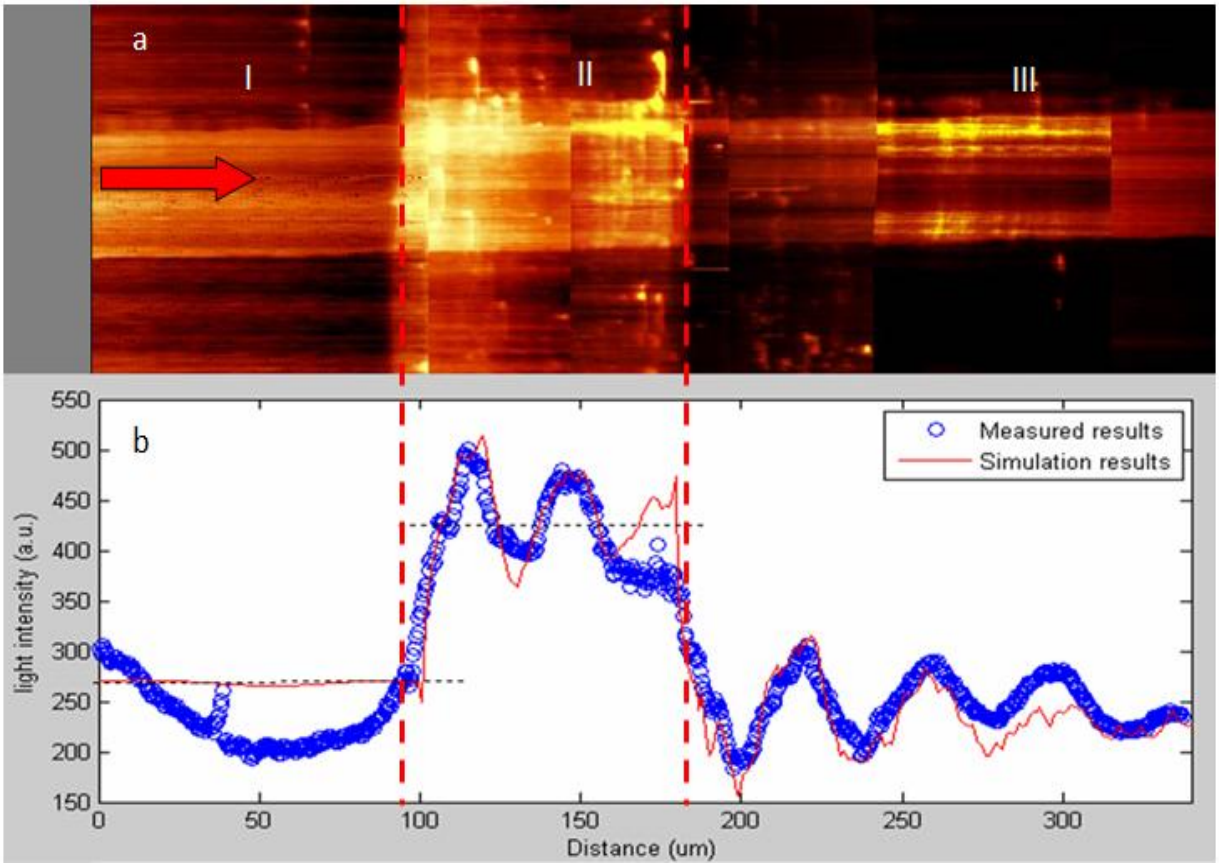

Fig. 5.15. (a) A CRP (1mg/ml) layer on the waveguide (b) light intensities along the waveguide.

The 15-nm-thick adlayer causes the detected evanescent field power to shift from P_0=279 counts immediately before the adlayer to an average $P_{adlayer}$=418 counts during the adlayer, corresponding to an intensity modulation of $(P_{adlayer}-P_0)/P_0$= +49%. Note that although the NSOM tip has moved away from the SiN_x waveguide core above the adlayer, the measured optical power in the evanescent field at the surface of the adlayer is larger, demonstrating the field redistribution locally in the adlayer region that is the operating principle of the LEAC sensor. Negative intensity modulation has been observed in relatively thick, 130 nm photoresist artificial adlayers, as discussed in the last section. In addition to the shift in average field,

oscillation resulting from beating of the different propagation constants of the guided mode and leaky modes is observed after the adlayer region with a beat wavenumber of 0.157/ μm and in the adlayer region with a beat wavenumber of 0.233/ μm.

A two-dimensional BPM simulation of the surface field intensity, superimposed on the measured data in Fig. 5.15, agrees well with the experimental results. The incident beam was assumed to be the fundamental TE mode due to the higher scattering loss of the TM mode. The calculated values for the effective index of the guided and first leaky mode in the adlayer were $n_{GMa}^* = 1.4705$ and $n_{LMa}^* = 1.4470 + i1.0428 \times 10^{-5}$ corresponding to a beat period of $\lambda_0 / (n_{GMa}^* - n_{LMa}^*) = 27.8$ μm, while the guided and leaky mode effective indices outside of the adlayer were $n_{GM}^* = 1.4609$ and $n_{LM}^* = 1.4467 + i1.1518 \times 10^{-5}$ corresponding to a beat period of $\lambda_0 / (n_{GM}^* - n_{LM}^*) = 46.1$ μm. The normal and adlayer regions'calculated beat periods are in reasonable agreement with the observed values of 27 and 40 μm. Note that the leaky mode effective index is less than that of SiO_2 (n=1.45), allowing the leaky mode to radiate into the lower cladding.

As shown in Fig. 5.16, for the second experiment, several concentrations of CRP were allowed to incubate with the anti-CRP patterned on the waveguide surface. A high concentration (0.6mg/ml) was studied to ensure that nearly all the available binding sites on the surface were filled with protein. A dilute concentration (0.6mg/ml) was used to pattern less than a monolayer of protein. Also, there were some patterns that had the final patterned layer as anti-CRP, because buffer with no CRP was added to that channel.

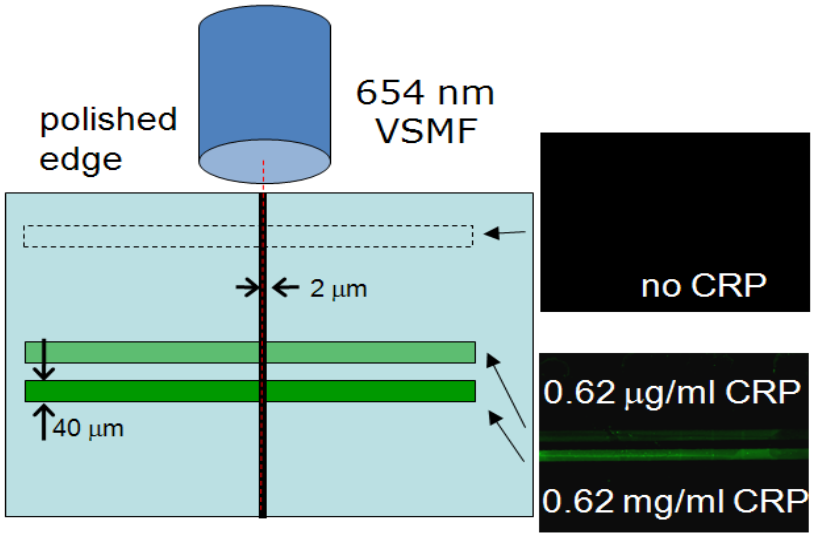

Fig. 5.16. Solutions with different CRP concentrations was patterned on the waveguide using three microfluidic channels.

The immunoassay was patterned using a PDMS microfluidic network (μFN). As shown in Fig. 5.16, the microfluidic channel was designed to make the three probe regions on the waveguide surface separated from each other to prevent the signal crosstalk between different channels. This design allows the placement of multiple probe regions along the same waveguide. Thus, the final system could be operated to allow simultaneous detection of several concentrations of the same analytes or different analytes on one waveguide, which grants the device multinanalyte capability. Xinya He and Brian Murphy carried out the immunoassay patterning on the waveguide surfaces.

To examine the effect of the ridge height of the waveguide to the light intensity response, the waveguide was etched to have a ridge height of 16.5 nm in the second experiment. As shown in Fig. 5.17*(i)*, the topographical results of the adlayer with an average thicknesses of 11.6 nm formed in the absence of CRP. The bright spots in the image correspond to high points presumed

to be processing defects, residue, dust, or other surface contamination. The high points lift the NSOM tip away from the main surface but are too small to significantly affect the local evanescent field distribution and thus decrease the optical intensity at these points. As a result, the optical intensity averaged across the waveguide width, as shown in Fig. 5.17 a(ii), b(ii) and c(ii), has sharp dips correlated with the bright spots that occur on the waveguide. To improve data analysis of the intensity profiles, only intensity data at positions corresponding to topological points less than 4 nm above the waveguide ridge and adlayer is included in the final calculations, which are shown with solid circles in Fig. 5.17a(ii), b(ii) and c(ii). The remaining filtered data are shown with the lines. Least squared linear fits, shown with the open circles, are made to the filtered data in the region before and within each adlayer region to determine the optical modulation, i.e., increase in measured average intensity associated with each adlayer thickness. The local evanescent field modulation increases with increasing adlayer thickness as tabulated in Table 1. The total adlayer thickness varies by ~3 nm, corresponding to the dimensions of CRP, and results in a 5% difference in intensity modulation.

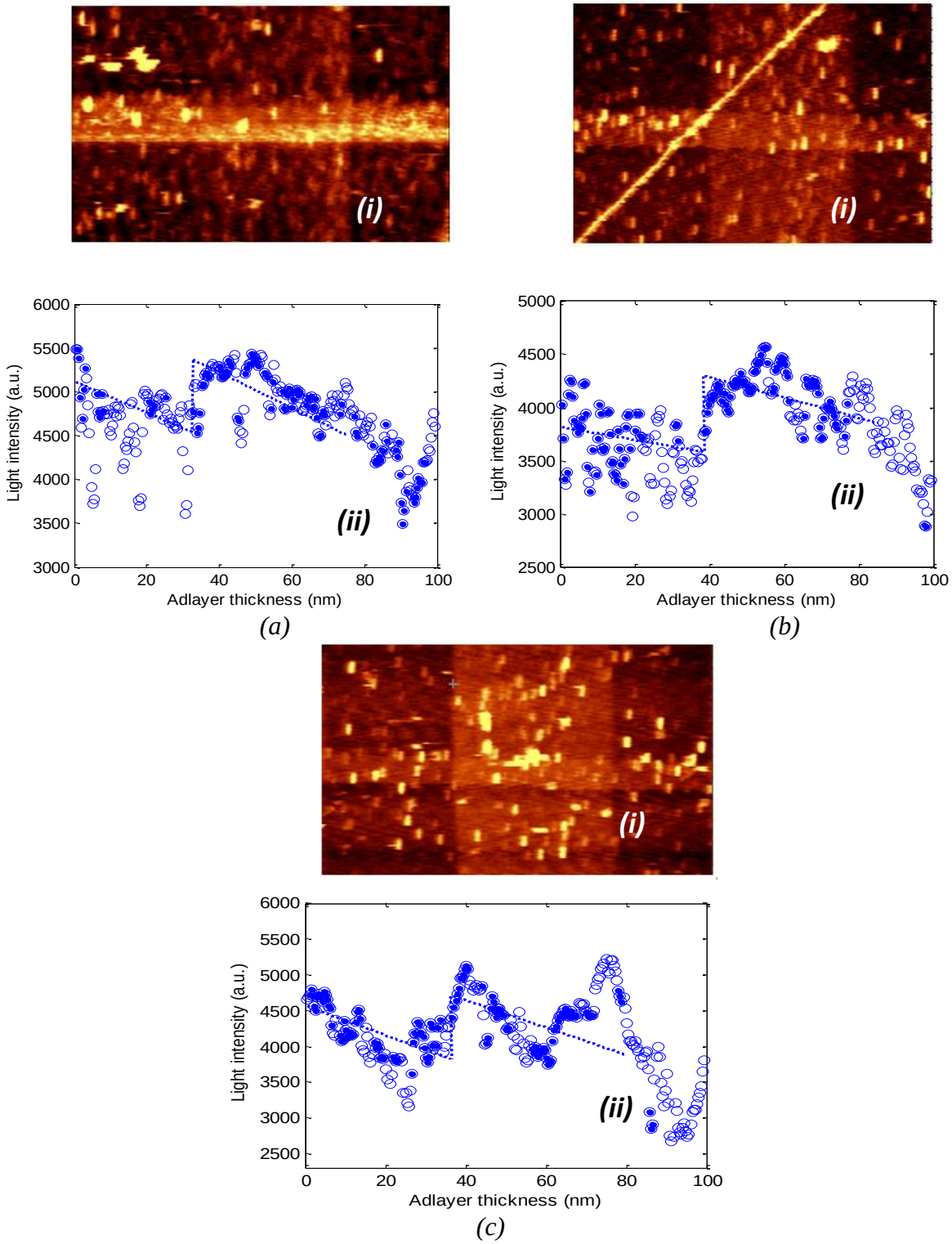

Fig.5.17. a(i), b(i) and c(i): NSOM scanned topographic results a(ii), b(ii) and c(ii): light intensity along the waveguide covered by the adlayers with CRP concentration of (a) 0mg/ml (b) 0.6mg/ml and (c) 0.6mg/ml.

CRP concentration	Adlayer thickness	Intensity modulation
0 μg/ml	11.6 nm	18.23%
0.6 μg/ml	12.4 nm	19.92%
0.6 mg/ml	14.8 nm	23.27%

Table 1. Solutions with different CRP concentrations was patterned on the waveguide using three microfluidic channels.

The expected top surface intensity modulation is predicted to be 10% for 3 nm thickness changes on a waveguide with a 10 nm ridge height. The response of a LEAC biosensor to immunoassay adlayers has been measured with NSOM to probe the top surface evanescent field response on an asymmetric planar waveguide. For a 16.5-nm-high ridge, varying concentrations of CRP resulted in a 3 nm variation in height and a 5% variation in optical intensity on the top surface corresponding to a modulation sensitivity of 1.7%/nm. As discussed in Chap. 4, computer simulation indicated that buried detectors will exhibit larger intensity modulation than the top surface evanescent field, and this is confirmed by the following experiment results in Chapter 6.

References:

[1] R.D. Harris and J.S. Wilkinson, "Waveguide surface plasmon resonance sensors," *Sensors and Actuators B: Chemical*, vol. 29, Oct. 1995, pp. 261-267.

[2] J. Dostalek, J. Ctyroky, and J. Schrofel, "Surface plasmon resonance biosensor based on integrated optical waveguide," *Sensors and Actuators B: Chemical*, vol. 76, Jun. 2001, pp. 8-12.

[3] K. De Vos, I. Bartolozzi, E. Schacht, P. Bienstman, and R. Baets, "Silicon-on-Insulator microring resonator for sensitive and label-free biosensing," *Optics Express*, vol. 15, Jun. 2007, pp. 7610-7615.

[4] R. Yan, G. Yuan, R. Pownall, and K. Lear, "A novel low-loss y-type splitter with adjustable branching ratio," The 20th Annual Meeting of the IEEE Lasers and Electro-Optics Society (LEOS), pp. 543-544, 2007.

[5] Han-Bin Lin, Jung-Young Su, Pei-Kuen Wei, and Way-Seen Wang, "Design and application of very low-loss abrupt bends in optical waveguides," *Quantum Electronics, IEEE Journal of*, vol. 30, 1994, pp. 2827-2835.

[6] Qian Wang, Sailing He, and Lirong Wang, "A low-loss Y-branch with a multimode waveguide transition section," *Photonics Technology Letters, IEEE*, vol. 14, 2002, pp. 1124-1126.

[7] S. Matthew, "Thin film integrated optical waveguides for biosensing using local evanescent field detection," *Dissertation*, Colorado State University, 2009.

[8] R. Yan, G. Yuan, M.D. Stephens, X. He, C.S. Henry, D.S. Dandy, and K.L. Lear, "Evanescent field response to immunoassay layer thickness on planar waveguides," *Applied Physics Letters*, vol. 93, 2008, pp. 101110-3.

[9] G. Yuan, M. Stephens, D. Dandy, and K. Lear, "Direct imaging of transient interference in a single-mode waveguide using near-field scanning optical microscopy," *Photonics Technology Letters, IEEE*, vol. 17, 2005, pp. 2382-2384.

Chapter 6

LEAC MEASUREMENT WITH BURIED DETECTOR ARRAY

The local evanescent array coupled (LEAC) biosensor concept is based on the physical phenomenon of local field redistribution when a waveguide cross-section changes in response to biofilm formation due to specific binding of molecules in localized regions. In Chapter 5, near field scanning microscopy (NSOM) was used to study the optical field response to different films on a waveguide structure[1][2].

For the work presented in this chapter, rather than using bulky NSOM equipment as described in previous chapter, a photodetector array is integrated underneath a waveguide core to sense the vertical shift in the evanescent field due to patterned films. Experimental demonstration of the LEAC biosensing system with integrated buried detectors will be discussed [3-5]. Use of asymmetric waveguides, potentially close to cutoff, and relatively large core to detector distances can provide very large normalized current modulation due to changes in surface film thickness. The multiple element detector array enables multianalyte biosensing on a single waveguide with multiple regions of various immobilized antibodies or other molecular recognition probes. A more complete description of the local evanescent field shift phenomenon appears in Section 6.1.

6.1 Previous work on leaky mode buried detector (1st generation LEAC sensor with buried detector array)

In this section, I will briefly review the work done by Matt Steven and Guangwei Yuan on fabrication and measurement on the 1st generation CSU LEAC sensor. This first device studied was a detector that was designed and fabricated in the CSU cleanroom from a multilayered film sample deposited at the Army Research Lab (ARL).

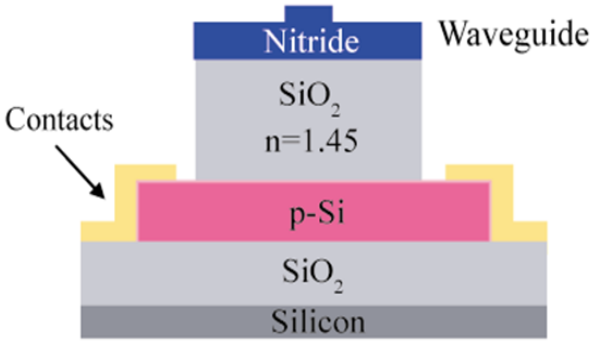

Fig. 6.2. 1st generation LEAC sensor with buried detector array.

As a first step in looking at the application of a buried detector to profile the evanescent field for this sensor device, a prototype detector was designed and fabricated in the CSU semiconductor cleanroom. Fig. 6.2 shows the initial multilayer film structure. The substrate was a thermal oxide wafer and three films were deposited on the substrate in order to form the sensing, cladding and waveguide layers. The thermal oxide isolated the polysilicon detector layer from the silicon substrate to allow the bias current of the detector to only travel through the polysilicon. An additional layer of silicon dioxide provided optical isolation between the core of the waveguide and the detector region while still allowing the field to reach the detectors. To

form the waveguide and sensor complex, a series of etching steps were used to remove the deposited films [6][7].

An experiment was done to determine the change in the detector response when the bulk refractive index of the upper cladding was increased. The detector response was measured with air as the upper cladding and then vegetable oil was added on top of the waveguide to increase the cladding index. As seen in Fig. 6.3, the photocurrent detected for the bare waveguide was lower than the current detected after the upper cladding index was increased. Based on the BeamPROP simulation results[3], this was not the expected result of this experiment. The increase in upper cladding index should have resulted in lower power measured by the detectors due to an upward shift in the evanescent field. One possible explanation for this effect may be that since the oil was not confined to the top surface of the waveguide, some oil flowed between the fiber and the polished face of the waveguide. The oil then formed a more efficient coupling connection due to better index matching in the fiber/air/waveguide interface.

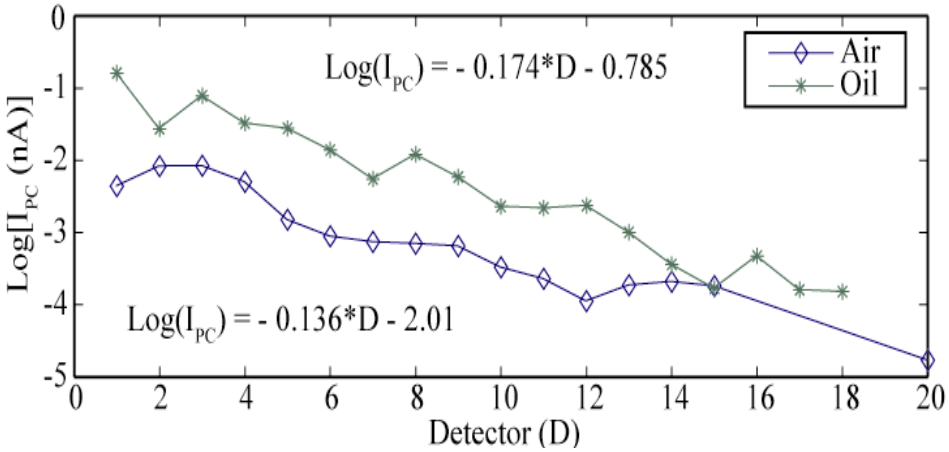

Fig. 6.3. Changing the upper cladding from air to oil affects waveguide loss for the CSU buried detector device. Bare waveguide loss = 13.6 dB/mm, With oil = 17.4 dB/mm. IPC is the photocurrent measured at each detector. Reproduced from [5].

6.2 Second generation of Avago chip

The second device was fabricated with the cooperation of Phil Nikkel and his colleagues using a commercial 0.35μm CMOS technology at the Avago Technologies facility in Fort Collins, Colorado. More fabrication details can be found in Section 4.3.2. Fig. 6.4 shows the structure of the LEAC sensor with buried detector array and the SEM picture of the LEAC sensor chip fabricated by Avago Technology Inc.

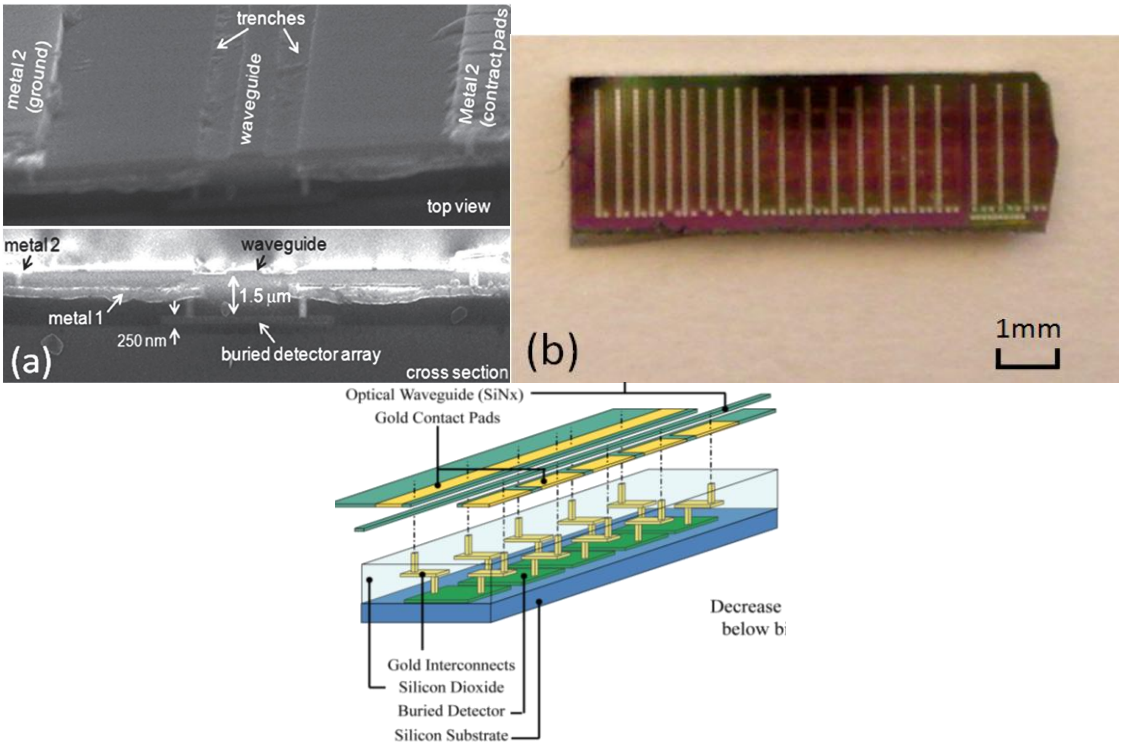

Fig. 6.4. (a) SEM picture of Avago chip (b) LEAC sensor chip fabricated by Avago Technology Inc. (c) structure of the LEAC sensor with buried detector array.

6.2.1 Result on photoresist

To investigate the response of the detector-integrated sensor to an adlayer patterned on the waveguide surface, we chose to pattern the waveguide with a strip of photoresist, whose refractive index is similar to most bio-materials and easy to pattern on the sensor's surface. In the next experiments, we used the following procedures to put an extraordinarily thin photoresist layer on the surface to approach the thicknesses of the actual biofilms.

AZ5214-E photoresist diluted in Propylene Glycol Methyl Ether Acetate (PGMEA) was employed. An AZ5214-E:PGMEA (1:4) solution was spun on the sample at 6000 rpm for 30 sec. The sample was then soft baked at 95°C for 1 min to drive off the remaining solvent. Next, the photoresist layer was exposed with 10 mW/cm^2 405 nm UV light for 45 sec after aligning a 200 μm width stripline photomask on the desired photodetectors. The sample was developed via immersion in AZ400K:H2O (1:4) solution for 5-10 sec. Post baking the sample at 100°C for 1 min hardens the photoresist after developing. NSOM topographic analysis shows the photoresist has a thickness of ~120 nm, as shown in Fig. 6.5.

The first experiment on an integrated sensor chip had a 200 μm long, 120 nm thick photoresist layer patterned across the waveguide above the 9th and 10th buried detectors, as shown in Fig. 6.6(a). Measured photocurrents from detector array elements before photoresist coating, plotted with open squares in Fig. 6.6(b), are proportional to the light in the guided mode and exponentially decrease along the waveguide as the power in the waveguide is attenuated.

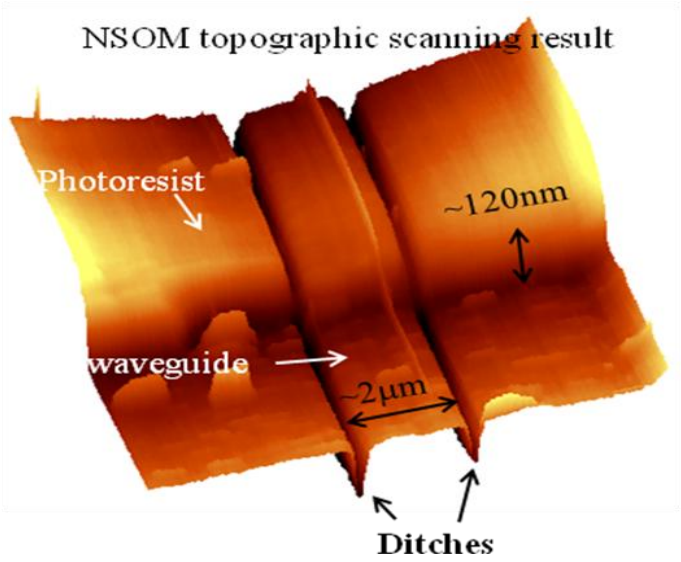

Fig. 6.5. NSOM topographic picture of the thin photoresist patterning.

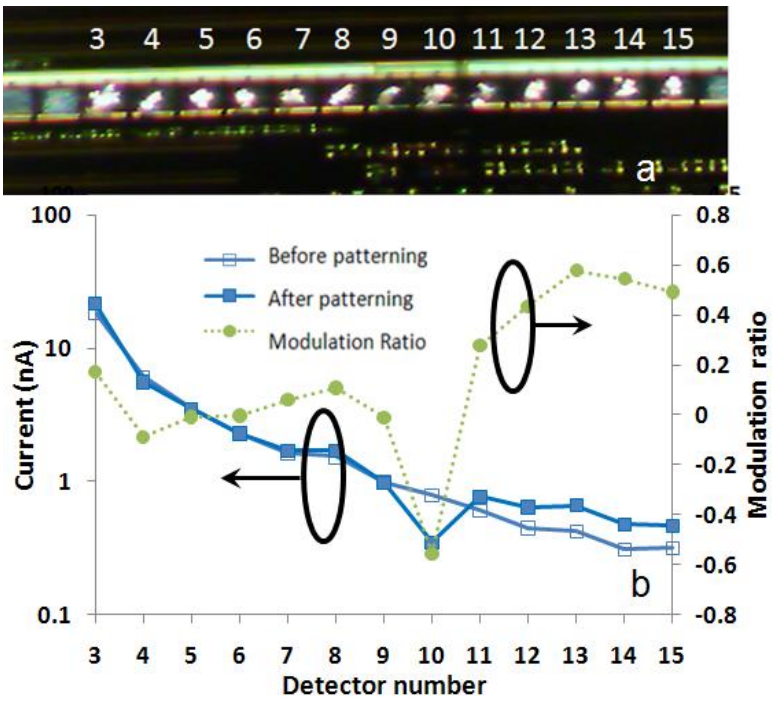

Fig. 6.6. (a) Photo of a LEAC sensor waveguide with 200μm long photoresist patterned above the 9th and 10th detectors. (b) Photocurrents measured before (open squares) and after (squares) the photoresist is patterned as well as the modulation ratio (dotted line).[3]

The modulation ratio for each detector observed after photoresist patterning is shown with circles in Fig. 6.6(b). The ratio decreases from approximately zero to -0.55, i.e. the photocurrent decreases by 55%, due to the patterned photoresist film at the 10th photodetector, before rising back to +0.27 at the 11th detector. These results imply that the light field is shifted up at the waveguide location where there is photoresist (n=1.55), and hence the photocurrent in the buried detector under the waveguide decreases at that location. The modulation ratio beyond the photoresist is higher than the ratio before the photoresist due to reduced absorption by the photodetectors under the photoresist, leaving more light in the waveguide after the photoresist region.

The minimal decrease in photocurrent of the 9th photodetector may be due to light scattering by the edge of the relatively thick 120 nm photoresist film, but the return of the photocurrent to higher levels beyond the photoresist indicates that the large current decrease for the 10th detector is not caused by greatly reduced power in the waveguide. Although the simulation shows the modulation should be larger than 90%, the measured modulation ratio is approximately 55% at the 10th detector. Several factors may cause this difference. First, as described above, the field distribution will shift upward when an adlayer forms on the waveguide, increasing the fraction of optical power in the core (i.e. increasing the confinement factor), and hence increasing scattering due to sidewall roughness of the core. Second, the abrupt transition out of the thick adlayer will also cause strong backscattering near detector #10 when light exits the adlayer region. Third, the lower index contrast between the cladding and core also reduces scatter due to sidewall roughness. Scattered light from the first two mechanisms will increase the photocurrents across the detector and hence decrease the modulation ratio, while the third mechanism will help to

increase the modulation ratio. In this case, considering the thick adlayer (120 nm), the first two mechanisms overcame the last mechanism.

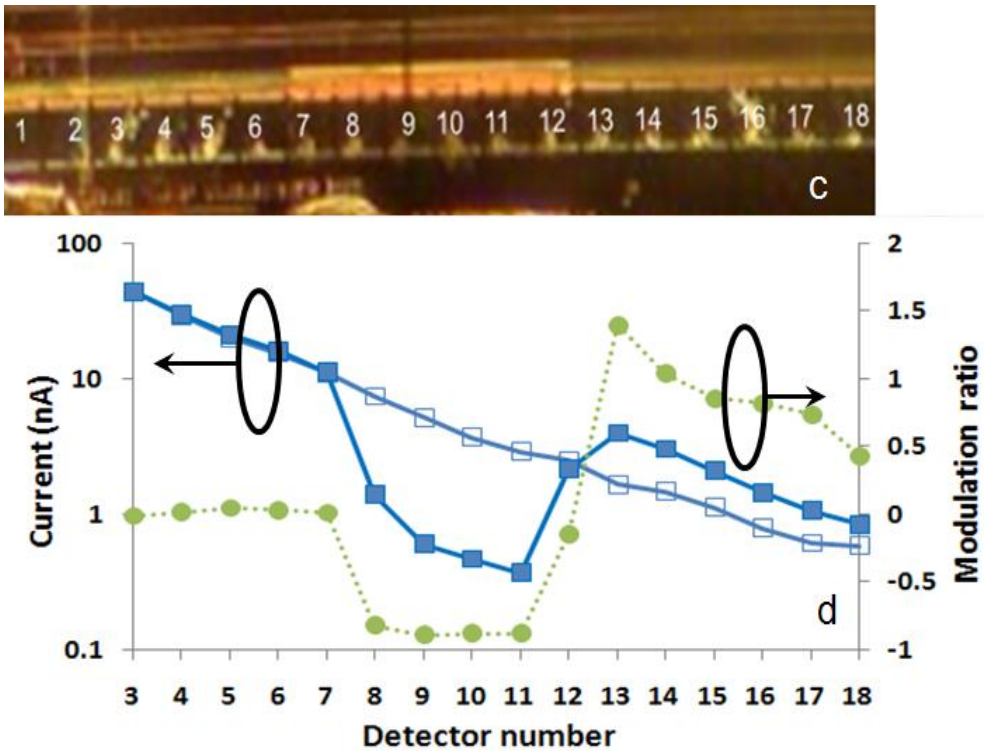

Fig. 6.7. (a) Photo of a LEAC sensor waveguide with 600 μm long photoresist patterned above the 7th and 12th detectors. (b) Photocurrents measured before (open squares) and after (squares) the photoresist is patterned as well as the modulation ratio (dotted line).[4]

To further investigate the impact of the second mechanism, scattering at the beginning and end of the adlayer, a 600 μm long photoresist adlayer was patterned across the waveguide above buried detectors 7 to 12 of a second chip, as shown in Fig. 6.7. Similar to the experiment with the shorter photoresist region, decreased photocurrents are measured at the positions where the waveguide is covered by the photoresist adlayer except on the first detector. However, the largest

modulation ratio in this case is around 87%, which agrees better with the 99% predicted by the simulation results.

The thickness of thinned photoresist adlayer is about 120nm, which is much thicker than expected for immunoassay layers and photocurrent response was near saturation in this case.

6.2.2 Measurement on waveguide sample patterned with BSA

The thickness of thinned photoresist adlayer is about 120nm, which is much thicker than expected for immunoassay layers and photocurrent response was near saturation in this case. Thus, the response of the LEAC sensor to a much thinner adlayer was studied in the following experiments.

To examine the response of the sensor to thinner organic nanofilms that are comparable to the thicknesses expected for immuno-complexes, Bovine Serum Albumin (BSA), whose thickness was two orders of magnitude smaller than photoresist, was patterned on the waveguide.

The BSA was labeled with fluorescein isothiocyanate (FITC), obtained from Sigma, according to the manufacturer's protocol. Phosphate buffered saline (PBS) solution was comprised of 50 mM sodium phosphate, 150 mM sodium chloride, 0.05% Tween 20, in deionized water and adjusted to pH 7.4. FITC-BSA patterning was achieved by manual delivery of 1 mg/mL FITC-BSA in PBS solution using a customized polypropylene-polyethylene copolymer based microcapillary device, as shown in Fig. 6.8. Once delivered to the die surface, the FITC-BSA solution was incubated for 20 min at room temperature in a humidity controlled

chamber. Following incubation, the die was rinsed with PBS, then deionized water, and dried under nitrogen. BSA was fluorescently labeled with FITC to enhance visualization of the pattern, as shown in Fig. 6.9(a), and to quantify the relative amount of adsorbed BSA, but fluorescent labeling is not required for the LEAC sensor mechanism. The low concentration of FITC labeled BSA in conjunction with the moderate evanescent field strength on the top surface is not expected to cause significant changes in the absorption of the guided light. This was confirmed by the observation of similar waveguide decay constants with and without FITC labeling of the BSA.

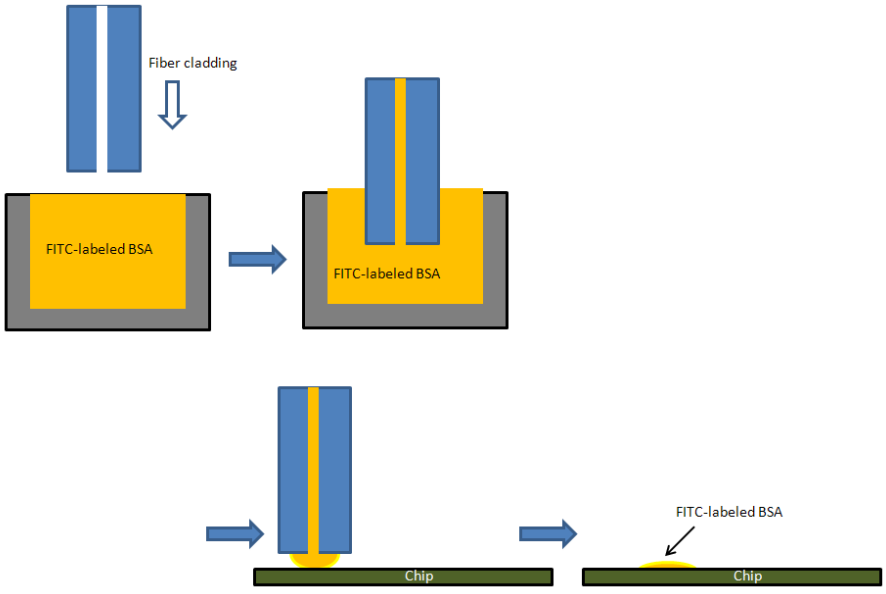

Fig. 6.8. Delivery of FITC-labeled BSA onto the chip surface using a customized polypropylene-polyethylene copolymer based microcapillary from a fiber buffer.

Atomic force microscopy (AFM) was used to scan a 50×50μm square area of the sample indicated in Fig. 6.9(b), to quantify the BSA film thickness. The scanned area was chosen to

include the thickest edge of the BSA pattern as determined from the fluorescence image. The topography demonstrates that the average thickness of the BSA pattern on the left side of the scanned area is 2.5 nm, as shown by column average plotted in Fig. 6.9(c). Assuming that the average thickness of the BSA film is proportional to the fluorescent intensity, the 2.5 nm step height from AFM was used to calibrate the average thickness of the BSA film above each photodetector, and the result indicates it varies from 1.2 nm to 2.5 nm, as shown in Fig. 6.9(d).

As was observed in the photoresist experiment, the modulation ratios at the first and last detector under the BSA nanofilm were affected by light scattering. However, the modulation ratio of approximately -50% at the penultimate detector 13, where the BSA film thickness was estimated to be 2.5 nm, is larger than the BPM simulated modulation ratio of -30%. In this experiment, the LEAC biosensor system shows a sensitivity of approximately 20%/nm when the patterned nanofilm is 2.5 nm.

In the next experiment, a lower concentration (0.1mg/mL) BSA solution was delivered to the chip surface using another method (Fig. 6.9) to obtain a smaller pattern with a well-controlled shape. An 0.8 mm diameter needle is used to punch the PDMS material to form a reservoir. The actual diameter of reservoir is around ~0.4mm due to the elastic property of the PDMS material. The PDMS reservoir was then aligned under a microscope to place it on the desired position on the waveguide surface of the chip. A syringe needle was used to deliver the FITC labeled BSA into the reservoir. Since the reservoir could hold more BSA solution and the shape of the reservoir helped to lower the evaporation rate, a longer incubation time (~30 mins) could be used in this experiment.

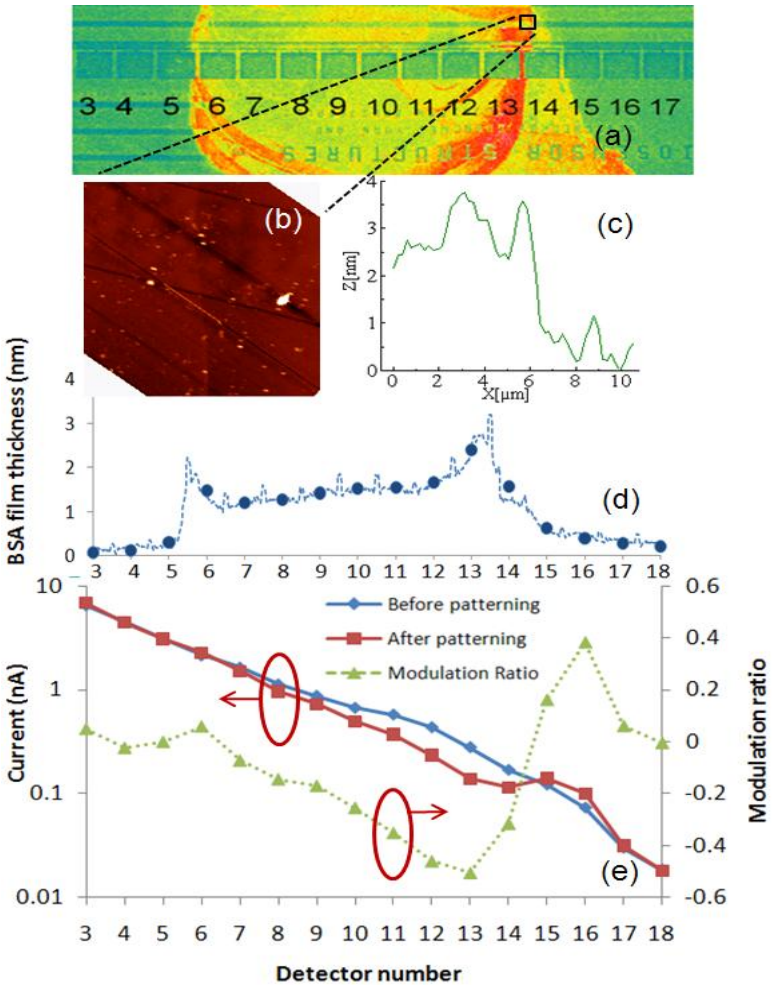

Fig. 6.9. (a) Fluorescence microscope image of a LEAC sensor waveguide with BSA patterned above the 6th-14th detectors. (b) False intensity AFM topographic image at the indicated position containing the edge of the BSA pattern. (c) Average nanofilm height obtained from AFM data. (d) BSA film thickness along the waveguide (dotted line) and average BSA film thickness above each photodetector (solid circle) (e) Photocurrents measured before (diamonds) and after (squares) the BSA is patterned as well as the current ratios (triangles).[3]

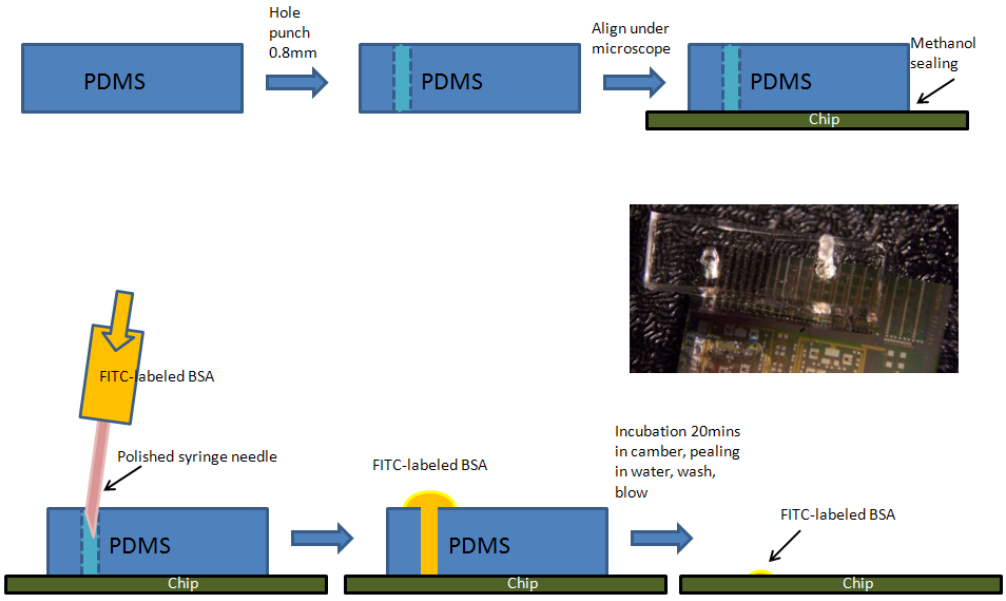

Fig. 6.10. PDMS reservoir patterning method.

The fluorescent picture shows the pattern covers the detector 6 to 9, as shown in Fig. 6.10. As was observed in the last experiment, the modulation ratios at the first and last detector were still affected by light scattering. The maximum modulation ratio of approximately -15% at the 8th detector. Smoother sidewalls in an improved waveguide structure will decrease sidewall scattering and should help to further decrease the difference between simulated and measured results.

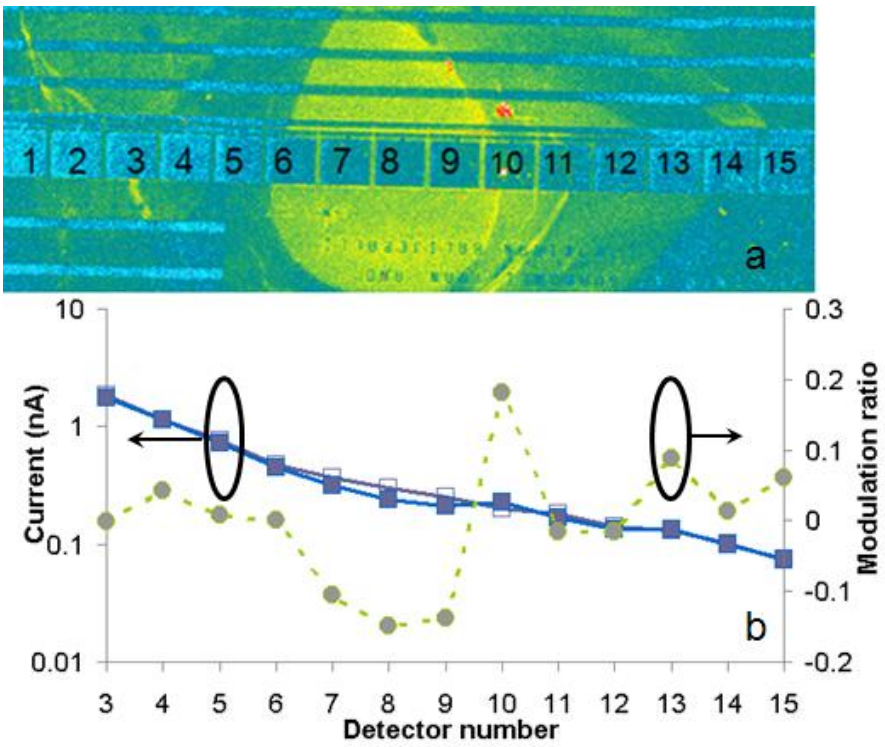

Fig. 6.11. a) Photo of a LEAC sensor waveguide with BSA patterned above the 6th-14th detectors. (b) Photocurrents measured before (open squares) and after (squares) the BSA is patterned as well as the current ratios (dotted line).[4]

6.3 Result on immunoassay adlayer

6.3.1 Mouse IgG and goat anti mouse IgG

To investigate the immunoassay ability of the LEAC biosensor, a mouse IgG antigen/antibody complex was patterned on the sample and the light intensity response was measured after each patterning. The photocurrents and modulation ratios are shown in Fig. 6.12. The microscope picture taken before rinsing the sample shows the antigen/antibody complex was printed above detectors 5 through 9.

As shown in Fig. 6.12, approximately 16% modulation ratio is observed on detectors 6 to 8 due to the goat anti mouse IgG (antibody) patterning. An additional ~4% decrease in photocurrent is detected after the mouse IgG (antigen) incubation. As previously observed, the modulation ratio is smaller on the first and last detectors in the patterned region. The antibody immobilization in this study is not optimized to maximize the binding site density, so an even larger modulation ratio after the antigen incubation could be expected after improving the immobilization method improvement.

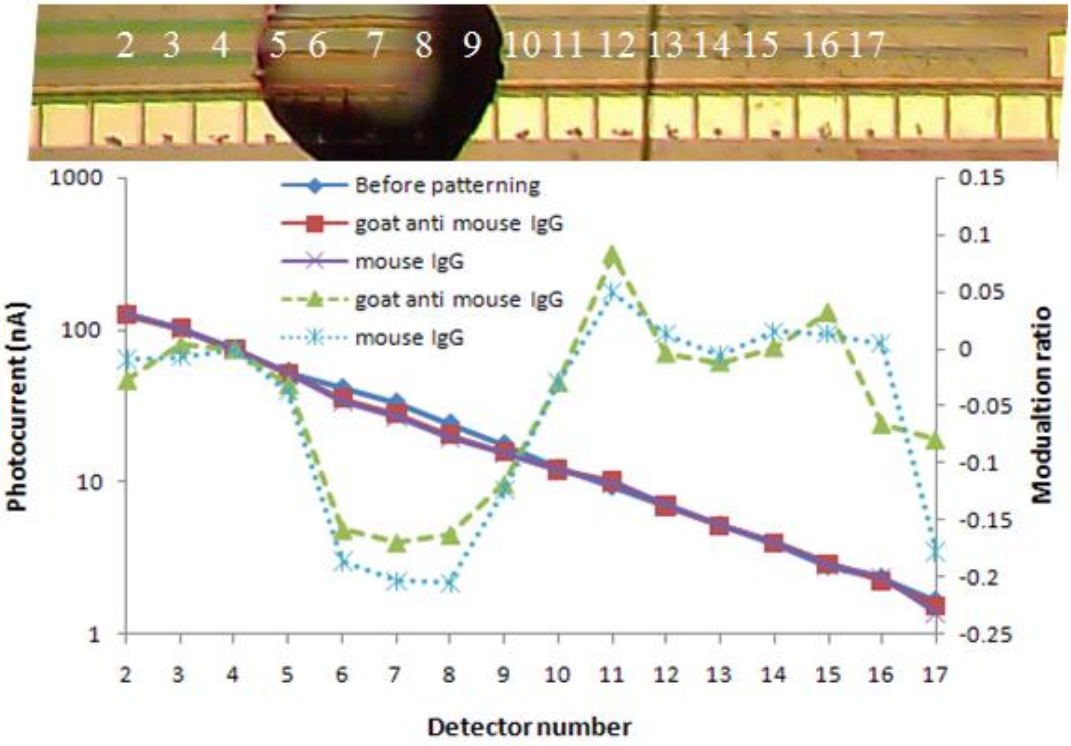

Fig. 6.12. (a) Microscope image of a LEAC sensor chip with goat anti mouse IgG patterned above the detectors 5 through 9 before rinsing. (b) Photocurrents measured before (diamonds) and after (squares) the goat anti mouse IgG /(crosses) mouse IgG is patterned as well as the respective current ratios (triangles and stars).[5]

6.3.2 Hspx antigen/antibody

In this experiment, anti-HspX were immobilized and the surface blocked before exposure to a 100 ng/mL HspX solution to test the response of the LEAC sensor to this TB reactive antibody. The 18 kDa HspX antigen was fluorescently labeled to facilitate direct visualization of the surface coverage, although it is important to note that the sensor itself does not rely on fluorescence. As shown in Fig. 6.13, an approximately 16% modulation ratio is observed on detectors 6 and 7 after the antibody printing. An additional 5% change in photocurrent is detected after 10 hour incubation with the HspX antigen. As previously observed, the modulation ratio is smaller on the first and last detectors in the patterned region.

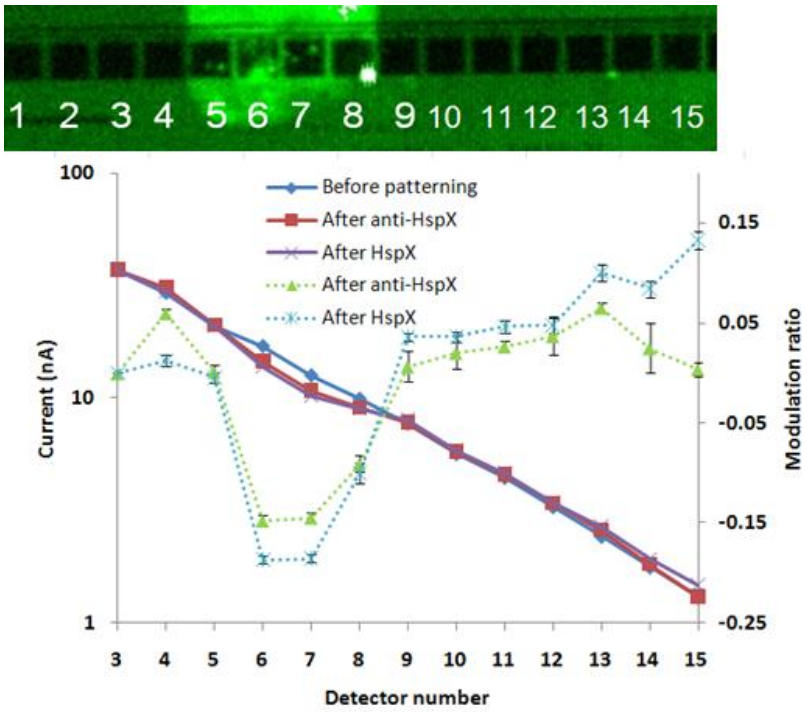

Fig. 6.13. (a) Fluorescent intensity image of a LEAC sensor waveguide with a HspX antigen-antibody complex patterned above detectors 5-8 (b) Photocurrents measured before (diamonds), after anti-HspX patterning (squares), and HspX exposure (star) as well as the measured current modulation ratios (dotted lines.).

The specificity of the LEAC biosensor was investigated in a manner characteristic of traditional diagnostic procedures for serology. TB reactive antigens Ag85 and HspX were utilized as capture probes for potential disease reactive antibodies. After a sample surface treatment to improve probe immobilization, two antigens (200 ng/μL) was printed in two separate locations along the waveguide on sensor chip. Each spot diameter was ~400 μm. The sample was then incubated in 60% humidity for 20 min before being rinsed with DI water and dried. Next, the sample was submerged into a 10 % bovine serum albumin solution for 1 h to passivate the remaining un-patterned surface against non-specific adsorption, after which the baseline photocurrent distribution was measured. The sample was then immersed in anti-HspX solution (200 ng/mL) for 1 h to allow the antibody to bind to the HspX patterned spot, followed again by photocurrent measurements. Although fluorescent labeling is not required for LEAC biosensing, the sample was then submerged in fluorescent-labeled anti-mouse IgG solution for 1 h to mark the presence of the anti-HspX spot (Fig. 3(a)).

As shown in Fig. 3(a), HspX was printed on detectors 4 to 7 as the probe, and antigen 85 was printed on detectors 10 to 13. After incubation and binding of the antibodies to the HspX antigen probe region, an 8% maximum modulation ratio was observed, which corresponds to a 0.5 nm change in average nanobiofilm thickness. No significant change in photocurrent was detected in the antigen 85 spot, indicating anti-HspX did not bind to the antigen-85 probe. Subsequent incubation with FITC-labeled anti mouse IgG resulted in specific binding to the captured anti-HspX, and caused an additional 5% current decrease on detector 6. These results show the LEAC biosensor can be used to selectively detect specific TB antibodies.

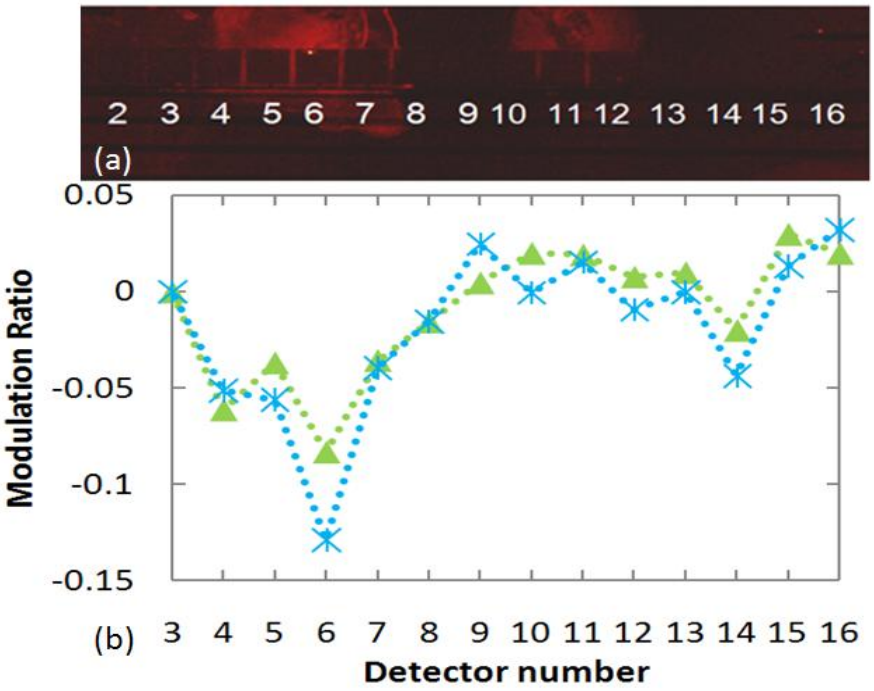

Fig. 6.13. (a) Fluorescent intensity image of a LEAC sensor waveguide with an HspX antigen-antibody complex patterned above the detector 4 through 7 and antigen 85 spot over detectors 10 through 13 (b) Measured current modulation ratios after anti-HspX (triangle) and anti mouse IgG (star).[5]

References:

[1] R. Yan, G. Yuan, M.D. Stephens, X. He, C.S. Henry, D.S. Dandy, and K.L. Lear, “Evanescent field response to immunoassay layer thickness on planar waveguides,” *Applied Physics Letters*, vol. 93, 2008, pp. 101110-3.

[2] G. Yuan, M. Stephens, D. Dandy, and K. Lear, “Direct imaging of transient interference in a single-mode waveguide using near-field scanning optical microscopy,” *Photonics Technology Letters, IEEE*, vol. 17, 2005, pp. 2382-2384.

[3] R. Yan, S.P. Mestas, G. Yuan, R. Safaisini, and K.L. Lear, “Response of Local Evanescent Array-Coupled Biosensors to Organic Nanofilms,” *Selected Topics in Quantum Electronics, IEEE Journal of*, vol. 15, 2009, pp. 1469-1477.

[4] R. Yan, S.P. Mestas, G. Yuan, R. Safaisini, D.S. Dandy, and K.L. Lear, “Label-free silicon photonic biosensor system with integrated detector array,” *Lab on a Chip*, vol. 9, 2009, pp. 2163-2168.

[5] R. Yan, N.S. Lynn, L.C. Kingry, Z. Yi, R.A. Slayden, D.S. Dandy and K.L. Lear, “Waveguide biosensor with integrated detector array for tuberculosis testing,” Applied Physics Letters, vol. 98, pp. 013702, 2010.

[6] S. Matthew, “Thin film integrated optical waveguides for biosensing using local evanescent field detection,” *Dissertation,* Colorado State University, 2009.

[7] M.D. Stephens, G. Yuan, K.L. Lear and D.S. Dandy, " Optical and physical characterization of a local evanescent array coupled biosensor: Use of evanescent field perturbations for multianalyte sensing ", Sens Actuators B Chem, 145, pp.769–774, 2010

Chapter 7

INTEGRATION OF MULTICHANNEL MEASUREMENT SYSTEM AND MICROFLUIDIC CHANNEL

In this chapter, the setup of a multichannel measurement system and the integration of the microfluidic channel into the LEAC sensor will be discussed. In the first part, we will discuss the hardware setup for the multichannel measurement system, including the probe card, the translation stage for the light coupling, the probe station and the external circuitry. Section 7.2 will provide some information about the LabVIEW program, which is used to switch different channels and to log the collected data into the computer. The integration of the microfluidic system in the LEAC sensor will be mentioned in the last part of this chapter. The Microfluidic channel were designed by Rongjin, Iris Yi, Kelly Nienburg and Scott Lynn, and fabricated by Kelly Nienburg. The probe card station was set up by Justin Grantham, Daniel Higley and John Blatt with the help from Rongjin. The circuit was originally designed by Matt Duwe with the help from Rongjin, and revised by the senior design team. The LabVIEW program was coded by Andrew Armstrong. Details of the senior design team's contribution can be found in reference [1].

7.1 Multichannel probe card measurement system with external circuitry

A probe card was implemented into the system to enable probing multiple photodetectors of the LEAC chip simultaneously. Before that, the current across a photodetector for a specific voltage with each detector was measured with 3 microprobes (ground, signal and reference channel). After the implementation of the probe card shown in figure 7.1, probing the first 32 photodetectors under one waveguide on the 3rd generation LEAC chip could be done much efficiently using a system of multiplexers, amplifiers and LabVIEW software, and real time monitoring of the signal change due to analyte binding is possible with the integration of microfluidic channel, which will be discussed in the section 7.3.

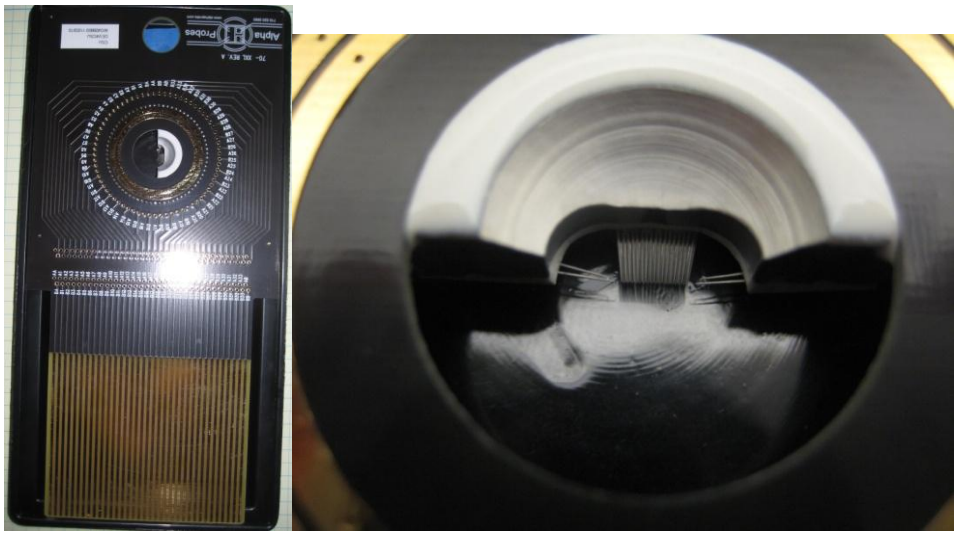

Fig. 7.1 Probe card (left) and close-up look (right).

Since we do not have a high-frequency, high-power, high/low-temperature system, and contact resistance of the aluminum pads on the LEAC chip is relatively low, standard probe card will be suitable for our application. Therefore, we chose to use standard tungsten probes. We chose an epoxy-ring probe card topology to fulfill the moderately high probe density requirement of the LEAC sample (105 μm pitch), as shown in Fig. 7.2. The probe card was ordered from Alpha Probes Incorporated, which is based in Colorado Springs.

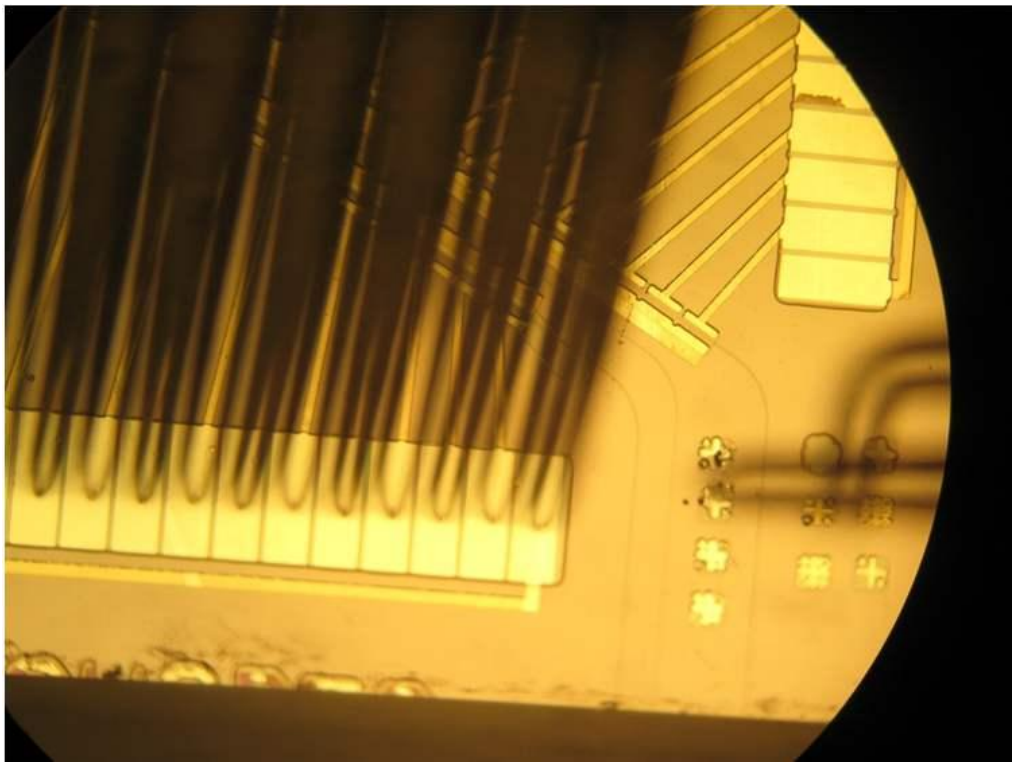

Fig. 7.2 Microscope image of probe card in contact with metal pads (Each pad is 105um Wide).

The probe card consists of a large PCB (4.5” width, 9 3/8” length, 0.062” thickness) which has a hole to accommodate probes on one side and metallic fingers to accommodate connection of the probes to external electronic circuits on the other. Our probe card has a total of 34 probes and 2 edge sensors. All of the photodetectors for a single waveguide share a common ground, and the ground pad is on a different side of the pads, depending on which section of the LEAC chip is being probed. 32 of these probes are used to contact the biasing side of photodetectors and the other two are used to contact ground pads for different waveguides. The edge sensors were placed in line with the rest of the probes but at a strategic distance away to avoid damaging any features on the chip. The edge sensors are used to determine when contact is made.

Figure 7.3 shows a block diagram of the Probing Apparatus. When bringing the probes into contact with the metal pads on the chip, a row of 32 probes must be simultaneously aligned to 32 corresponding metal pads on the sample. After that, laser light is then coupled into a waveguide on the LEAC chip. More details could be found in senior design final report. [1]

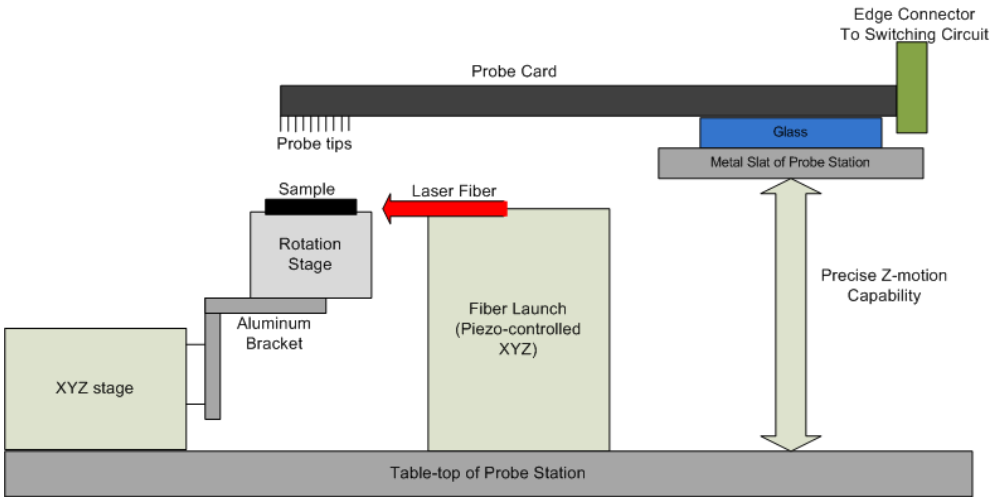

Fig. 7.3 Block diagram of probing apparatus. Reproduced from [1].

An amplification and switching circuit has been implemented to enable the real time measurements on the LEAC chip. A block diagram of the developed system is shown in Fig. 7.4.

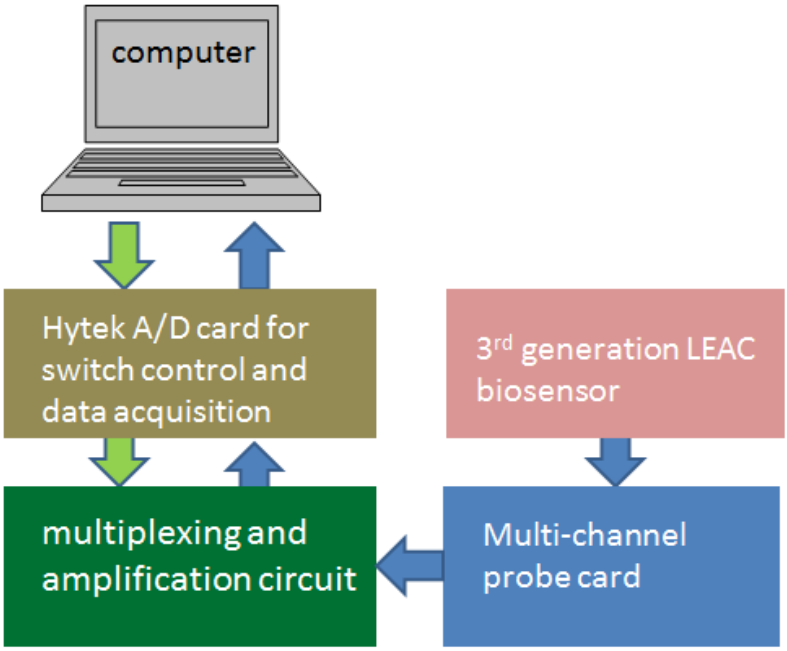

Fig. 7.4 Block diagram of the multiplexing, amplification, and software automated control system.

A multiplexing circuit controlled by a Hytek A/D card was use to switch the 32 different channels. The output of the multiplexers are then fed into a multi-stage transimpedance amplification system that converts the nano-ampere size currents to voltages that can be directly read by the A/D card. A LabVIEW program was adopted to control the A/D card and store the collected data into an excel sheet. More details about the LabVIEW code will be discussed in the section 7.2.

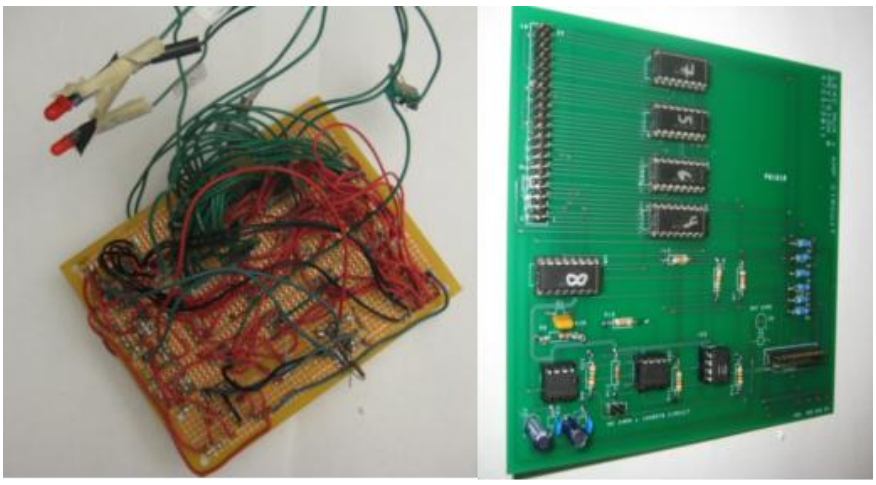

Fig. 7.5 Multiplexing and Amplification Circuit before and after redesign and PCB order. Reproduced from [1].

Figure 7.5 shows the circuit. The PCB layout was designed in PCB Artist available freely through Advanced Circuits of Denver, CO. This PCB version of the board allowed for much easier maintenance and provided much more consistent performance over the previous circuit.

Finally, to allow for the easy control of the circuit an enclosure was modified to house all of the inputs and outputs to the Hytek DAQ device, as well as to display edge sensor information and the ability to toggle the option of which side of the probe card that the potential is applied to.

As mentioned in the introduction part, a large portion of the work is finished with help of the senior design team, and some details of the circuit can be found in the senior design final report "Lab-on-a-Chip Diagnostic Biosensor" [1].

7.2 LabVIEW program for channel control and data acquisition

The goal for implementing software in the LEAC project was to fully automate data collection, i.e., let computer handle a multiplexer to switch between a subset of channels and record large sets of data. In accomplishing this goal, a few key features were defined, including having both a friendly and intuitive user interface, being capable of hours of data record without crashing, and returning data to the user in real-time to facilitate the analysis of data in future experiments. Andrew Armstrong (CBE) in the senior design team was assigned to code the LabVIEW program, and more details about the program could be found in the senior design final report.

With the differentiation between the Front Panel and the wiring diagram, a more user-friendly interface was simplified from a complex juggling act to easily understandable buttons for the job. Figure 7.6 shows version 1.0, the final project version, and how it can be read from left to right to define integral variables before the program is run.

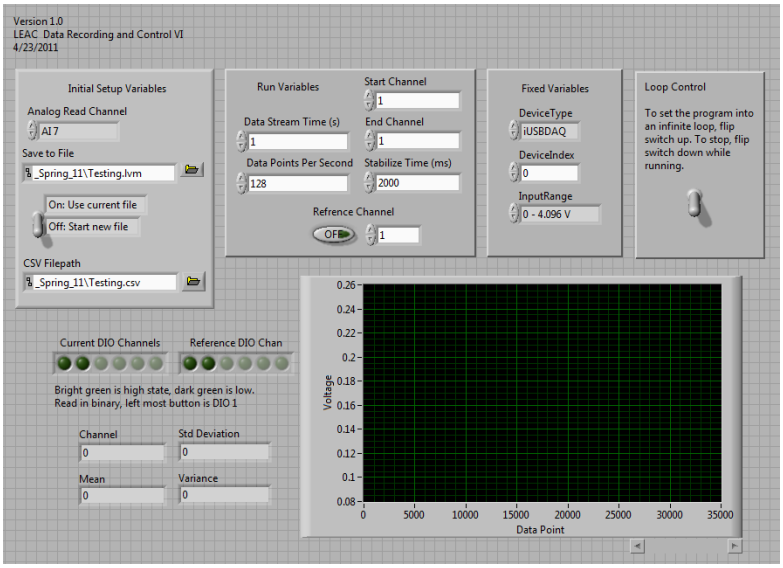

Figure 7.6 Version 1.0 of LEAC Data Recording and Control VI.

7.3 Microfluidic channel design and integration

One of the primary goals for LEAC biosensor was to bring the unit into real-time detection. By designing and integrating a microfluidics [2-6] element to the device, a blood or serum sample could potentially be flowed through micrometer width channels for delivery of analytes to the waveguide.

The first step was to design and order a mask containing microfluidic features. The total area of the mask design had to be small enough to fit within approximately 0.81 cm^2 to avoid covering the metal pads. A cutting guide was also added to improve the precision of the hand cutting by razor blade in the relatively small area. The channels were designed to cross the waveguide perpendicularly and to run parallel to each other. This feature of the mask enables the device to potentially detect different analytes on the same waveguide. Figure 7.7 shows the final mask design. Of the 32 individual pieces, there are 8 each of 4 different designs. The 4 designs vary only in spacing and number of channels.

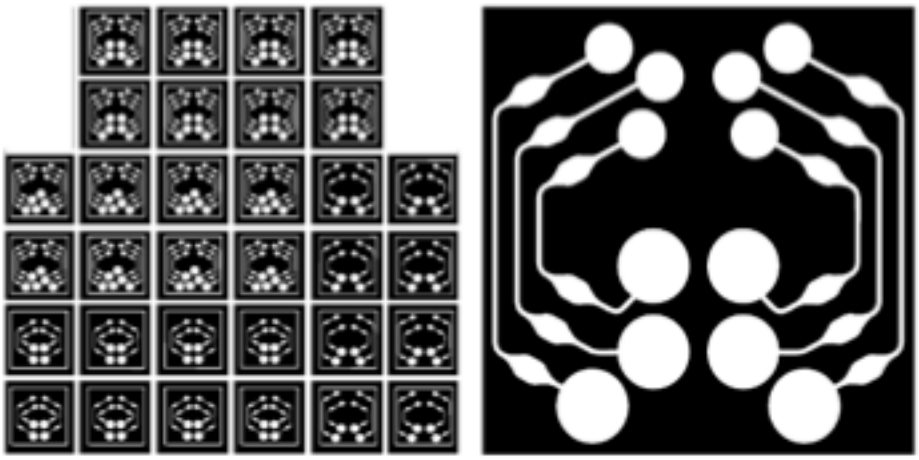

Fig. 7.7 Submitted mask design (left) and single, zoomed view of channel design (right).

An SU-8 mold was needed to make a polydimethylsiloxane (PDMS) channel. First, the SU-8 negative photoresist was spun onto a silicon wafer. Photolithography with the microfluidic channel mask and development of the photoresist gave the mode needed. PDMS was then poured into the mold to make the microfluidic channels. PDMS is a nontoxic, optically transparent polymer that is used for all microfluidics fabrication for the device. PDMS has a refractive index around 1.4, a feature of note for any baseline measurements of the chips.

The channels designed for the lab-on-a-chip device were compatible for either passive [7] or active flow [8] and both types were used for experiments. The advantages to capillary flow are its simplicity, independence from bulky pumping setups, and small sample requirements. However, it was found through fluorescent imaging that fluid would not flow passively through the PDMS when either reversibly or irreversibly bonded to a LEAC chip. It was suspected that either a strongly hydrophobic chip surface or chip features significant enough to hinder capillary forces were responsible for preventing flow. Further investigation of this phenomenon should be investigated in the future.

Because of the restraints on passive flow and the need to continuously switch between sample concentrations for a specific test, active flow with a syringe pump was used for LEAC sensor. Rather than pushing the fluidic through the channel, the system is configured to pull the fluidic through the channel to avoid possible leaking due to the high channel pressure in the “push” configuration. Figure 7.8 shows the system setup. A syringe is used to create a lower pressure, which makes the fluidic flow through the channel.

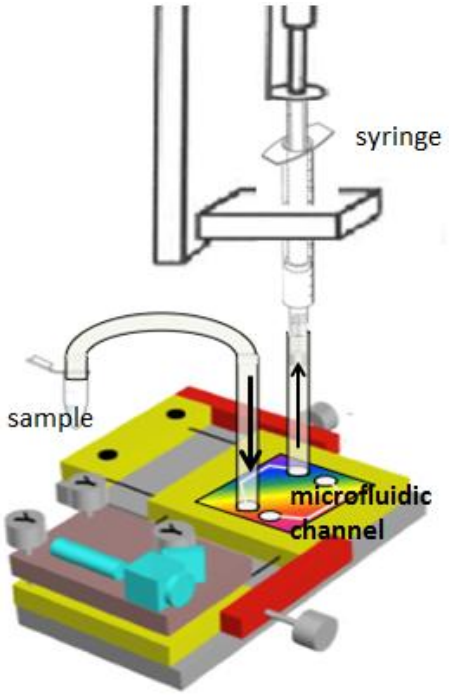

Fig. 7.8 Active fluid flow apparatus configuration. Reproduced from [1].

To irreversible bond between the chip and PDMS, O_2 plasma was used to treat both the chip and PDMS with 18 seconds of plasma oxidation at 20 watt. During plasma oxidation, oxygen radicals attack the surfaces, rendering them more hydrophilic, which lead to a permanent bond. Fig. 7.9 shows a fully fluorescing solution of labeled antibodies running through the channels with a permanent bond on both a glass slide and a chip with no evidence of leaking. More details about the microfluidic channel alignment could be found in the reference [1].

Fig. 7.9 Fluorescing capillary fluid flow through permanently bound PDMS on glass slide (left) and fluorescing active fluid flow through permanently bound PDMS on LEAC chip (right).

References:

[1] Justin Grantham, John Blatt, Daniel Higley, Andrew Armstrong, Kelli Luginbuhl, Kelly Nienburg, Senior design final report 2011, "Lab-on-a-Chip Diagnostic Biosensor", http://www.engr.colostate.edu/ece-sr-design/AY10/biosensors/documents/fallpaper.pdf.

[2] S. Balslev, A. M. Jorgensen, B. Bilenberg et al., "Lab-on-a-chip with integrated optical transducers," Lab on a Chip, vol. 6, no. 2, pp. 213-217, 2006.

[3] R. W. Applegate, J. Squier, T. Vestad et al., "Microfluidic sorting system based on optical waveguide integration and diode laser bar trapping," Lab on a Chip, vol. 6, no. 3, pp. 422-426, 2006.

[4] J. Gao, X. F. Yin, and Z. L. Fang, "Integration of single cell injection, cell lysis, separation and detection of intracellular constituents on a microfluidic chip," Lab on a Chip, vol. 4, no. 1, pp. 47-52, 2004.

[5] J. J. Hu, V. Tarasov, A. Agarwal et al., "Fabrication and testing of planar chalcogenide waveguide integrated microfluidic sensor," Optics Express, vol. 15, no. 5, pp. 2307-2314, 2007.

[6] H. C. Hunt, and J. S. Wilkinson, "Optofluidic integration for microanalysis," Microfluidics and Nanofluidics, vol. 4, no. 1-2, pp. 53-79, 2008.

[7] N. Scott Lynn and David S. Dandy, "Passive microfluidic pumping using coupled capillary/evaporation effects ", Lab on a Chip, vol. 9, 2009, pp. 3422-3429

[8] Douglas B. Weibel, Adam C. Siegel, Andrew Lee, Alexander H. George and George M. Whitesides, " Pumping fluids in microfluidic systems using the elastic deformation of poly(dimethylsiloxane) ", Lab on a Chip, vol. 7, 2007, pp. 1832–1836

Chapter 8

VIRUS DETECTION USING LEAC BIOSENSOR

In this chapter, we will discuss the potential application of LEAC biosensor in virus detection. Virus size polystyrene nanoparticles with two different diameters were used in the experiments. In the first part, different viral diagnostic methods, including several label-free optical biosensors, will be introduced and the scattering mechanism of LEAC sensor will be explained. In section 8.2, experiment methods and sample preparation procedures will be discussed. In section 8.3, numerical methods including Mie scattering model and FDTD method will be used to calculate the scattering cross section of particles with different radius in evanescent field. In the last part, experimental results got from LEAC sensor in detection of 40nm and 200nm polystyrene nanoparticles will be reviewed.

8.1 biosensors for virus detection

In recent years, outbreaks of fast spreading viral diseases, such as bird flu and H1N1, have drawn a lot of concern of the point-of-care virus detection techniques. Timely diagnosis is necessary in order to receive effective antiviral treatment. Traditional virus diagnostic tools, such as ELISA[1], usually require cell culture for 2-10 days depending on the virus before the immunoassay procedures within specialist laboratories. Other methods, such as RT_PCR [2], transcribes the extracted viral nucleic acid from sample into cDNA, which is then detected using fluorescence or luminescence after amplification. Although these methods usually are quicker than the others, they are expensive and the sample preparation procedures are complex. Compared with these established techniques, a desired biosensor for virus detection should be rapid, inexpensive, sensitive and label-free.

Many biosensors based on different detection mechanism have been studied for the virus detection applications. As described in chapter 3, the biosensor could be categorized into different types by the transducers they use. For virus detection, electrochemical sensors, piezoelectric sensors and optical sensors are the most popular biosensors.

Electrochemical sensors are sensors which use electrochemical interrogation including current, potential and impedance changes to transduce the biological recognition event. They were first developed in 1962 with the glucose electrode [3]. Amperometry has been applied successfully to detect Epstein-Barr virus, cytomegalovirus, HSV and HBV [4]. An innovative impedance viral sensor was described by C. Lieber, et al.[5], whereby single viruses detection was proven possible using this techniques (Fig. 8.1). Problems encountered when using

electrochemical sensor include sensitivity to pH changes and non-specific binding of molecules, leading to false positive detection.

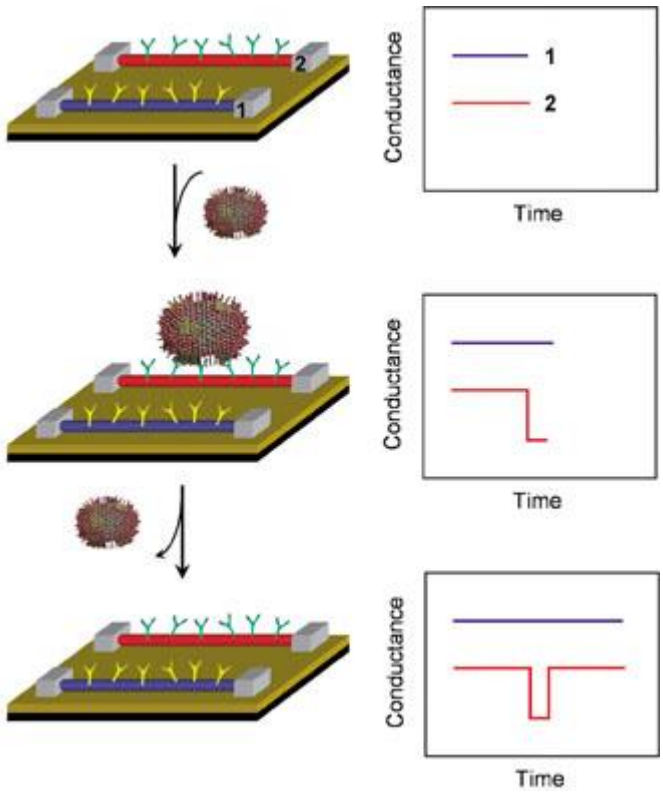

Fig. 8.1 Viral sensor based on nanowires [5]

Piezoelectric viral sensors utilize piezoelectric devices, such as the quartz crystal microbalance (QCM) and micro cantilever arrays, to sense mass change due to the attachment of the virus particles. Because of the relatively high macromolecular mass of virus particles, it is feasible to apply such devices for these analytes. Sensor based on a QCM structure is used by Dell Atti et al. to detect HPV [6]. Work was conducted by Yao et al. [7] to used QCM based

viral sensor to detect HBV, and the limit of detection is 8.6pg L^{-1}. L. Johnson, et al. from Purdue University fabricated a biosensor based on silicon micro cantilevers, as shown in Fig 8.2[8]. Experimental results demonstrated the detection of a single vaccinia virus particle with average mass from 12.4±1.3 fg to 7.9±4.6 fg. These sensors are not suitable for in-field use due to its extreme vibration sensitivity.

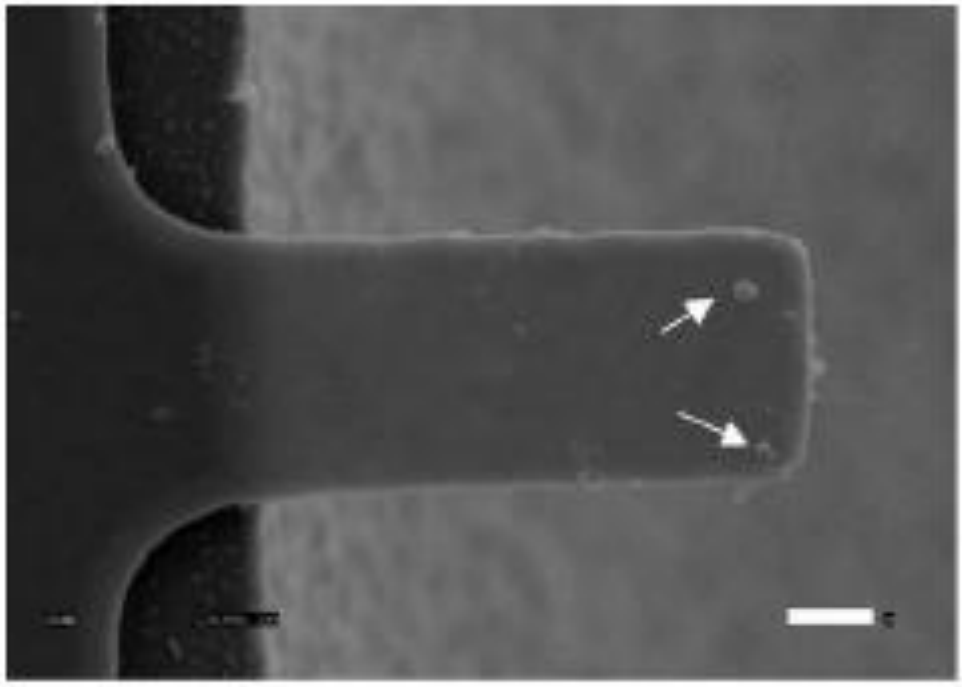

Fig. 8.2 Scanning electron micrograph of virus loaded cantilever beam, scale bar is 1μm. Reproduced from [8]

One of the most popular optical viral sensor formats is based on surface plasmon resonance (SPR). The detection mechanism has been introduced in chapter 3. Rich and Myszka [9] used SPR to observe of many aspects of HIV biology. Due to its detection mechanism, the SPR

sensors are sensitive to temperature and wavelength variation. Except prism coupling methods, the SPR mode coupling efficiencies are low. It is hard to build a portable SPR sensing system.

As discussed in previous chapters, LEAC biosensor has been tested with different antigen/antibodies proteins [10]. The increased refractive index of the upper cladding due to the immobilized antigen/antibody shift the local evanescent field up, and hence lead to a decreased photocurrent detected by the detector array under the waveguide. Instead of the thin uniform adlayer (n=1.55) formed by the immobilized antigen/antibody molecules, the immobilized virus particles form isolated "islands" on the waveguide. Due to the refractive index difference between the particles (n=1.55) and the air (n=1), the evanescent field is scattered out and can be detected by the detector under the waveguide, as shown in Fig. 8.3. Two factors of the particles determine the scattered light intensity, the scattering cross section of the particle and the concentration of the particle.

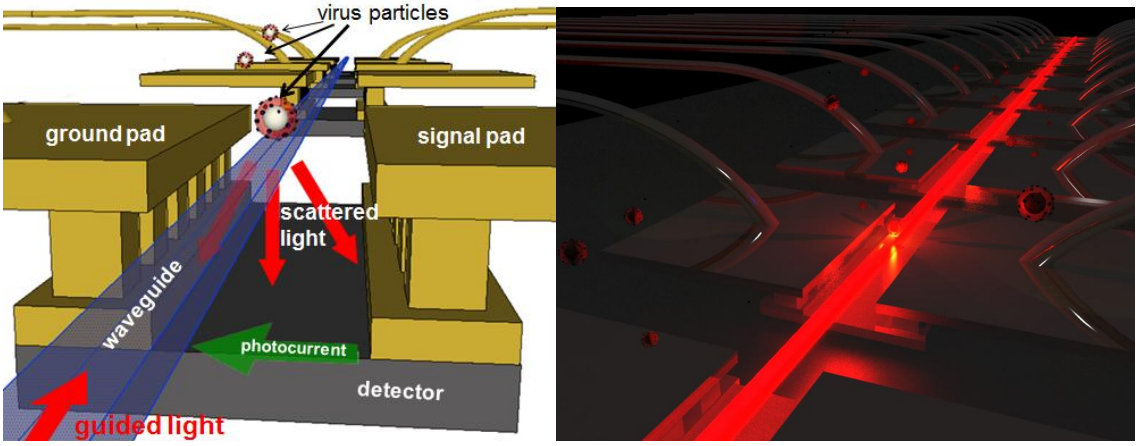

Fig. 8.3 (a) Local scattered light detection mechanism (b) an illustration of the virus detection using LEAC sensor

8.2 Sample preparation

As described in chapter 4, the sample was first polished with polishing papers with different grit sizes. To make the waveguide surface active towards any thiol groups that will be present on the outer surface of a protein, the SiN_x surface of the LEAC sample was firstly rendered with amine terminated surface (NH_2) and then treated with a cross-linked[11].

The affinity existing between biotin and neutravidin was utilized to mimic the binding between the immobilized antibody and the captured virus particles. The same array printer mentioned in chapter 6 was utilized here to covalently isolate biotinylated BSA onto the waveguide over known detection pads. BSA was used to block the rest of the waveguide surface to reduce the possible non-specific interactions. After this, the sensor was incubated with a solution of 200 nm diameter neutravidin coated polystyrene spheres for 30 minutes. Fig. 8.4 shows the immobilized the particles with different diameters.

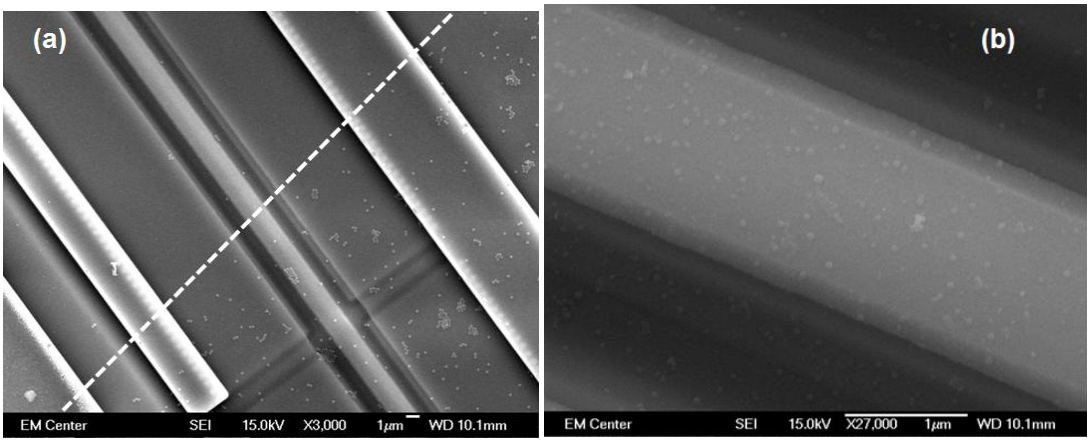

Fig. 8.4 SEM picture of immobilized polystyrene nanoparticles with diameter of (a) 200nm and (b) 40nm. A clear boundary could be seen between the biotinylated BSA printed region and BSA blocked region

8.3 Numerical models

To understand the relationship between the scattering light intensity and the particle size, the scattering mechanism of the small particle in evanescent field is studied in this section.

The size parameter, p, is defined as

$$p = \frac{\pi d}{\lambda} \tag{8.1}$$

where d is the radius of the particle and the λ is the wavelength of the incident light. When the particles are much smaller than the wavelength of light (p<1), the scattering cross section of the particle could calculated using Rayleigh approximation,

$$\sigma_s = \frac{2\pi^5}{3}\frac{d^6}{\lambda^4}\left(\frac{n^2-1}{n^2+2}\right)^2 \tag{8.2}$$

where n is the refractive index of the particle, and d is the diameter of the particle.

From above equation, it shows the Rayleigh scattering strongly depends on the size of the particle and the wavelengths. When d increases, the intensity of the Rayleigh scattered radiation increases rapidly.

When p > 1, the small particle approximation is not valid. Mie theory [12], also called Lorenz–Mie theory, should be used in this case. Mie theory allows the calculation of the electric and magnetic fields inside and outside a spherical object and is generally used to calculate how much light is scattered, i.e., the total optical cross section. One difference between Mie scattering

and Rayleigh scattering is the Mie resonance, as shown in Fig. 8.5. The existence of resonance of Mie scattering makes it a useful method to measure particle size using scatted light.

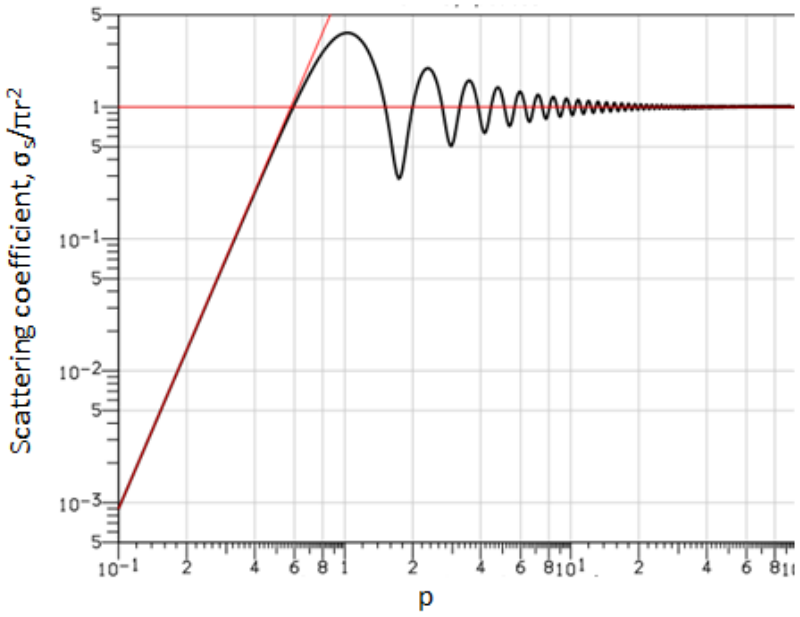

Fig. 8.5 Scattering coefficient VS. p for metal particles. Reproduced from http://en.wikipedia.org/wiki/Mie_theory.

For the two kinds of nanoparticles used in our experiments (40nm and 200nm), the size parameter, p, are 0.21 and 0.96. For the 200nm polystyrene nanoparticles, Rayleigh approximation is not applicable, so Mie theory is used in the following calculations.

Since the particles are immobilized above the waveguide, the incident light in this case is the evanescent field that exponentially decays into the upper cladding with a decaying constant, α, can be calculated by

$$\alpha = \frac{2\pi}{\lambda}(n_{eff}^2 - n_{upper}^2)^{1/2} \tag{8.3}$$

where n_{eff} is the effective index of the guided mode in the waveguide, and n_{upper} is the refractive index of the upper cladding. Different from traditional Mie scattering in plane wave, the incident energy flux given by the time-averaged Poynting vector is not constant over the geometrical cross section of the particles due the exponentially decaying E-field distribution. The scattering of evanescent waves by large spherical particles has been studied by Chew et al. in 1979 [13], and their theory was corrected by Liu et al in 1995 [14]. Some other models and theories were proposed by different groups to study the relationship between the particles-interface distances vs. scattered light intensities [15]. The scattering of evanescent wave by small particles has been studied by M. Quinten et al. in 1999 [16]. According to their research results, higher multipole contributions are strongly enhanced for evanescent field excitation as compared to plane-wave excitation and increase further with the angle of incidence, resulting in corresponding changes in the scattering and extinction spectra.

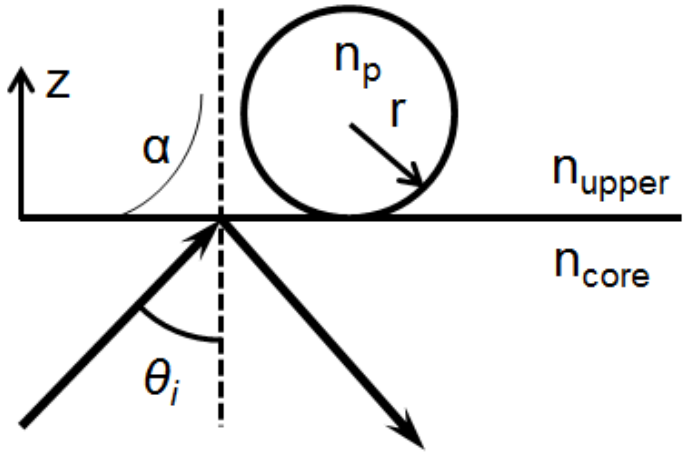

Fig. 8.6 Geometry of the scattering problem

The waveguide guided mode in the LEAC sensor is TE mode [15]. According to paper [14], the Mie scattering cross section, A_{sca} , is

$$A_{sca} = \frac{\lambda^2}{2\pi n_{upper}^2} \sum_{n=1}^{\infty} (2n+1)(\left|a_n(r)\right|^2 \Pi_n(\theta_i) + \left|b_n(r)\right|^2 \Gamma_n(\theta_i)) \tag{8.4}$$

$\Pi_n(\theta_i)$ and $\Gamma_n(\theta_i)$ are the size-independent weighting factors normalized from Mie coefficients to count incident wave as evanescent field. $a_n(r)$ and $b_n(r)$ are the Mie coefficients. θ_i is the incident angle as shown in Fig 8.6. r is the radius of the particle. n_{upper} is the refractive index of the upper cladding.

The averaged incident light intensity over the cross-sectional area of the particle perpendicular to the Poynting vector of the evanescent wave is [14],

$$\tilde{I}_0 = \frac{1}{\pi r^2} \iint S_{inc} dA = I_0 e^{-2\alpha r} \frac{n_p}{n_{upper}} \sin\theta_i \frac{I_1(2\alpha r)}{\alpha r} \tag{8.5}$$

where $I_1(2\alpha r)$ is the modified Bessel function of order 1 with argument $2\alpha r$.

Thus, for our problem, normalizing total scatted light power by particles with radius of r to particles with radius r_0, we get

$$P(r) = \frac{e^{-2\alpha r} \frac{I_1(2\alpha r)}{\alpha r} \sum_{n=1}^{\infty} (2n+1)(\left|a_n(r)\right|^2 \Pi_n(\theta_i) + \left|b_n(r)\right|^2 \mathrm{T}_n(\theta_i))}{e^{-2\alpha r_0} \frac{I_1(2\alpha r_0)}{\alpha r_0} \sum_{n=1}^{\infty} (2n+1)(\left|a_n(r_0)\right|^2 \Pi_n(\theta_i) + \left|b_n(r_0)\right|^2 \mathrm{T}_n(\theta_i))} \tag{8.6}$$

For wavelength of 654nm, the normalized scattered power for particles with different diameters from 20 nm to 200 nm is plotted in Fig. 8.7. The scattered power of a single 200 nm particle is 39 times larger than a 40 nm particle.

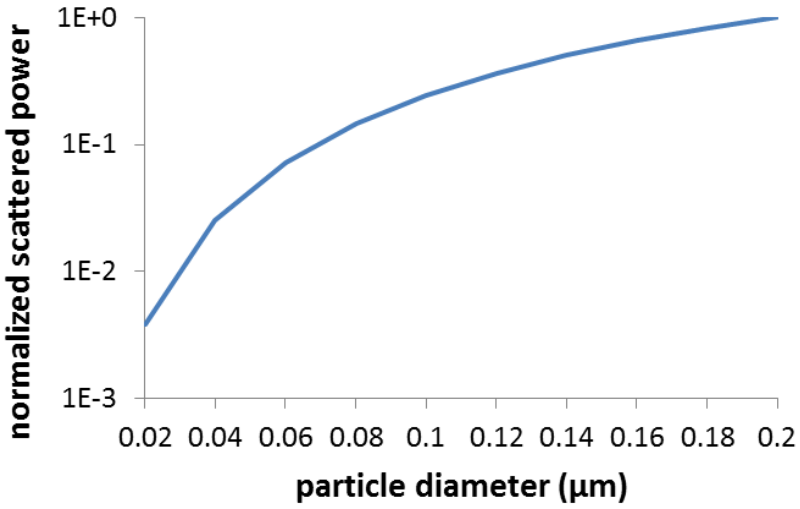

Fig. 8.7 Normalized scattered power vs. particle diameter

8.4 Experimental results by using 40 nm and 200 nm polystyrene particles

The signal measured using LEAC biosensor is modulation ratio, defined as

modulation ratio = $(I_p-I_0)/I_0$

where I_0 is the photocurrent measure before the immobilization of the nanoparticles and I_p is the photocurrent measured after the immobilization.

The modulation ratio from individual detection pads and the particle numbers per detector is shown in Fig. 8.8. The particle number on each detector is calculated using the fluorescent

microscope image. On detector 4-7, where there were little to no captured particles, the modulation ratio remains small number. It can be seen that the modulation ratio on detector 8-11 has a sharp increase due to the present of the polystyrene nanoparticles. The modulation ratio drops to negative value after detector 12; this is because of less guided power in the waveguide due to the increased scattering loss in the particle immobilized region.

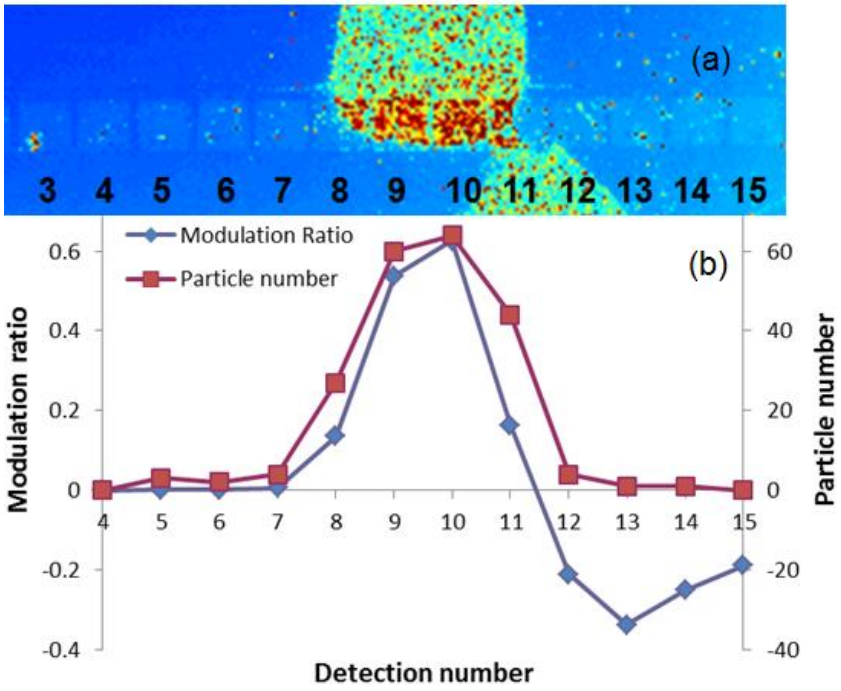

Fig. 8.8 Particle number distribution along the waveguide and the modulation ratio measured from different detectors. The particle diameter is 200nm.

It should be noticed that the decreased guided light power in the waveguide lead to decreased scattered light power measured by the detector with larger numbers. A correction factor is needed to compensate this effect.

It was found that the particle number on different detectors ranged from 20-70. A correction factor for each detector, K_i, was needed to cancel out the effect of the increased loss due to the patterned particle. α_w is the propagation loss along the waveguide before the particle patterning. More details about the calculation could be found in Appendix B.

$$K_i = \frac{e^{-\alpha_w \cdot (i-1)}}{\prod_{n=1}^{i-1}(e^{-\alpha_w} - \Delta S_n)} \quad \text{where } \Delta S_n = \frac{N_n}{N_1} M_1 (1 - e^{-\alpha_w}) \tag{8.7}$$

Fig. 8.9 shows the corrected modulation ratio vs. a particle count. The data were collected from 3 LEAC biosensors chips, and the 3 samples give consistant result fall on same trend line. The sensitivity for these 200 nm particles is appx. 1%/particle.

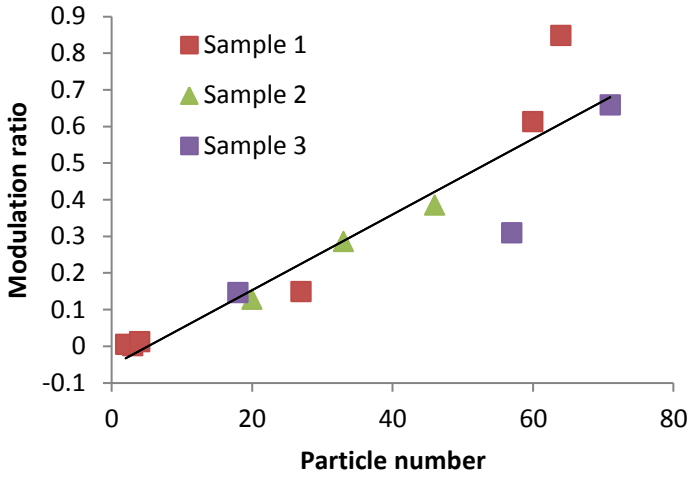

Fig. 8.9, Dependence of corrected modulation ratio on particle number for 200 nm diameter polystyrene nanoparticles. The sensitivity is ~1%/particle.

Similar to 200nm particles, the relationship between modulation ratio and particle number for 40nm particles are plotted in Fig. 8.10 for the single biosensor chip used for this particle size.

The sensitivity for 40nm particles is ~0.04%/particle. The sensitivity for 200nm particle is approximate 25 times larger than 40nm particles. Compared with the calculated results in section 8.3, which is 39 times larger for 200nm particle, this experimental ratio is slightly smaller.

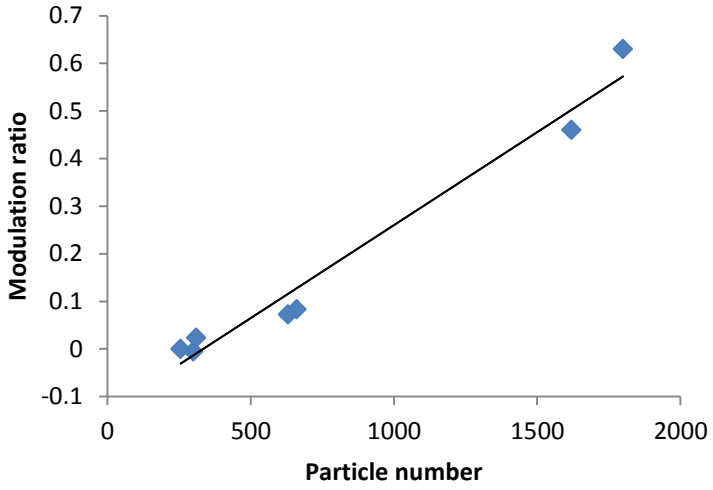

Fig. 8.10 Dependence of corrected modulation ratio on particle number for 40 nm diameter polystyrene nanoparticles. The sensitivity is ~0.04%/particle.

Polystyrene nanoparticles with two different diameters, 40nm and 200nm, were detected by the LEAC biosensor. The sensitivity for the 200nm particle is ~1%/particle and it is 0.04%/particle for the 40nm particle. The particle scattering light intensity was calculated using the Mie scattering method in evanescent field described in reference [14], and the calculated ratio of scattered light intensity for 40nm and 200nm particles was 39, which is larger than the experimental ratio, 25.

References:

[1] A.C.M. Boon, A.M.F. French, D.M. Fleming, M.C. Zambon, "Detection of influenza a subtypes in community-based surveillance", J. Med. Virol., vol. 65, 2001, pp. 163

[2] WM Freeman, SJ Walker, KE Vrana, "Quantitative RT-PCR: Pitfalls and potential", Biotechniques., vol. 26, 1999, pp. 112

[3] L.C. Clark, C. Lyons, "Electrode systems for continuous monitoring in cardiovascular surgery", Ann. N.Y. Acad. Sci., vol. 105, 1962, pp. 20

[4] C.F. Ding, F. Zhao, M.L. Zhang, S.S. Zhang, "Hybridization biosensor using 2,9-dimethyl-1,10-phenantroline cobalt as electrochemical indicator for detection of hepatitis B virus DNA", Bioelectrochemistry, vol. 72, 2008, pp. 28

[5] Fernando Patolsky, Gengfeng Zheng, Oliver Hayden, Melike Lakadamyali, Xiaowei Zhuang, and Charles M. Lieber, "Electrical detection of single viruses", PNAS, vol. 101, 2004, pp. 14017–14022.

[6] D. Dell'Atti, M.Zavaglia, S. Tombelli, G. Bertacca, A.O. Cavazzana, G. Bevilacqua, M. Minunni, M. Mascini, "Development of combined DNA-based piezoelectric biosensors for the simultaneous detection and genotyping of high risk Human Papilloma Virus strains", Clin. Chim. Acta, vol. 383, 2007, pp. 140

[7] C. Yao, T. Zhu, J. Tang, R. Wu, Q. Chen, M. Chen, B. Zhang, J. Huang, W. Fu, "Hybridization assay of hepatitis B virus by QCM peptide nucleic acid biosensor", Biosens. Bioelectron., vol. 23, 2008, pp. 879

[8] Luke Johnson, Amit K. Gupta, Azam Ghafoor, Demir Akin, Rashid Bashir, "characterization of vaccinia virus particles using microscale silicon cantilever resonators and atomic force microscopy", Sensors and Actuators B, 2005, pp. 9.

[9] R.L. Rich, D.G. Myszka, "Spying on HIV with SPR", Trends Microbiol., vol. 11, 2003, pp. 124

[10] R. Yan, N.S. Lynn, L.C. Kingry, Z. Yi, R.A. Slayden, D.S. Dandy and K.L. Lear, "Waveguide biosensor with integrated detector array for tuberculosis testing," Applied Physics Letters, vol. 98, 2010, pp. 013702

[11] Peng Wu, Paul Hogrebe, David W. Grainger, "DNA and protein microarray printing on silicon nitride waveguide surfaces", Biosensors and Bioelectronics, vol. 21, 2006, pp. 1252–1263

[12] Warren J. Wiscombe, "Mie scattering calculations: advances in technique and fast, vector-speed computer codes", National Technical Information Service, U.S. Dept. of Commerce, 1979

[12] H. Chew, D.S. Wang, M. Kerker, "Elastic scattering of evanescent electromagnetic waves", Appl. Opt. vol. 18, 1979, pp. 2679

[13] C. Liu, T. Kaiser, S. Lange, G. Schweiger, "Structural resonances in a dielectric sphere illuminated by an evanescent wave", Opt. Commun. vol. 117, 1995, pp. 521

[14] Patrick C. Chaumet, Adel Rahmani, Fre ́de ŕique de Fornel, and Jean-Paul Dufour, “Evanescent light scattering: The validity of the dipole approximation”, Physical Review B, vol. 58, 1998, pp. 2310

[15] M. Quinten, A. Pack, R.Wannemacher, “Scattering and extinction of evanescent waves by small particles”, Appl. Phys. B, vol. 68, 1999, pp. 87–92

[16] R. Yan, G. Yuan, M.D. Stephens, X. He, C.S. Henry, D.S. Dandy, and K.L. Lear, “Evanescent field response to immunoassay layer thickness on planar waveguides,” Applied Physics Letters, vol. 93, pp. 101110-3, 2008.

Chapter 9

ACHIEVEMENTS AND CONCLUSIONS

9.1 Achievements and Conclusions

The overall objective of this Ph.D research work is to develop a chip-scale inexpensive, compact, rugged, and simple biosensing system. To achieve this goal, both theoretical and experimental studies were used to study different devices and systems from simple format waveguides and Y-splitters to complicated devices including LEAC waveguide biosensors with and without integrated buried detector arrays. BPM and FDTD methods have been applied to achieve a better understanding of the working mechanism of the LEAC biosensor. Different characterization methods, including NSOM, a DC measurement system and a LabVIEW controlled AC measurement system were used in different stages in this project. A summary of the achieved milestones is listed below.

9.1.1 Theoretical study of LEAC sensors

LEAC sensors have been modeled using both a customized 1-D mode solver written in MATLAB [1] and a commercial simulation software from Rsoft [2][3]. Some of the most important parameters were studied and optimized. For example, the relationship between the geometric dimensions of the waveguide in the LEAC sensor and the refractive index of the waveguide core has been studied to ensure a single mode waveguide in the LEAC sensor. The

sensitivity of the LEAC biosensor has also been studied using simulations and verified with experimental data [2].

9.1.2 NSOM characterization on basic waveguide structures and LEAC biosensors without buried detector arrays

A LEAC sensor structure without buried detector arrays has been characterized with NSOM to study its response to different adlayers [1]. The asymmetric waveguide sensor is adopted since it allows more light power to "leak" into the evanescent mode in the lower cladding, which increases the sensitivity of the sensor. After comparison with other candidate materials, the material of SiNx was chosen as the waveguide core and SiO_2 was chosen as the lower cladding for their mechanical strength, optical properties and compatibility with CMOS technology, which lowers both the cost and difficulties in fabrication. A sequence of steps that exploits traditional sputtering, photolithography and dry etch technologies has been developed for waveguide fabrication. The procedure includes a multiple step facet polishing process and end-fire light coupling. In light coupling for NSOM characterization, we used a method of permanently bonding an optical fiber to the waveguide chip to ensure the mechanical stability during the movement and measurement of the sample. As discussed in Chap. 5, optical splitters will grant the chip multi-detection ability with a minimal number of light sources for the LEAC biosensor. A group of Y-type splitters, which have the same structure as the waveguide in the LEAC sensor, were fabricated using a similar process.

In the initial proof-of-concept sensor experiments single and multiple immunoassay complex adlayers, including CRP antibody/antigen binding with different concentrations[1], were patterned on the sensor sample using microfluidic channels. NSOM was used to characterize the sensors. In the CRP experiment, modulation of 50% has been measured with 1mg/ml CRP antigen concentration. Sensitivity of 3.3%/nm was determined by increasing the CRP concentration from 0μg/ml to 0.6 mg/ml.

In the Y-type splitter study, the relationship between the branching ratio and the phase difference as well as temperature change was studied [4]. After the proof-of-concept experiment, investigating a LEAC biosensor with integrated buried detector arrays was the next step.

9.1.3 Measurement on a LEAC sensor using integrated buried detectors

After the proof-of-concept experiment, a LEAC sensor with buried detector arrays was also fabricated and characterized. The chip was designed by Guangwei Yuan[5] and fabricated byAvago Technologies Inc. using traditional CMOS fabrication flow. These samples will be referred as Avago chips in the following descriptions.

To test the buried detector array on the Avago chip, a thin layer of photoresist (~120nm) was patterned across the waveguide and the photocurrents from the integrated buried detector array were collected by a DC measurement system employing a Keithley K4200 multimeter. Approximately an 89% modulation ratio was measured after the patterning of the thinned photoresist [1]. To further characterize the response of the Avago chip to real bio-molecules,

BSA was patternedonto the chip. Two methods, micro-tube (fiber jacket) and PDMS reservoir patterning, were developed to attain a well-controlled, uniform BSA patterning on the sample. A modulation ratio of ~15% was observed in response to a ~1nm thick BSA film, which agrees well with the BPM simulation results [3].

To further decrease the noise level during the measurement, an AC measurement system was built to replace the DC measurement system. A lock-in amplifier was used to filter out all frequencies except for the known modulated source frequency. A USB A/D card with a homebrew LabVIEW program was used to collect and analyze the data. A reference probe was added into the system to calculate out any guided light power changes in the waveguide due to light coupling fluctuations.

To investigate the immunoassay ability of the Avago chip, goat-anti-mouse IgG antibody and antigen were printed on the sample using a VersArray ChipWriter Pro system. Approximately a 16% modulation ratio was observed from the goat-anti-mouse IgG (antibody) patterning. An additional ~4% decrease in photocurrent was detected after the mouse IgG (antigen) incubation[6]. HspX, a TB reactive antibody, was immobilized on the sample to investigate the application of the LEAC biosensor in TB diagnostics. Antigen 85 was used as a negative control molecule to test selectivity of the LEAC sensor. Binding of antibodies to the HspX protein probe region resulted in an 8% maximum modulation while no significant change in the photocurrent with the antigen-85 was observed, which indicated that the LEAC biosensor could be used to selectively detect specified TB antibodies [7].

To test the virus detection ability of LEAC sensor, 40nm and 200nm polystyrene nanoparticles were immobilized onto the waveguide, and the increased scattered light was collected. Sensitivities of 1%/particle and 0.04%/particle were observed for 200nm and 40nm particles respectively.

9.1.4 Design of the 3rd generation LEAC sensor compatible with microfluidic channel integration

During the characterization of the Avago chips a lot of problems were revealed; the waveguide width and detector length design, the non-optimized position of detector pads for real-time monitoring, and the photocurrent generated by the scattering light from the polishing edge. To solve these probelms a new LEAC sensor chip was designed to allow real-time monitoring and compatibility with microfluidic channel integration. LASI CAD software was used to design the new mask. A waveguide bend was used to minimize the effect of the scattering light from the polishing edge during the fiber light coupling. Metal pads were placed far from the waveguides for three reasons: 1) Enable detection while the waveguide was covered by microfluidic channels, 2) Reduce the possibility of scratching the waveguide using micro probes, and 3) Avoid the possible PDMS channel leaking problem due to the bad adhesion between PDMS and Al. Several batches of new LEAC samples have been fabricated in the CSU cleanroom. Limited by the cost and equipment, chemical mechanical polishing (CMP) won't be included in the new LEAC sensor fabrication flow, so the mesa detector structure has been

replaced with the thin insulator detector structure. Multichannel measurement system consisting of a multiplexing/amplification circuit, a probe card and a LabVIEW data acquisition/control program has been implemented, although the circuit still needs some improvement to further decrease the noise. PDMS microfluidic channel has been tested with the LEAC sensor, and a SU-8/glass microfluidic channel system will be used to replace the PDMS channel to address some problems encountered, such the leaking problem on some surfaces and PDMS residue problem.

9.2 Conclusion and suggestions

We have designed and tested 3 generation of LEAC biosensors with different analytes. The 3rd generation of LEAC sensor has been fabricated in the CSU cleanroom and characterized. The optical waveguide part of the chip works well after some optimizations, while the MSM detector part of the chip still has some performance problems, such as the large dark current, the inconsistence photocurrent on different detectors, unstable signals from each detector. Many possible reasons, such as the material properties, the non-uniform device layer thicknesses on the SOI wafers, poor metal-Si contacts, could lead to these problems. Some of the future work could include the tests the chips fabricated from SOI wafers with different resistivities, thicknesses and uniformities. Different metal-silicon contact tests may also help to further improve the performance of the MSM detector array. The waveguide-detector distance will be needed to adjusted after the upper cladding is changed from air to water for the microfluidic channel tests.

For the characterization, Small particle test could be the used to test the sensor sample before the channel integration. Sucrose test could be the first experiment to be done after the microfluidic channel integration, and this will provide the sensitivity and LOD of LEAC sensor for the bulk RI change.

Deposition of the thin layer of palladium onto the LEAC sample could form a hydrogen sensor with local detection ability or a reference channel built on the same waveguide. Metal loaded waveguide could be alternative waveguide option for hydrogen sensor. A SPR sensor could be built by depositing a layer of Ag or Au.

Complete publications and awards

[Publications]

Journal papers

[1] R. Yan, Z. Yi, R. Safaisini, K. Lear, "Structure Optimization for Local Evanescent Field Shift Biosensing," manuscript in preparation for IET Optoelectronics.

[2] R. Yan, N.S. Lynn, L.C. Kingry, R.A. Slayden, D.S. Dandy and K.L. Lear, "Virus detection using a local evanescent array coupled biosensor," manuscript in preparation for Nature Photonics.

[3] N.S. Lynn, R. Yan, L.C. Kingry, R.A. Slayden, D.S. Dandy and K.L. Lear, "?", manuscript in preparation for Analytical Chemistry.

[4] R. Yan, N.S. Lynn, L.C. Kingry, Z. Yi, R.A. Slayden, D.S. Dandy and K.L. Lear, "Waveguide biosensor with integrated detector array for tuberculosis testing," Applied Physics Letters, vol. 98, pp. 013702, 2010.

[5] R. Yan, S.P. Mestas, G. Yuan, R. Safaisini, D.S. Dandy, and K.L. Lear, "Label-free silicon photonic biosensor system with integrated detector array," Lab on a Chip, Featured on the front cover, vol. 9, pp. 2163-2168, 2009.

[6] R. Yan, S.P. Mestas, G. Yuan, R. Safaisini, and K.L. Lear, "Response of Local Evanescent Array-Coupled Biosensors to Organic Nanofilms," IEEE Journal of Selected Topics in Quantum Electronics, vol. 15, pp. 1469-1477, 2009.

[7] R. Yan, G. Yuan, M.D. Stephens, X. He, C.S. Henry, D.S. Dandy, and K.L. Lear, "Evanescent field response to immunoassay layer thickness on planar waveguides," Applied Physics Letters, vol. 93, pp. 101110-3, 2008.

Conference Papers:

[1] David S. Dandy, N. Scott Lynn, Luke C. Kingry, Rongjin Yan, and Kevin L. Lear, "Label Free Detection of Virus-Like Particles", MicroTAS, 2011

[2] Z. Yi, R. Yan, R. Safaisini, K. Lear, "Optimization of waveguide thickness for local evanescent field shift detection," SPIE Photonic West 2011, 7888-21, 2011

[3] K. Lear, R. Yan, D. Dandy, N. Lynn, R. Slayden, L. Kingry, "A novel evanescent field biosensor with an integrated photodetector array (invited)," SPIE Photonic West 2011, 7888-5, 2011

[4] R. Yan, S. Lynn, L. Kingry, R. Slayden, D. Dandy and K. Lear, "Demonstration of nanoparticle detection using a local evanescent array coupled biosensor," The 23rd Annual Meeting of the IEEE Photonics Society, TuN2, 2010

[5] R. Yan, S. Lynn, L. Kingry, D. Dandy, R. Slayden, and K. Lear , "Waveguide biosensor with integrated photodetector array for tuberculosis serology ," The Conference on Lasers and Electro-Optics (CLEO) 2010, AMC5, 2010.

[6] R. Yan, S. Lynn, L. Kingry, R. Slayden, D. Dandy, and K. Lear, "An optical waveguide array biosensor for serology," Biomedical Sciences Instrumentation, vol. 46, pp. 45-50, 2010.

[7] R. Yan, L. Kingry, R. Slayden, and K. Lear , “Demonstration of the immunoassay using local evanescent array coupled biosensor ,” SPIE Photonic West 2010, pp. 7559-14, 2010.

[8] K. Lear and R. Yan, “A photonic biosensor system on a CMOS chip (Invited),” SPIE Photonic West 2010, pp. 7606-11, 2010.

[9] R. Yan, S. Mestas, Guangwei Yuan, and K. Lear, “High sensitivity local evanescent array coupled biosensors with nanometer BSA film,” The Conference on Lasers and Electro-Optics (CLEO) 2009, CTuCC5, 2009.

[10] R. Yan, G. Yuan , S. Mestas, R. Safaisini, and K. Lear, “Demonstration of local evanescent array coupled biosensors with organic nanofilms,” The 21th Annual Meeting of the IEEE Lasers and Electro-Optics Society (LEOS), pp. 240-241, 2008

[11] R. Yan, G. Yuan, R. Pownall, and K. Lear, “A novel low-loss y-type splitter with adjustable branching ratio,” The 20th Annual Meeting of the IEEE Lasers and Electro-Optics Society (LEOS), pp. 543-544, 2007.

[12] R. Yan, G. Yuan, R. Pownall, and K.L. Lear, “Waveguide Characterization Using Shear Force Scanning Optical Microscopy,” 2007 American Physical Society Annual Meeting, L38.00015, 2007.

[13] G. Yuan, R. Yan, M. Stephens, D. Dandy, and K. Lear, “Evanescent field response to small patterned features on a planar waveguide biosensor,” 2007 American Physical Society Annual Meeting, J41.00006, 2007.

[14] K. Lear, G. Yuan, M. Stephens, X. He, R. Pownall, R. Yan, P. Nikkel, C. Henry, T. Chen, and D. Dandy, "A waveguide biosensors local evanescent field response to an immunoassay complex," 2007 Digest of the IEEE/LEOS Summer Topical Meetings, pp. 97-98, 2007.

[Recent Awards]

2010 Chinese Government Award for Outstanding Self-financed Students Studying Abroad, Ministry of Education of the People's Republic of China

2010 SPIE Scholarship in Optical Science and Engineering

2010 The best reviewed paper in Rocky Mountain Bioengineering Symposium

2009 Winner of the Colorado Photonics Industry Association (CPIA) poster contest

References:

[1] R. Yan, G. Yuan, M.D. Stephens, X. He, C.S. Henry, D.S. Dandy, and K.L. Lear, "Evanescent field response to immunoassay layer thickness on planar waveguides," *Applied Physics Letters,* vol. 93, 2008, pp. 101110-3.

[2] R. Yan, S.P. Mestas, G. Yuan, R. Safaisini, D.S. Dandy, and K.L. Lear, "Label-free silicon photonic biosensor system with integrated detector array," *Lab on a Chip,* vol. 9, 2009, pp. 2163-2168.

[3] R. Yan, S.P. Mestas, G. Yuan, R. Safaisini, and K.L. Lear, "Response of Local Evanescent Array-Coupled Biosensors to Organic Nanofilms," *Journal of Selected Topics in Quantum Electronics,* vol. 15, 2009, pp. 1469-1477.

[4] R. Yan, G. Yuan, R. Pownall, and K. Lear, "A novel low-loss y-type splitter with adjustable branching ratio," 2007, pp. 543-544.

[5] Y. Guangwei, "Characterization of integrated optical waveguide devices," *Dissertation.*

[6] R. Yan, L. Kingry, R. Slayden, and K. Lear, "Demonstration of the immunoassay using local evanescent array coupled biosensor," *SPIE Photonic West 2010*, 2010, pp. 7559-14.

[7] R. Yan, S. Lynn, L. Kingry, D. Dandy, R. Slayden, and K. Lear, "Waveguide biosensor with integrated photodetector array for tuberculosis serology," *submitted to The Conference on Lasers and Electro-Optics (CLEO) 2009*, 2010.

[8] R. Yan, S. Lynn, L. Kingry, R. Slayden, D. Dandy, and K. Lear, "An optical waveguide array biosensor for serology," *Rocky Mountain Bioengineering Symposium*, 2010.

[9] P. Wu, P. Hogrebe, and D.W. Grainger, "DNA and protein microarray printing on silicon nitride waveguide surfaces," *Biosensors and Bioelectronics,* vol. 21, Jan. 2006, pp. 1252-1263.

Appendix A: LEAC sensor fabrication flow

I. Buried detector fabrication

a. Preparation:

1.) Take AZ2070 photoresist out of the refrigerator in the hood 2 hours in advance of fabrication. Make sure the condensation on the outside of photoresist bottle has completely gone before opening the bottle.
2.) Use the glass knife to cut out 1.5mm×1.5mm to 2mm×2mm square pieces out of the SOI wafer. Cut from the back side of the wafer.
3.) Clean the samples with acetone, methanol, and water. Place the samples face up on a piece of paper under the hood, and blow dry the top of the sample with an air gun. Make sure the air blows vertically to the sample, and turn off the air gun before remove the air gun away to avoid the air blows the samples away.

b. SiO_2 deposition:

1.) Put in a Si wafer piece to be the control piece for the SiO_2 deposition.
2.) Follow the PECVD procedure to deposit a **250nm** thick SiO_2 layer. With the standard SiO_2 setting documented in the cleanroom, SiO_2 deposition rate is **170Å/min**. So the deposition time is 11'46" – 14'42".
3.) Measure the SiO_2 thickness on both the sample and the control piece with the Filmetrics.

c. Photolithography:

1.) Clean the sample with acetone, methanol, and water. Then blow dry it.
2.) Prebake: bake with **120 ℃** for **2 min**, and cool it down to room temperature.
3.) Place the sample on the spinner, apply HDMS. Spin at **3000rpm** for **30 sec**.
4.) Apply AZ2070 photoresist, spin at **4000rpm** for **50 sec**.
5.) Softbake: bake with **100 ℃** for **2 min**, and cool it down to room temperature.
6.) Edge bead removal (*Critical step*): use a razor blade to remove as much photoresist on the edges as you can. Be careful not to break the samples too.
7.) If the procedure isn't followed by alignment and exposure right away, soak the samples in water till right before the alignment.
8.) Alignment: Clean the **mask** with acetone and methanol. Follow the alignment procedures.
9.) Exposure: (right aligner) **14mj** for **30 sec**.
10.) Develop: AZ300MIF for **~30 sec**. Examine under the microscope to see if results are desired; if not, further develop for **5 sec**. Repeat the 5-sec development procedure until all excess photoresist is gone.

11.) Postbake: bake with **110 ℃** for **1.5 min**, and cool it down to room temperature.

d. Etching: follow the MicroRIE procedure
   1.) Put four glass slides around the samples with the rough side facing down.
   2.) O_2 plasma cleaning: O_2 40 sccm, 40W, 1 min
   3.) Etching: CF_4 + O_2 8% 40 sccm, 40W, etching rate: **1.25 nm/sec**. Use the Filmetrics measured SiO_2 thickness to calculate the etching time, e.g. for 250nm is 2'20".
   4.) Clean the sample with acetone, methanol, and water. Then blow dry it.

II. Metal deposition

a. Preparation:
   1.) Take AZ2070 photoresist out of the refrigerator in the hood 2 hours in advance of fabrication.

b. Lift-off photolithography:
   1.) Clean the sample with acetone, methanol, and water. Then blow dry it.
   2.) Prebake: bake with **120 ℃** for **2 min**, and cool it down to room temperature.
   3.) Place the sample on the spinner, apply HDMS. Spin at **3000rpm** for **30 sec**.
   4.) Apply AZ2070 photoresist, spin at **4000rpm** for **50 sec**.
   5.) Softbake: bake with **100 ℃** for **2 min**, and cool it down to room temperature.
   6.) Edge bead removal (*Critical step*): use a razor blade to remove as much photoresist on the edges as you can. Be careful not to break the samples too.
   7.) If the procedure isn't followed by alignment and exposure right away, soak the samples in water till right before the alignment.
   8.) Alignment: Clean the **mask** with acetone and methanol. Follow the alignment procedures.
   9.) Exposure: (left aligner) **10mj** for **1 min**.
   10.) Develop: AZ300MIF for **~30 sec**. Examine under the microscope to see if results are desired; if not, further develop for **5 sec**. Repeat the 5-sec development procedure until all excess photoresist is gone.
   11.) Postbake: bake with **110 ℃** for **1.5 min**, and cool it down to room temperature.

c. Metal deposition:
   1.) Follow the E-beam metal deposition procedures. Deposit **300nm** thick.

d. Lift-off:
   1.) Optional: soak the sample in acetone overnight. Cover the acetone container with lid and place a heavy stuff on top of the lid for the minimum evaporation.

2.) Air brush the sample with acetone to wash away the photoresist. Don't ever let the sample dry out before all the excess photoresist is completely removed. Otherwise, the photoresist will never come off again.
3.) After all the photoresist is washed off, spray with methanol and water. Then blow dry it.

III. Insulator and waveguide deposition

a. SiO_2 deposition
   1.) Put in a Si wafer piece to be the control piece for the SiO_2 deposition.
   2.) Follow the PECVD procedure to deposit a **1.5μm** thick SiO_2 layer. With the standard SiO_2 setting documented in the cleanroom, SiO_2 deposition rate is **170Å/min**. So the deposition time is 88'14".
   3.) Measure the SiO_2 thickness on both the sample and the control piece with the Filmetrics.

b. SiN_x deposition
   1.) Put in a Si wafer piece to be the control piece for the SiO_2 deposition.
   2.) Follow the PECVD procedure to deposit a **150nm** thick SiN_x layer. With the standard SiN_x setting documented in the cleanroom, SiN_x deposition rate is **160Å/min**. So the deposition time is 9'23".
   3.) Measure the SiN_x thickness on both the sample and the control piece with the Filmetrics.

IV. Waveguide fabrication

a. Photolithography:
   1.) Clean the sample with acetone, methanol, and water. Then blow dry it.
   2.) Prebake: bake with **120 ℃** for **2 min**, and cool it down to room temperature.
   3.) Place the sample on the spinner, apply HDMS. Spin at **3000rpm** for **30 sec**.
   4.) Apply S1818 photoresist, spin at **6000rpm** for **30 sec**.
   5.) Softbake: bake with **100 ℃** for **2 min**, and cool it down to room temperature.
   6.) Edge bead removal (*Critical step*): use a razor blade to remove as much photoresist on the edges as you can. Be careful not to break the samples too.
   7.) Alignment: Clean the mask with acetone and methanol. Follow the alignment procedures.
   8.) Exposure: (left aligner) **10mj** for **35 sec**.

9.) Develop: AZ400K for **~17 sec** until all excess red photoresist is gone. Examine under the microscope to see if results are desired; if not, further develop for **5 sec**. Repeat the 5-sec development procedure until all excess photoresist is gone.

10.) Postbake: bake with **120 ℃** for **1 min**, and cool it down to room temperature.

b. Etching: follow the MicroRIE procedure

1.) Put four glass slides around the samples with the rough side facing down.

2.) O_2 plasma cleaning: **O_2 40 sccm, 40W**, **30 sec**

3.) Etching: **CF_4 + O_2 8% 40 sccm, 40W,** etching rate: **1.25 nm/sec**. Use the Filmetrics measured SiN_x thickness to calculate the etching time, e.g. for 150nm is 2'.

4.) Clean the sample with acetone, methanol, and water. Then blow dry it.

V. Open via

a. Preparation:

1.) Take AZ2070 photoresist out of the refrigerator in the hood 2 hours in advance of fabrication.

b. Photolithography:

1.) Clean the sample with acetone, methanol, and water. Then blow dry it.

2.) Prebake: bake with **120 ℃** for **2 min**, and cool it down to room temperature.

3.) Place the sample on the spinner, apply HDMS. Spin at **3000rpm** for **30 sec**.

4.) Apply AZ2070 photoresist, spin at **4000rpm** for **50 sec**.

5.) Softbake: bake with **100 ℃** for **2 min**, and cool it down to room temperature.

6.) Edge bead removal (*Critical step*): use a razor blade to remove as much photoresist on the edges as you can. Be careful not to break the samples too.

7.) If the procedure isn't followed by alignment and exposure right away, soak the samples in water till right before the alignment.

8.) Alignment: Clean the **mask** with acetone and methanol. Follow the alignment procedures.

9.) Exposure: (right aligner) **14mj** for **30 sec**.

10.) Develop: AZ300MIF for **~30 sec**. Examine under the microscope to see if results are desired; if not, further develop for **5 sec**. Repeat the 5-sec development procedure until all excess photoresist is gone.

11.) Postbake: bake with **110 ℃** for **1.5 min**, and cool it down to room temperature.

c. Wet etching

1.) Use plastic/anti-acid tweezers to dip the sample into Silox Vapox III (Transene Co) for **~10 sec** followed by microscope examination, and Filmetircs, repeat this procedure until SiO_2 is gone.
2.) Clean the sample with acetone, methanol, and water. Then blow dry it.

Appendix B: Scattering loss correction factor calculation

The following calculation is aim to get a correction factor to cancel out the effect of the increased waveguide loss due to patterning of nanoparticles, which has been described in Ch. 8.

Before the patterning of the small particles, the power detected by detector i could be defined as,

$$P_{di} = P_1[1-(s+c)]^{i-1}(r_s s + r_c c) \tag{1}$$

P_1 is the guided light power in the waveguide at the position of detector 1, i is the detector number, s is the scattering ratio, c is the waveguide loss ratio due to the loss of evanescent field, r_s the detector absorption ratio for scattering light and r_c is the detector absorption ratio for evanescent field.

Considering the reflectivity for normal incidence at the detector/lower cladding interface is 0.2, if we assume $r_c \approx r_s \approx r$,

$$P_{di} = P_1[1-(s+c)]^{i-1} r(s+c) \tag{2}$$

Assuming the particle patterning induced coupling ratio change, $\Delta c \approx 0$, the power detected by detector i after the particle pattering could be defined as,

$$P_{d1}' = P_1 r(s+c+\Delta s_1) \tag{3}$$

$$P_{di}' = P_1 \prod_{n=1}^{i-1}[1-(s+c+\Delta s_n)] r(s+c+\Delta s_i) \tag{4}$$

where Δs is the particle induced scattering ratio change, so the corrector factor could defined as,

$$K_i = \frac{[1-(s+c)]^{i-1}}{\prod_{n=1}^{i-1}[1-(s+c+\Delta s_n)]} \tag{5}$$

α_w is the propagation loss along the waveguide before the particle pattering, then

$$e^{-\alpha_w} = 1-(s+c) \tag{6}$$

When i=1, from (2),

$$P_1 r = \frac{P_{d1}}{1-e^{-\alpha_w}} \tag{7}$$

Assuming the particle induced scattering loss is proportional to the number of patterned particles, from (2), (3) and (7), we get

$$\Delta s_i = \frac{N_i}{N_1}\Delta s_1 = \frac{N_i}{N_1}\frac{P_{d1}^{'} - P_{d1}}{p_1 r} = \frac{N_i}{N_1} M_1 (1 - e^{-\alpha_w}) \tag{8}$$

where N_i is the particle number on detector i, and M_1 is the modulation ratio on detector 1.

Equation (4) could be wrote as,

$$K_i = \frac{e^{-\alpha_w \cdot (i-1)}}{\prod_{n=1}^{i-1}(e^{-\alpha_w} - \Delta S_n)} \quad \text{where } \Delta S_n = \frac{N_n}{N_1} M_1 (1 - e^{-\alpha_w}) = N_n \sigma (1 - e^{-\alpha_w}) \tag{9}$$

σ is the sensitivity of the sensor, with a unit of %/particle. In Fig. 1, the measured photocurrent before and after the correction is plotted and the modulation ratio before and after the correction is shown in Fig. 2.

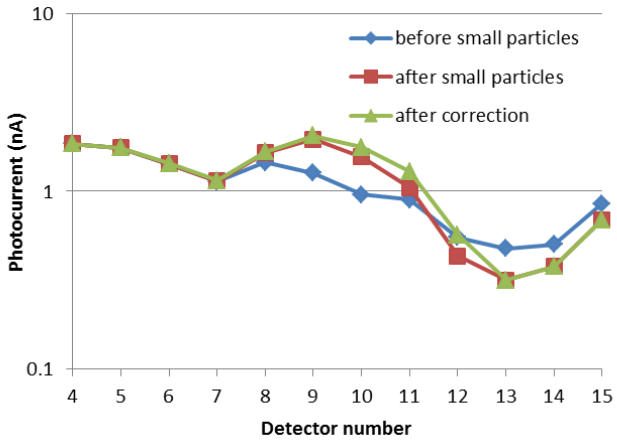

Fig. 1, Photocurrent measured before the particle patterning, after the particle patterning and after the correction

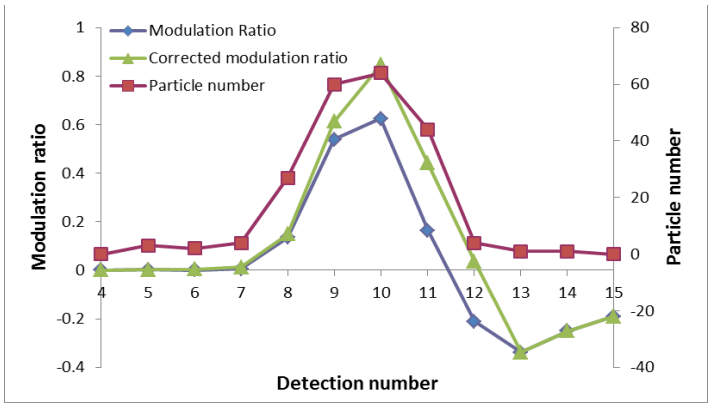

Fig. 2, Particle number distribution along the waveguide (red). Modulation ratio before the correction (blue). Modulation ratio after the correction (green).